technische universität
dortmund

Measuring Coherence Properties of Exciton-Polaritons with Homodyne Detection

Dissertation

zur Erlangung des akademischen Grades
Doktor der Naturwissenschaften
(Dr. rer. nat.)

vorgelegt
der Fakultät Physik
der Technischen Universität Dortmund

von

Carolin Lüders

Dortmund, 2022

Dissertation in der Fakultät Physik, Technische Universität Dortmund.

Einreichung: Dortmund, 26.08.2022

Disputation: Dortmund, 23.11.2022

Prüfungskommission:
Prof. Dr. Marc Aßmann (1. Gutachter, Technische Universität Dortmund)
Prof. Dr. Jan Sperling (2. Gutachter, Universität Paderborn)
Prof. Dr. Jan Kierfeld
Dr. Hans Dembinski

Contents

Abstract

For quantum technology, hybrid systems are needed to connect different physical systems, e.g. a matter system for information processing and light for communication. For connecting semiconductors and light, semiconductor quantum optics investigates how light influences the quantum state of the semiconductor and how the state of the semiconductor can be measured via the emitted light.
To measure the quantum state of light, optical homodyne tomography (OHT) is a versatile technique that is widely applied in quantum optics. But its application to semiconductor emission is often prevented by the lack of a fixed phase reference for nonresonant luminescence and by the fast time scales of the system.
These challenges are tackled in this work. We present the application of OHT to semiconductor luminescence without a fixed phase reference in order to investigate coherence properties and the quantum state. Thereby, a pulsed local oscillator and fast detectors enable a high time resolution. As a testbed for the method, we investigate the emission from an exciton-polariton condensate in a GaAs microcavity.
Specifically, this work shows which information can be gained by using one, two and three homodyne detection channels. With one channel, the second-order photon correlation function $g^{(2)}(0)$ is measured. Via two channels, we measure the phase-averaged Husimi function and quantify the amount of quantum coherence in the polariton system. With three channels, we reconstruct the regularized P function, depending on postselected initial conditions, and track the temporal decay of quantum coherence.

Zusammenfassung

Für die Quantentechnologie sind hybride Systeme gefragt, die verschiedene physikalische Systeme verbinden, z.B. ein Materiesystem zur Informationsverarbeitung und Licht zur Kommunikation. Für die Verbindung zwischen Halbleitern und Licht erforscht die Halbleiter-Quantenoptik, wie Licht den Quantenzustand des Halbleiters beeinflusst und wie der Zustand des Halbleiters über das emittierte Licht gemessen werden kann.
Zur Messung des Quantenzustands von Licht wird in der Quantenoptik die vielseitige Methode der optischen Homodyn-Tomographie (OHT) verwendet. Ihre Anwendung auf die Emission von Halbleitern wird jedoch häufig durch das Fehlen einer festen Phasenreferenz für nicht-resonante Lumineszenz und durch die schnellen Zeitskalen des Systems verhindert.
Diese Herausforderungen werden in dieser Arbeit angegangen. Wir stellen die Anwendung von OHT auf Halbleiterlumineszenz ohne feste Phasenreferenz vor, um die Kohärenz-Eigenschaften und den Quantenzustand zu untersuchen. Dabei ermöglichen ein gepulster Lokaloszillator und schnelle Detektoren eine hohe Zeitauflösung. Als Testumgebung für die Methode untersuchen wir die Emission eines Exziton-Polariton-Kondensats in einer GaAs-Mikrokavität.
Konkret zeigt diese Arbeit, welche Informationen durch die Verwendung von einem, zwei und drei Homodyn-Detektionskanälen gewonnen werden können. Mit einem Kanal wird die Photonenkorrelationsfunktion zweiter Ordnung $g^{(2)}(0)$ gemessen, mit zwei Kanälen messen wir die phasengemittelte Husimi-Funktion und quantifizieren den Grad der Quantenkohärenz im Polaritonensystem, und mit drei Kanälen rekonstruieren wir die regularisierte P-Funktion abhängig von postselektierten Anfangsbedingungen und verfolgen den zeitlichen Zerfall der Quantenkohärenz.

Chapter 1

Motivation

Semiconductors are a well-established technological platform and the centerpiece of our computers, smart phones and many other devices. Semiconductor components like transistors and diodes, as well as lasers, were developed during the last century as part of the so-called first quantum revolution, when scientists began to understand how quantum mechanics underlies the electronic properties of materials and the generation of light. However, the trend to miniaturize these components according to Moore's Law — the observation that the number of components in an integrated circuit doubles every one or two years [Mac11] — is reaching its limits while the demand for fast computing and high data transfer rates still increases.

Beside several possible ways to go past these limits [Wal16, Wil17], a second quantum revolution is in the making [DM03, Deu20]. Thereby, scientists and engineers aim at using the peculiarities of quantum mechanics like entanglement and superposition in order to develop new technologies, promising a speedup that exceeds any classical device.

To this aim, there is a need for quantum interfaces — also being called quantum interconnects or hybrid quantum systems — in order to connect different types of systems that carry the same quantum information [KBK$^+$15, ABB$^+$21]. For example, computations might be carried out by a matter-based system and the information then might be transferred via light, as illustrated in Fig. 1.1. Such interfaces are already well-engineered for classical devices, using semiconductor chips for computing and glass fibers for information transfer, whereas for quantum information processing, they are still under development. Furthermore, light-matter interfaces are also paramount for our fundamental understanding of how distinctively different physical systems can interact to realize seminal quantum phenomena.

These interfaces can comprise different kinds of matter systems, e.g. superconductors, atoms or solid-state color centers; however, since semiconductors are already well-established in industrial production, they might be more easily integrated into existing platforms and enable the fabrication of on-chip devices. Therefore, we focus here on

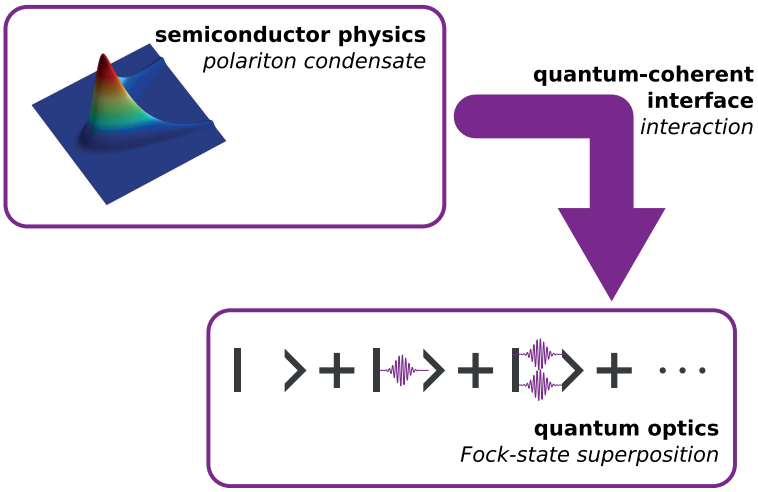

Figure 1.1: Visualization of a hybrid quantum system where quantum information is transferred between two different types of systems, e.g. a semiconductor for computation and light for communication [LPR+21].

the connection between semiconductors and light.

Unfortunately, in physics, the fields of semiconductors and quantum optics are mostly separated to date; one exception is the development of single-photon sources, where one optimizes the purity, the indistinguishability and the repetition rate of the produced photons [SGD+16], but this only concerns single-photon states and not general quantum states. To further connect these fields, one question for physicists is: how can we measure quantum properties of a semiconductor system via probing the emitted light? And also the other way around: can light influence the quantum state of a semiconductor?
These questions are only starting to be approached. Regarding the latter, it was shown that the photon statistics of the excitation light field can influence the output photon statistics and the intensity of an emitter [KSA+15, AB15, BHM+14]. Moreover, the photon statistics of the excitation light creates correlations between carriers in the material, e.g. bunched light may create biexcitons [CKR09] and a state of light with three-photon fluctuations may create correlations between three excitons [AHLC+14]. Along these lines, Ref. [KK06] proposed to "map the quantum-statistical properties of the exciting light directly onto the generated state of the quasiparticle excitations in matter." These ideas were extended by the pioneering works of Kira et al. [KKS+11], who characterized the response of the material to excitation light in arbitrary quantum states by a Wigner-function-like response distribution where a set of coherent states used for excitation spans the phase space.

But despite these insights on how light influences the state of a semiconductor, the converse problem — measuring the quantum state of a semiconductor by probing its

emitted light — was not comprehensively investigated. One routinely used tool is the photon statistics $g^{(2)}$ of the emission in order to verify single-photon generation; see e.g. Ref. [SGD$^+$16]. However, this is not a complete characterization of the quantum state since $g^{(2)}$ only depends on the diagonal of the density matrix and does not contain information on off-diagonal elements, i.e. superpositions of basis states.
A more advanced method in the toolkit of quantum optics, allowing a complete characterization of the quantum state of light, is quantum state tomography via homodyne detection (optical homodyne tomography, OHT) [LR09]. Nonetheless, this method was rarely applied to semiconductors yet. Usually, OHT requires a fixed relative phase between signal and detection. Without this phase reference, OHT only allows measuring photon statistics, as done e.g. for a superluminescent diode [MR97] and a diode laser [MBAR95, RC13]. If the sample is excited resonantly, the excitation laser can be used as a phase reference, which enabled the measurement of squeezed light from semiconductor polaritons via OHT [BBA$^+$14]. But this approach does not work for nonresonant excitation. Thus, a broader application of OHT to semiconductors is often prevented by the lack of a fixed phase reference. Another problem are the small time scales given by the coherence times of semiconductors that require a high time resolution of the detection system.

To bridge the aforementioned gaps, this work presents the application of OHT to a semiconductor system that is excited nonresonantly, demonstrating that in spite of the lack of a phase reference, information on the quantum state can be gained. The setup developed by Marc Aßmann, Johannes Thewes and myself achieves a high time resolution by using a pulsed laser with 0.5 - 1 ps pulse duration and a fast repetition rate of 75 MHz as a local oscillator (LO) for detection and fast balanced detectors with a bandwidth of 100 MHz. The lack of such fast detectors, which have only been engineered during the last decade [CQZ$^+$11, KBM$^+$12, HFW$^+$13], has mostly prevented the application of OHT at high repetition rates before. Furthermore, by using several homodyne detection channels, it is possible to reconstruct the relative phase between signal and LO and to calculate the conditional quantum state depending on selectable initial conditions and on the time delay between the channels [TLA20]. This method for time- and intensity-resolved quantum state tomography opens new possibilities to explore quantum dynamics and characteristics.
To describe the quantum state, I employ state-of-the-art theoretical concepts together with my collaborators at Paderborn University, including novel phase-space approaches and the concept of quantum coherence for quantifying superpositions both in matter and light, which are a sought-after resource for quantum information protocols [LM14, BCP14, SAP17]. Thereby, we use a particle-picture-based quantification of quantum coherence which is different than the wave-based nonclassicality criteria that

have been used before [Man86].

As a testbed for our methods, I investigate exciton-polaritons in a GaAs microcavity. Exciton-polaritons are quasi-particles arising when semiconductor excitons and photons are strongly coupled. GaAs is a well-established material and easy to connect with existing technology; however, exciton-polaritons can also exist in organic semiconductors for room-temperature usage [CGZ+17]. Exciton-polaritons are ideal candidates for hybrid systems: they inherently provide strong light-matter coupling, and the polariton-polariton interaction mediated via their excitonic part might be used for quantum information processing. Furthermore, polaritons might inherit the quantum properties of pump light and reproduce them in their emission [LSS+15]. Recent works demonstrated a transfer of entanglement from a single photon to polaritons [CLS+18] and possible indications of photon antibunching due to the polariton-polariton interaction [DFS+19, MMWJ+19]. Besides, polaritons may form a macroscopic condensate, which is accompanied by the spontaneous formation of coherence and off-diagonal long-range order in the system [KMSL07]. This condensation occurs at a carrier density that is several orders of magnitude smaller than for a laser and thus provides a more energy-efficient source for coherence [DHY10, DP12]. See also [KLS+22] for a review of the applicability of polariton condensates for classical and quantum computing. Previous studies on exciton-polaritons already characterized the first- and second-order correlation functions $g^{(1)}$ and $g^{(2)}$ and their decay times [LKW+08, TVA+12, KZW+16, KFA+18, APA+19, OTP+21] and the photon number distribution [KSF+18]. However, to the best of my knowledge, the amount of quantum coherence was not measured before our work in Ref. [LPR+21] and quantum state tomography was not performed.

This thesis is structured as follows: Chapter 2 and 3 introduce the theoretical background of quantum optics and exciton-polaritons, respectively. Chapter 4 presents the basic experimental setup that is common in all conducted measurements, consisting of homodyne detection and polariton spectroscopy. I perform a preliminary characterization of the sample in Chapter 5.
The next three chapters contain the main results of this thesis. Specifically, Chapter 6 presents time- and frequency-resolved measurements of the second-order photon correlation function $g^{(2)}(0)$ of the polariton emission, surpassing previous methods that rely on photon counting and need longer acquisition times such as the Hanbury Brown–Twiss setup [HT56], streak cameras [AVT+10], two-photon absorption [BGRF09] or transition edge sensors [KSF+18]. With our faster method, the intrinsic fluctuations of the light field are distinguished from extrinsic noise.
While the measurements in Chapter 6 only need one-channel homodyne detection, I use two channels in Chapter 7 in order to measure the Husimi function of the polariton

emission. This phase-space function is a more complete way to describe the state of light than $g^{(2)}$ and allows me to quantify the amount of quantum coherence in the polariton system.

In Chapter 8, I extend the measurements to three homodyne channels and implement a phase-sensitive reconstruction of an advanced phase-space function, the regularized P function P_Ω, depending on postselected initial conditions. By scanning a time delay between the three channels, I track the temporal decay of quantum coherence, which is vital for applications.

Finally, a conclusion and an outlook can be found in Chapter 9.

I hope that this work serves as a starting point for future research on semiconductor quantum optics and hybrid quantum systems.

Chapter 2

Theoretical background — Quantum optics and coherence

This chapter introduces the most important concepts from quantum optics needed for our investigations on polariton condensates. In particular, we explain different notions of coherence and different ways to characterize a quantum state of light.

2.1 First-order correlation function and coherence time

Before diving into the quantum description of light, we review the classical notion of coherence. In classical physics, light is described as an ensemble of electromagnetic waves in different modes $E(t) = \sum_i E_{0,i} \cos(\omega_i t + \phi_i)$, each mode i with a given amplitude $E_{0,i}$, phase ϕ_i and frequency ω_i. These waves might also have different polarizations, which we ignore here for simplicity. Consequently, the ensemble possesses a distribution of frequencies $F(\omega)$ with linewidth $\Delta\omega$. With increasing time, waves with different frequencies run apart and the total phase of $E(t)$ diffuses. Besides, the individual phases ϕ may vary discontinuously due to perturbations [Fox06, p. 17]. Thus, for large times, the phase relation between the waves is randomized and the ability of the light field to interfere with itself is lost.
In this framework, coherence is defined as the ability of a light field to interfere with itself, e.g. in a Michelson interferometer. This ability is quantified by the first-order correlation of the field [Fox06, p. 19]:

$$g^{(1)}(\tau,t) = \frac{\langle E^*(t)E(t+\tau)\rangle}{\langle |E(t)|^2\rangle}. \tag{2.1}$$

When $g^{(1)}(\tau) = 1$, the light field interferes with maximum contrast and is perfectly coherent, which is always the case for equal times $\tau = 0$. By contrast, for increasing time difference τ, $g^{(1)}(\tau)$ usually decreases, and for $g^{(1)}(\tau) = 0$, there is no coherence

and no ability to interfere. Accordingly, a coherence time can be defined from $g^{(1)}(\tau)$ as the time scale over which the coherence decays [MW62]:

$$\tau_c = \int_{-\infty}^{\infty} |g^{(1)}(\tau)|^2 d\tau. \tag{2.2}$$

The temporal correlation $g^{(1)}(\tau)$ is related to the power spectrum $F(\omega)$ by the Fourier transformation for a stationary random process, according to the Wiener-Khintchine theorem [MW95, p. 59]. The specific shape of both functions depends on the physics behind the light emission, the two most important cases being an exponential and a Gaussian shape of $g^{(1)}(\tau)$. The exponential case [AUM+07]

$$g^{(1)}(\tau) = \mathrm{e}^{-|\tau|/\tau_c} \tag{2.3}$$

corresponds to a Lorentzian spectrum and relates to homogeneous broadening. Its physical origin is natural broadening due to finite lifetimes or collision broadening that effects all emitters in the same way [Lou83].
The other well-known case is a Gaussian function [AUM+07]

$$g^{(1)}(\tau) = \mathrm{e}^{-\frac{\pi}{2}(\frac{\tau}{\tau_c})^2}, \tag{2.4}$$

corresponding to a Gaussian spectrum as well. This case results from inhomogeneous broadening. It occurs when different sources emit light with Gaussian-distributed frequencies, e.g. atoms in a gas with Doppler-shifted frequencies [MW95, p. 806] and an ensemble of quantum dots with a Gaussian size distribution [MGF+10].

In general, because of the Fourier relation, linewidth and coherence time are inversely proportional to each other. The smaller the linewidth, the longer lasts coherence. This hints at a problem of this classical notion of coherence: In principle, one could always filter a light field spectrally in order to achieve a longer coherence time, no matter if the light comes from a lightbulb or a laser. (Of course, for the laser, most of the intensity lies already in a small frequency range while, in the case of the light bulb, the intensity is spread over a wide frequency range and one would loose most of the intensity by filtering it.) Thus, in order to distinguish more precisely between different light states from different origins, a more advanced description is needed.

2.2 Light in the number-state representation

Quantum mechanically, each light wave is described as a harmonic oscillator with frequency ω. The amount of energy in this oscillator is quantized, meaning that energy can only be added and subtracted in "packages" of the amount $\hbar\omega$, called photons. Adding one photon is described by the creation operator $\hat{a}^\dagger$ and removing one photon

by the annihilation operator $\hat{a}$. Photons are bosons and obey the commutator relation $[\hat{a}_j,\hat{a}_{j'}^\dagger] = \delta_{j,j'}$, where j identifies different optical modes. How many of these elementary excitations are present is counted by the number operator $\hat{n} = \hat{a}^\dagger\hat{a}$, and their energy is then given by $\hbar\omega\hat{a}^\dagger\hat{a}$.
The entire light field consists of many modes with different frequencies ω_j and different properties, like spatial shape and polarization. Thus, the Hamilton operator of the total energy is given by [Sch01, p. 271]

$$\hat{H} = \sum_j \hbar\omega_j \left(\hat{a}_j^\dagger\hat{a}_j + \frac{1}{2}\right). \tag{2.5}$$

While $\sum_j \hbar\omega_j\hat{a}_j^\dagger\hat{a}_j$ is the energy of the total number of photons in the system, $\sum_j \hbar\omega_j\frac{1}{2}$ is the ground state or vacuum energy without any photons present.
For each mode, there exists a distinct family of states, the photon-number eigenstates $|n\rangle$, obeying $\hat{n}\,|n\rangle = n\,|n\rangle$ with $n \in \mathbb{N}$. Such states contain a specific number of photons n. But also superpositions of photon number states are possible, which do not possess a fixed photon number. In general, every possible state of the light field can be described as a superposition of various number states since these states form a complete basis, called the Fock basis. Thus, every state can be characterized by a density matrix in the Fock basis for each mode [MW95, p. 481]:

$$\rho = \sum_{n,m} \rho_{nm}\,|n\rangle\langle m|\,. \tag{2.6}$$

The diagonal elements of the density matrix ρ_{nn} correspond to the probability of measuring the photon number n, whereas the off-diagonal elements are a result of coherent quantum superpositions of the basis states.

2.3 Thermal and coherent light states

The two most important light states occuring in this work are the thermal state and the coherent light state, and a combination of both, the displaced thermal state. Therefore, we will discuss their properties and how they can be distinguished by more suitable criteria than $g^{(1)}(\tau)$.
A **coherent state** is the quantum mechanical equivalent to a classical wave with fixed amplitude and phase. This state is a good approximation of the light emitted by a laser.[1] It is defined as the right-hand-side eigenstate of the annihilation operator [Gla63]:

$$\hat{a}\,|\alpha\rangle = \alpha\,|\alpha\rangle\,, \tag{2.7}$$

[1] There was a debate on whether these states are really created by lasers, see Ref. [BRS06] for a summary.

with a complex eigenvalue $\alpha \in \mathbb{C} = |\alpha| e^{i\phi}$, with amplitude $|\alpha|$ and phase ϕ [Fox06, p. 134]. Astonishingly, photons can be removed from the coherent state without altering it. The coherent state can be expressed in the Fock basis [Gla63]:

$$|\alpha\rangle = e^{-\frac{1}{2}|\alpha|^2} \sum_n \frac{\alpha^n}{\sqrt{n!}} |n\rangle . \tag{2.8}$$

The density matrix is then given by

$$\rho = |\alpha\rangle \langle\alpha| = e^{-|\alpha|^2} \sum_{n,m} \frac{\alpha^n \alpha^{*m}}{\sqrt{n!m!}} |n\rangle \langle m| . \tag{2.9}$$

Thus, the coherent state is a superposition of an infinite number of photon number states and therefore does not possess a fixed photon number. We only know the probability for measuring each photon number [Gla63]:

$$\text{Prob}(n) = |\langle n|\alpha\rangle|^2 = \frac{|\alpha|^{2n}}{n!} e^{-|\alpha|^2}. \tag{2.10}$$

This is a Poisson distribution, describing random, independent events [MW95, p. 23]. Thus, each individual photon emission event is statistically independent of all the other ones for any delay τ. From the Poisson distribution follows the mean photon number and the variance [Fox06, p. 159]:

$$\langle \hat{n} \rangle = |\alpha|^2 \quad \text{and} \quad \text{Var}(n) = \langle \hat{n} \rangle. \tag{2.11}$$

This variance, which comes from the quantization and is not found in the classical description of an electromagnetic wave for non-random light, is also called shot noise.

Now let us compare this to a **thermal state**. A thermal state is created when many different sources independently emit light [Gla63], each with different phase and amplitude. In sum, the light field's amplitude and phase fluctuate rapidly on the time scale of the coherence time τ_c. The density matrix only has diagonal elements [Gla63]:

$$\rho = \frac{1}{1+\bar{n}} \sum_n \left(\frac{\bar{n}}{1+\bar{n}} \right)^n |n\rangle \langle n| , \tag{2.12}$$

with the mean photon number $\bar{n}$. This gives a Bose-Einstein distribution for the photon number probabilities [Fox06, p. 85]:

$$\text{Prob}(n) = \frac{1}{1+\bar{n}} \left(\frac{\bar{n}}{1+\bar{n}} \right)^n . \tag{2.13}$$

From this follows the variance, which is much higher than the coherent one for the same mean photon number,

$$\text{Var}(n) = \bar{n} + \bar{n}^2. \tag{2.14}$$

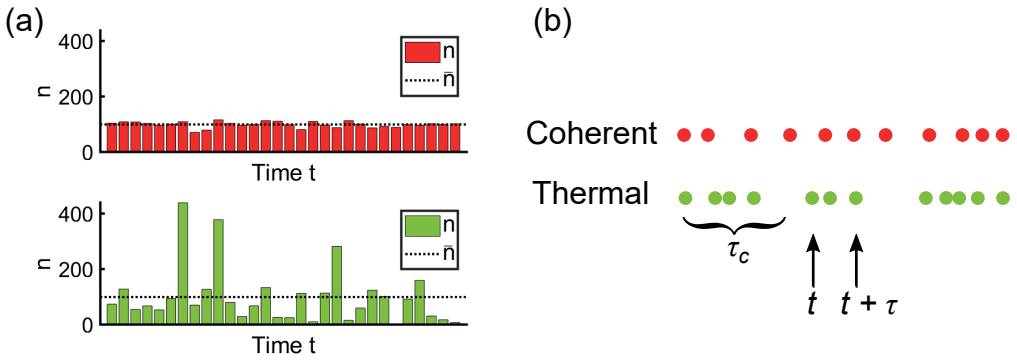

Figure 2.1: (a) Simulation of photon numbers detected in time intervals smaller than the coherence time, for an average photon number of 100. Top: Coherent state. Bottom: Thermal state. (b) Illustration of photon flux versus time for coherent and thermal state. After a first photon was detected at time t, a second photon is detected at time $t+\tau$ with enhanced probability for thermal light, as long as τ is smaller than the coherence time τ_c.

The different variances of coherent and thermal state can also be visualized by simulating repeated measurements of the photon number. Figure 2.1(a) shows results from such a simulation. For the coherent state, the measured number of photons fluctuates only slightly around the mean photon number whereas, for the thermal state, some instances show a very high photon number and some instances almost no photon at all. This behavior is called "bunching". It also means there is a correlation between photons: If one photon is measured, there is an increased probability to measure another one within the coherence time. This correlation can be quantified via the **second-order correlation function** and helps to distinguish thermal and coherent light.

2.4 Second-order correlation function

The second-order correlation function $g^{(2)}(\tau,t)$ is the probability to measure a photon at time $t+\tau$, after another photon was detected at time t, averaged over some time interval Δt [Fox06, p. 161]:

$$g^{(2)}(\tau,t) = \frac{\langle \hat{a}^\dagger(t)\hat{a}^\dagger(t+\tau)\hat{a}(t+\tau)\hat{a}(t)\rangle}{\langle \hat{a}^\dagger(t)\hat{a}(t)\rangle\langle \hat{a}^\dagger(t+\tau)\hat{a}(t+\tau)\rangle}. \tag{2.15}$$

The idea is visualized in Fig. 2.1(b).
For coherent light, photons are statistically independent of each other, thus $g^{(2)}(\tau) = 1$ for all τ [Lou83, p. 221]. By contrast, when detecting a photon from a thermal light field, there is an increased probability to detect another photon as long as τ is smaller than the coherence time τ_c. If photons from different spectral modes cannot be distinguished,

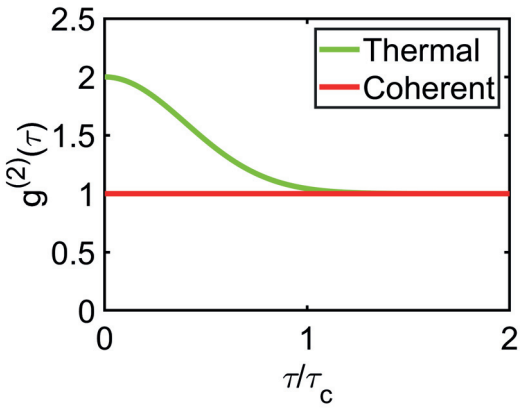

Figure 2.2: $g^{(2)}(\tau)$ vs τ for coherent light (red) and thermal light with Gaussian spectrum (green).

for thermal light the following relation holds between first- and second order correlation [Lou83, p. 221]:

$$g^{(2)}(\tau) = 1 + |g^{(1)}(\tau)|^2. \tag{2.16}$$

The dependence of $g^{(2)}(\tau)$ on τ is shown in Fig. 2.2 for coherent light and for thermal light with a Gaussian spectrum.

In the case of one mode of light and $\tau = 0$, $g^{(2)}(0)$ can also be related to the variance of the photon number. The numerator of Eq. (2.15) can be transformed with help of the bosonic commutator relation:

$$\langle \hat{a}^\dagger \hat{a}^\dagger \hat{a}\hat{a} \rangle = \langle \hat{a}^\dagger \hat{a}\hat{a}^\dagger \hat{a} - \hat{a}^\dagger \hat{a} \rangle = \langle \hat{n}^2 - \hat{n} \rangle = \langle \hat{n}^2 \rangle - \bar{n}. \tag{2.17}$$

Using the known relation $\langle \hat{n}^2 \rangle = \bar{n}^2 + \mathrm{Var}(n)$ [MW95], we find:

$$g^{(2)}(\tau = 0) = 1 - \frac{1}{\bar{n}} + \frac{\mathrm{Var}(n)}{\bar{n}^2}. \tag{2.18}$$

Thus, when the variance is high, the photon correlation increases as well. Using the variances for the coherent and thermal state Eq. (2.11) und (2.14), we find $g^{(2)}(\tau = 0) = 1$ for the coherent state and $g^{(2)}(\tau = 0) = 2$ for the thermal state.
If coherent and thermal light are combined, values between 1 and 2 are taken. Here, two different cases are imaginable. On the one hand, the light might come from two different, distinguishable modes. In that case, $g^{(2)}(\tau,t)$ is given by a statistical mixture of the different possibilities $g_{ij}^{(2)}(\tau,t)$ to detect photons from these modes [LHA+13]. On the other hand, thermal and coherent emission might happen in the same mode, which is the case for the displaced thermal states we investigate in Chapter 7. In that case, the photon number variance is given by [Lac65, KSF+18]:

$$\mathrm{Var}(n) = 2|\alpha_0|^2\bar{n}_{th} + |\alpha_0|^2 + \bar{n}_{th} + \bar{n}_{th}^2, \tag{2.19}$$

with the mean thermal photon number $\bar{n}_{th}$ and the mean coherent photon number $|\alpha_0|^2$. Inserting this into Eq. (2.18) gives

$$g^{(2)}(\tau = 0) = 2 - x^2, \tag{2.20}$$

where $x = |\alpha_0|^2/(|\alpha_0|^2 + \bar{n}_{th})$.
But also $g^{(2)}(\tau = 0) < 1$ is possible for single-photon sources, making $g^{(2)}(\tau = 0)$ an important criterion for quantum information applications; see e.g. [SGD+16]. Altogether, $g^{(2)}$ may be used as a criterion to distinguish different states of the light field, as long as the time resolution $\Delta\tau$ of the apparatus is smaller than the coherence time of the light. Besides, $g^{(2)}$ is not uniquely connected to only one kind of quantum state, thus prior knowledge is necessary. See Chapter 6 for a detailed discussion on time resolution and frequency-resolved $g^{(2)}(\tau = 0)$ measurements of polariton emission.

2.5 Quantum coherence

Up to now, we introduced the classical notion of coherence, $g^{(1)}$, which is a measure of phase stability and spectral width, and the second-order photon correlation $g^{(2)}$, which is related to the variance of the photon number. However, $g^{(1)}$ can be changed by filtering the signal and also is only a classical property while $g^{(2)}$ only depends on the photon number distribution, i.e. the diagonal elements of the density matrix in the Fock basis. It makes no statement about the presence of off-diagonal elements, i.e. superpositions of Fock states. But these superpositions can be used for quantum information protocols and provide a *resource* for applications. (Resource theories have emerged over the last years to quantify the usefulness of a physical system for quantum communication and computing; see Ref. [CG19] for a review.)
Therefore, theorists introduced a measure for the amount of superpositions in a system, called **quantum coherence** in contrast to previous notions of coherence [LM14, BCP14, SAP17]. It can be defined as the sum of the modulus square of the off-diagonal elements [BCP14] [2]:

$$\mathcal{C}(\rho) = \sum_{m,n\in\mathbb{N}:m\neq n} |\rho_{m,n}|^2. \tag{2.21}$$

Since ρ is Hermitian (i.e. $\rho = \rho^\dagger$), this corresponds to the squared distance in the Hilbert-Schmidt norm, $\|\hat{A}\|_{\mathrm{HS}} = [\mathrm{tr}(\hat{A}^\dagger\hat{A})]^{1/2}$, between the state ρ and an incoherent state ρ_{inc} with the same diagonal elements [SW18, LPR+21]:

[2] Using the square of the off-diagonal elements, i.e. the l_2 norm, is only one possible choice. In general, one wants the quantum coherence to be monotone with respect to the parameters of the system, so these can be ordered into "more" or "less" coherent. The l_2 norm is monotone with respect to the parameters of the states we study here and therefore can be used [LPR+21].

$$\begin{aligned}\mathcal{C}(\rho) =& \|\rho - \rho_{\text{inc}}\|_{\text{HS}}^2 = \text{tr}\left([\rho - \rho_{\text{inc}}]^2\right) \\ =& \text{tr}\left(\rho^2\right) - 2 \underbrace{\text{tr}\left(\rho\hat{\rho}_{\text{inc}}\right)}_{\substack{=\sum_n \rho_{n,n}\langle n|\rho|n\rangle \\ =\text{tr}\left(\rho_{\text{inc}}^2\right)}} + \text{tr}\left(\rho_{\text{inc}}^2\right) \\ =& \text{tr}\left(\rho^2\right) - \text{tr}\left(\rho_{\text{inc}}^2\right).\end{aligned} \tag{2.22}$$

Quantum coherence can be converted into other quantum correlations [MYG+16] and into entanglement [KSP16, CH16, QSG+18], which is a key resource for quantum-communication applications [HHHH09]. This conversion can be performed for example with a CNOT gate acting on a state with quantum coherence and an incoherent state [QSG+18].[3]

However, it requires attention that the quantum coherence depends on the basis of ρ. For example, in the coherent-state representation, a coherent state can be simply described by $|\alpha\rangle = \int d^2\alpha' \delta(\alpha' - \alpha)|\alpha'\rangle$ — with δ denoting the Dirac delta distribution — including no superpositions and therefore zero quantum coherence (please note that this expansion is not unique because coherent states form a generating system and not a basis; but the above expansion uses the minimum number of elements). Nonetheless, in the Fock basis, a coherent state is expressed by Eq. (2.8) and (2.9), having off-diagonal elements and therefore high quantum coherence. On the other hand, a photon-number state $|n\rangle$ includes no superpositions in the Fock base and therefore zero quantum coherence; but in the coherent-state representation, $|n\rangle$ is a superposition of $n+1$ coherent states [VS14] and thus possesses quantum coherence.

Indeed, quantum coherence is only defined with respect to a chosen "classical" reference. If one picks particle states $|n\rangle$ as the classical reference, then superpositions of those like the coherent state $|\alpha\rangle$ exhibit quantum coherence, and vice versa.

The choice of the reference depends on the kind of system under investigation. Mostly, in the context of quantum optics, coherent states are seen as classical because they correspond to lightwaves known from classical optics. But for some quantum applications, also coherent states provide resources. For example, they are exploited as a resource e.g. for random number generators and continuous-variable quantum key distribution (CV-QKD) [SAL11, FXA+16, PAB+20]. Moreover, the particle-based quantum coherence can be converted to entanglement with help e.g. of a pair-production process, $|n\rangle_p \mapsto |n\rangle_s \otimes |n\rangle_i$, where the pump photons decay into signal and idler photons [LPR+21].

[3] A simple example for this conversion are two coupled qubits in the states $|+\rangle|0\rangle$, where $|+\rangle = \sqrt{1/2}(|0\rangle + |1\rangle)$ is in a superposition of two basis states and possesses quantum coherence. The CNOT gate, which flips the qubit in the state $|0\rangle$ if the other qubit is in the state $|1\rangle$, then creates the entangled state $\sqrt{1/2}(|00\rangle + |11\rangle)$ [CH16].

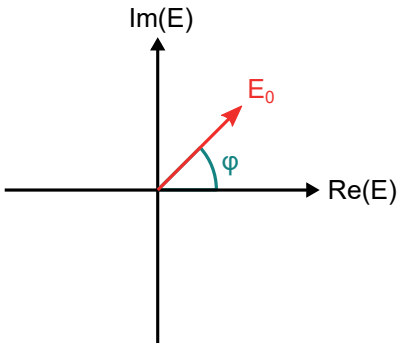

Figure 2.3: The phase-space diagram represents a classical electrical field with phase ϕ and amplitude E_0.

Especially for matter systems, Fock states as the particle basis are the classical default and their superpositions are seen as a quantum phenomenon. In this work, we aim at characterizing a matter system — a semiconductor cavity with polaritons — by probing the emitted light field. Therefore, we are looking for superpositions of particle states and use the Fock basis as the classical reference. We quantify the amount of quantum coherence of the polariton system in Chapter 7.

2.6 Continuous variables

Up to now, we described quantum properties of light in the Fock basis. However, actually measuring in this basis would require single-photon counting detectors with sufficient time resolution. In practice, there is also another useful approach, namely to measure **continuous variables** instead of discrete photon numbers. Nevertheless this approach allows to calculate quantities like $g^{(2)}$ and quantum coherence.
To introduce continuous variables, let us go back to the classical notion of the electrical field of light. The field can also be described as consisting of two oscillating fields, the field and its conjugate momentum, 90° out of phase with each other. These can be expressed as a complex amplitude with phase ϕ ([Fox06, p. 130]):

$$E = E_0 e^{i\phi} \tag{2.23}$$
$$= E_0 \cos\phi + iE_0 \sin\phi \tag{2.24}$$
$$= E_1 + iE_2. \tag{2.25}$$

The real part E_1 and the imaginary part E_2 are called **field quadratures**. They act as the axes of a coordinate system in which a vector represents the complex field amplitude E, as shown in Fig. 2.3.

Now coming back to quantum mechanics, the field quadratures correspond to the dimensionless operators $\hat{q}$ and $\hat{p}$, which are composed of the creation and annihilation operators [Sch01, p. 279-280]:

$$\begin{aligned} \hat{q} &= A(\hat{a}^\dagger + \hat{a}); \\ \hat{p} &= A\mathrm{i}(\hat{a}^\dagger - \hat{a}); \\ \hat{a}^\dagger &= \frac{1}{2A}(\hat{q} - \mathrm{i}\hat{p}); \\ \hat{a} &= \frac{1}{2A}(\hat{q} + \mathrm{i}\hat{p}). \end{aligned} \tag{2.26}$$

The positive normalization factor A assumes different values in the literature. The field quadratures are called continuous variables because they can take any value, in contrast to discrete variables like the photon number that are restricted to integers.
From the definition (2.26) and the bosonic commutator $[\hat{a},\hat{a}^\dagger] = 1$ follows a commutator for the field quadratures:

$$[\hat{q},\hat{p}] = 2A^2\mathrm{i}. \tag{2.27}$$

Using the definition (2.26) and the commutator, the mean photon number can be related to the expectation values of the quadratures:

$$\bar{n} = \langle \hat{a}^\dagger \hat{a} \rangle = \frac{1}{4A^2}(\langle \hat{q}^2 \rangle + \langle \hat{p}^2 \rangle) - \frac{1}{2}. \tag{2.28}$$

From the commutator also follows an uncertainty relation [AFP09], p. 87:

$$\Delta q \Delta p \geq \frac{1}{2} \left| \langle [\hat{q},\hat{p}] \rangle \right| = A^2. \tag{2.29}$$

Hence, the field quadratures $\hat{q}$ and $\hat{p}$ cannot be measured simultaneously with arbitrary precision but have an intrinsic uncertainty. When measuring them multiple times, one obtains a distribution of values with some width. The width is not necessarily equal in both directions but can be asymmetric, e.g. for so-called squeezed states. This distribution of quadrature values characterizes the light state equally well as the density matrix. It is called a **phase-space distribution** because $\hat{q}$ and $\hat{p}$ act similarly to the position and momentum coordinates of a harmonic oscillator, providing coordinates for the **phase space** of the system.
Since $\hat{q}$ and $\hat{p}$ represent the axes of a coordinate system, we must take into account that coordinate systems can be rotated. The absolute rotation, i.e. absolute phase, is not fixed but is a choice of the experiment, as follows. Let us consider a point in phase space given by the measured coordinates (q,p). Now we rotate the coordinate

system by an angle θ. Then, the point is described by the new coordinates (q_θ,p_θ) in the rotated coordinate system [AWH13, p. 134]:

$$q_\theta = q\cos\theta + p\sin\theta \tag{2.30}$$

$$p_\theta = -q\sin\theta + p\cos\theta. \tag{2.31}$$

By inserting definition (2.26), the rotated operator $\hat{q}_\theta$ is

$$\hat{q}_\theta = A(\hat{a}^\dagger e^{\mathrm{i}\theta} + \hat{a}e^{-\mathrm{i}\theta}). \tag{2.32}$$

This will be important in Section 4.1 where we discuss the homodyne detection method, where the rotation θ of the coordinate system is defined by the phase of the local oscillator.
Meanwhile, the next section introduces the most important phase-space distributions.

2.7 Phase-space distributions

Different kinds of phase-space distributions are available to describe a light state. This might be puzzling because, in classical mechanics, just one probability distribution $P_{cl}(q,p)$ is needed to calculate the expectation value of any quantity $O(q,p)$ [Sch01, p. 322] [4]:

$$\langle O(q,p)\rangle = \int\int O(q,p)P_{cl}(q,p)dqdp. \tag{2.33}$$

However, in quantum mechanics, the order in which non-commuting operators like $\hat{q}$ and $\hat{p}$ or $\hat{a}^\dagger$ and $\hat{a}$ are evaluated is relevant. Therefore, different kinds of phase-space distributions correspond to different operator ordering. For example, the Wigner, Husimi, and P distributions are associated with symmetric, antinormal (creation operators are always to the right of annihilation operators), and normal (creation operators to the left of annihilation operators) ordering, respectively [Sch01, p. 322].

Now we discuss the most important distributions, their advantages and drawbacks. In any case, phase-space distributions are an attempt to express the density matrix $\hat{\rho}$ in terms of the continuous variables q and p. These variables are related to annihilation and creation operators, according to Eq. (2.26), whose right-hand-side and left-hand-side eigenstates are the coherent states. Therefore, most phase-space distributions are defined by relating ρ to coherent states instead of Fock states. This is possible because coherent states form an overcomplete linear generating system — although they are not orthogonal to each other — so that each state can be represented as a linear combination

[4] Although in principle, one could convolute the classical distribution and apply this modified probability to compute expectation values. But this procedure does not provide any benefit, as opposed to quantum mechanics.

of them [Sud63].
One of these attempts is the **Glauber-Sudarshan P distribution**. It is defined by expressing the density matrix directly via coherent states [Gla63, Sud63]:

$$\hat{\rho} = \int d^2\alpha P(\alpha) \left|\alpha\right\rangle \left\langle\alpha\right| . \tag{2.34}$$

For a particular coherent state $|\alpha_0\rangle$, P is the delta distribution $P(\alpha) = \delta(\alpha - \alpha_0)$. This is already an example for the main drawback of the P distribution: for many quantum states, it is singular and no well-behaved function. Besides, the P distribution is ambiguous - a given quantum state can be represented by different P distributions [SV20]. To avoid these problems, the P distribution may be convoluted with a kernel K [SV20]:

$$P_K(\alpha) = \int d^2\alpha' K(\alpha,\alpha') P(\alpha'). \tag{2.35}$$

One of the possible results is the **Husimi-Kano Q function**, when using a Gaussian Kernel. It can also be defined as the expectation value of the density operator for a coherent state [Sch01, p. 324]. The connection is shown by [SV20]:

$$Q(q,p) = \frac{1}{\pi} \left\langle\alpha\right| \rho \left|\alpha\right\rangle = \int d^2\alpha' P(\alpha') \left\langle\alpha|\alpha'\right\rangle \left\langle\alpha'|\alpha\right\rangle /\pi \tag{2.36}$$

$$= \int d^2\alpha' P(\alpha') |\left\langle\alpha|\alpha'\right\rangle|^2/\pi = \int d^2\alpha' P(\alpha') \underbrace{\mathrm{e}^{-|\alpha-\alpha'|^2}/\pi.}_{=K(\alpha,\alpha')} \tag{2.37}$$

Thus, the Q function is always broader than the corresponding P distribution. Also it is always positive, but it does not allow to easily compute marginals. An illustration of the Husimi function for a coherent state is shown in Fig. 2.4a. Regarding measurements, the Q function can be reconstructed from two-channel homodyne detection. This is explained in detail and applied to polariton emission in Chapter 7.

When using a Gaussian Kernel with half the width as the one above, we obtain the **Wigner function** [LR09]. An image of the Wigner function for a coherent state is shown in Fig. 2.4b. The Wigner function can be negative and therefore is not really a probability distribution. But its marginals correspond to probability distributions of the variables q or p [Sch01, p. 69 - 71]. The Wigner function is historically of importance, but it poses challenges for the reconstruction from measured data. Typically, the data stem from phase-sensitive measurements of the field quadratures with one-channel homodyne detection [SBRF93, BSM97] or, if no phase reference is available, from three homodyne channels using additional phase reconstruction [TLA20]. From these data, the Wigner function can either be calculated using inverse Radon-transformation, delivering huge error margins and possible unphysical features and

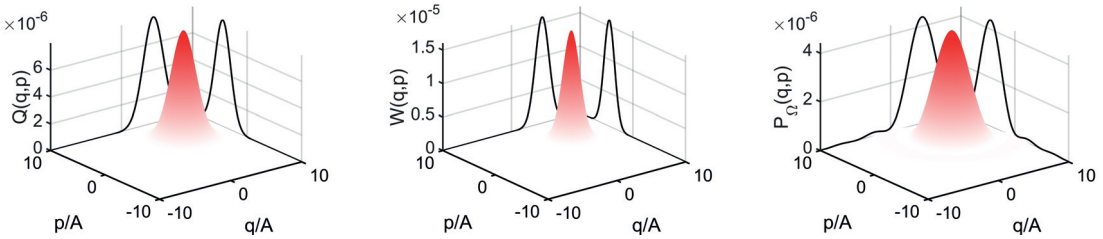

Figure 2.4: Simulated coherent state with mean photon number $|\alpha_0|^2 = 10$, represented (a) by the Husimi function, (b) the Wigner function, and (c) the regularized P function with filter (8.5) and filter parameter $R = 0.7$. The black lines show an integral projection of the functions to the q and p axes.

artifacts, or via maximum-likelihood methods, which do not provide practical means to determine error margins [LR09].

As further improvement, in the last years more, advanced phase-space distributions were developed, mostly by using optimized non-Gaussian kernels. One of them is the **regularized P function**, which can be sampled from homodyne detection data together with error margins, while artifacts can be avoided, making it more practicable than the Wigner function. For this reason, we applied the regularized P function instead of the Wigner function to data from three-channel homodyne detection. Figure 2.4c illustrates the regularized P function for a coherent state, with the filter function given in Eq. (8.5) and a so-called filter parameter $R = 0.7$. Details on this function, the reconstruction process, and its application to polariton emission are found in Chapter 8.

Chapter 3

Theoretical background — Exciton-polaritons in semiconductor microcavities

Due to the strong coupling of light and matter, exciton-polaritons are a natural candidate for semiconductor quantum optics. They emerge when excitons in a semiconductor microcavity are strongly coupled to photons. This chapter explains the fundamentals of exciton-polaritons, following Refs. [GM14, DHY10], and gives a review on previous studies.

3.1 Excitons

In a solid, the possible energies electrons can possess are divided into distinct energy bands. The highest filled band is called valence band, and the band above that conduction band. The size of the energy gap between those bands determines the conductive properties of the material, with the three categories isolator (big gap), metal (no gap) and semiconductor (intermediate gap).
In the semiconductor, this gap can be bridged by optical excitation, when a photon gives enough energy to an electron in the valence band to transfer it to the conduction band. Thereby, the electron leaves an empty place in the valence band, a quasiparticle called hole which is positively charged. The positive hole in the valence band and the negative electron in the conduction band can be bound by Coulomb interaction, similar to a hydrogen atom. Such a pair is a new quasiparticle, called **exciton**. Although excitons consist of fermionic particles, they can be considered as bosons as long as the distance between different excitons is much larger than their Bohr radius a_B [DHY10]. When the electron falls back to the valence band, recombining with the hole, the exciton is destroyed and the energy is emitted as a photon again.

The exciton energy dispersion, depending on the wave vector $\vec{k}$, can be written as

$$E_n(\vec{k}) = E_g - E_X + \frac{\hbar^2 \vec{k}^2}{2m_{\text{exc}}}, \tag{3.1}$$

with the band gap E_g, the binding energy E_X and the mass m_{exc} [GM14].

In solids, excitons are only weakly bound because dielectric screening of the electrical field reduces the strength of the Coulomb interaction. Therefore, they possess binding energies on the order of 1 – 100 meV [HH77] and their Bohr radius a_B extends over several unit cells of the crystal. These weakly bound excitons are called Wannier-Mott excitons, in contrast to the stronger bound Frenkel excitons in organic and molecular semiconductors.
The Bohr radius directly influences the interaction strength between excitons and light because the oscillator strength is proportional to a_B^{-3} [DHY10]. Thus, a decrease of the Bohr radius is desirable for strong coupling to light. This can be achieved by using quantum wells instead of bulk material.
A quantum well is a thin layer of a semiconductor, with a thickness comparable to a_B, placed between two layers of another material with a larger band gap. Thus, the motion of excitons is confined in the direction perpendicular to the layer (denoted as z direction). This confinement leads to a reduced Bohr radius, and therefore an enhanced interaction strength with light. Also, the total exciton energy is enhanced compared to the bulk due to the confinement energy, which can be on the order of several 100 meV and increases with decreasing quantum well thickness [MLC92].
Moreover, the anisotropy in z direction breaks momentum conservation in this direction. Therefore, the momentum of interchanging photons and excitons needs only to be equal in lateral direction. This means that the lateral wavenumber $k_{||}$ has to be equal for exciton and photon but k_z can be arbitrary, improving optical accessibility. But there is a catch, because with the smaller length of the material in z direction, the spatial overlap with the light field is reduced. Thus, for ultimately stronger light-matter coupling, also the light field should be confined in z direction with help of a microcavity.

3.2 Microcavity

A microcavity, basically, is created by placing two mirrors around an optical medium — in this case, a semiconductor quantum well —, confining the light field in between. This has two beneficial effects: it enhances the spatial overlap between material and light field, and it keeps the photons longer inside the material. Without a cavity, a photon would quickly escape to the outside after only a few interactions with excitons. But between the two mirrors, photons are reflected again and again like in an interfer-

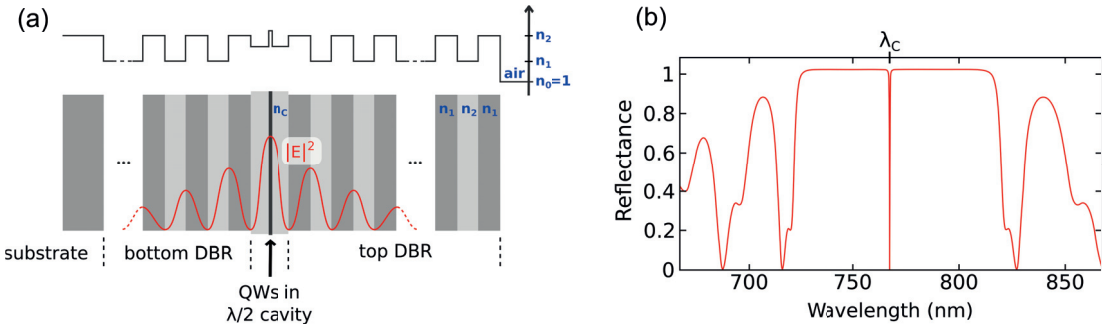

Figure 3.1: (a) Structure of a microcavity. The distributed Bragg reflector (DBR) layers have alternating refractive indices n_1 and n_2. In between lies the cavity with refractive index n_c and optical length $\lambda_c/2$, containing the quantum wells. This structure leads to a concentration of the electrical field in the cavity, depicted in red. (b) Reflectivity spectrum of a microcavity. Due to the DBRs, a stop band with high reflectivity is formed. For excitation, light can permeate into the structure either resonantly at the design wavelength λ_c or non-resonantly at one of the lower-wavelength Bragg minima outside the stop band. Both images are taken from [Ber21].

ometer, interacting multiple times. Thus, excitons and photons interchange repeatedly, a photon creating an exciton, which recombines and creates a photon, and so on. When the lifetime of a photon in the cavity is sufficiently long, the regime of strong coupling is achieved.

In reality, the two mirrors are so-called distributed Bragg reflectors (DBR), consisting of many layers with alternating high and low refractive indices and an optical thickness of $\lambda/4$. The Bragg effect causes destructive interference for wavelengths in a certain range called stop band, making the structure highly reflective in this range. Between the two mirrors is the cavity layer with the quantum wells and an optical thickness of $\lambda_c/2$. Consequently, at the design wavelength λ_c, the transmission is sharply increased and the electrical field is concentrated around the center of the cavity with a highly enhanced amplitude compared to free space. A scheme of the structure and the electrical field is shown in Fig. 3.1.

In order to create excitons optically, the excitation light, typically from a laser, has to penetrate into the structure. This is only possible at wavelengths with low reflectivity, i.e. either at the design wavelength λ_c or at one of the lower-wavelength Bragg minima outside the stop band. The first case is called resonant excitation, the latter one non-resonant excitation. Only non-resonant excitation was used in this work. This excitation process is discussed in detail in Section 3.4.

The energy dispersion of the cavity is given by:

$$E_{\mathrm{Cav}} = \frac{\hbar c}{n_c}\sqrt{k_z^2 + k_{||}^2}, \tag{3.2}$$

with reduced Planck's constant $\hbar$ and the orthogonal wave vector $k_z = n_c 2\pi/\lambda_c$. For $k_{||} \ll k_z$, this simplifies to a parabolic energy dispersion:

$$E_{\mathrm{Cav}} \approx E_{\mathrm{Cav}}(k_{||} = 0) + \frac{\hbar^2 k_{||}^2}{2m_{\mathrm{Cav}}}, \tag{3.3}$$

with the cavity-photon effective mass

$$m_{\mathrm{Cav}} = \frac{E_{\mathrm{Cav}}(k_{||} = 0)}{c^2/n_c^2}. \tag{3.4}$$

The cavity-photon effective mass is typically five orders of magnitude smaller than the bare electron mass [DHY10], resulting in a much more curved energy dispersion than the one of the exciton alone.

The quality of a microcavity is described with the Q factor

$$Q \equiv \frac{\lambda_c}{\Delta\lambda_c} = 2\pi \frac{c}{\lambda_c} \Delta\tau_{\mathrm{Cav}}, \tag{3.5}$$

with the full width half maximum $\Delta\lambda_c$ in the reflectance spectrum, the speed of light c and $\Delta\tau_{\mathrm{Cav}}$ the average lifetime of a photon in the cavity [KBML17]. The Q factor corresponds to the average number of roundtrips a photon can travel in the cavity before it escapes. This means 20 000 roundtrips for the sample investigated in this work, sufficient to facilitate strong coupling.

3.3 Polariton dispersion

As we have seen, using a quantum well in a microcavity enhances the oscillator strength of excitons and leads to a longer lifetime of photons in the cavity. Both effects are expressed in the exciton-photon dipole interaction strength (which is nonzero only for excitons and photons having the same $k_{||}$) [SFW98],

$$2g_0 = \hbar\Omega \approx 2\hbar \sqrt{\frac{2\Gamma_0 c N_{\mathrm{QW}}}{n_c L_{\mathrm{eff}}}}, \tag{3.6}$$

with the Rabi frequency Ω representing the exchange rate between exciton and photon. N_{QW} is the number of quantum wells in the cavity, L_{eff} is the effective length of the cavity, which is inversely proportional to the cavity quality factor, and Γ_0 is proportional to the exciton oscillator strength per unit area. As we will see, strong coupling occurs if $g_0 \gg (\gamma_{\mathrm{cav}} - \gamma_{\mathrm{exc}})/2$, with γ_{cav} and γ_{exc} being the decay rates of the photons and the excitons, respectively. The following derivation is based on Ref. [DHY10].
Mathematically, strong coupling occurs when the Hamiltonian of the system can be diagonalised with new eigenvectors, being superpositions of the prior, uncoupled eigenvectors. In our case, the uncoupled modes are photons, expressed with photon ladder

operators $\hat{a}_{k_{||}}$, and excitons with exciton ladder operators $\hat{b}_{k_{||}}$. The Hamiltonian consists of the uncoupled parts, $\hat{H}_{\mathrm{Cav}}$ and $\hat{H}_{\mathrm{exc}}$, which simply depend on the number of excitations in each subsystem, and the interaction part $\hat{H}_I$ (when using the rotating wave approximation, discarding terms where energy conservation is violated):

$$\begin{aligned}\hat{H} &= \hat{H}_{\mathrm{Cav}} + \hat{H}_{\mathrm{exc}} + \hat{H}_I \\ &= \sum E_{\mathrm{Cav}}(k_{||},k_z)\hat{a}^{\dagger}_{k_{||}}\hat{a}_{k_{||}} + \sum E_{\mathrm{exc}}(k_{||})\hat{b}^{\dagger}_{k_{||}}\hat{b}_{k_{||}} + \sum g_0(\hat{a}^{\dagger}_{k_{||}}\hat{b}_{k_{||}} + \hat{b}^{\dagger}_{k_{||}}\hat{a}_{k_{||}}).\end{aligned} \tag{3.7}$$

Because of the interaction term, the modes $\hat{a}_{k_{||}}$ and $\hat{b}_{k_{||}}$ are not eigenmodes of the system anymore. To get new eigenmodes, the Hamiltonian can be diagonalized via the Hopfield-Bogoliubov transformations:

$$\hat{P}_{k_{||}} = X_{k_{||}}\hat{b}_{k_{||}} + C_{k_{||}}\hat{a}_{k_{||}}, \tag{3.8}$$

$$\hat{Q}_{k_{||}} = -C_{k_{||}}\hat{b}_{k_{||}} + X_{k_{||}}\hat{a}_{k_{||}}. \tag{3.9}$$

This leads to a new, diagonalized Hamiltonian

$$\hat{H}_{\mathrm{pol}} = \sum E_{\mathrm{LP}}(k_{||})\hat{P}^{\dagger}_{k_{||}}\hat{P}_{k_{||}} + \sum E_{\mathrm{UP}}(k_{||})\hat{Q}^{\dagger}_{k_{||}}\hat{Q}_{k_{||}}, \tag{3.10}$$

with new annihilation operators $\hat{P}_{k_{||}}$,$\hat{Q}_{k_{||}}$ for the resulting eigenmodes. These eigenmodes can be seen as new elementary excitations or quasiparticles of the system, being linear superpositions of excitons and photons with the same in-plane wave number $k_{||}$. Thus, we cannot consider excitons and photons existing separately anymore, but they are contributing simultaneously to the system. A similar effect is also known in classical mechanics when coupling two harmonic oscillators, e.g. two pendulums connected by a spring, which then oscillate in two normal modes.
The new quasiparticles are called polaritons and are bosons because excitons and photons are bosons as well. The factors X and C, called Hopfield coefficients, determine the relative proportion of photon and exciton in the polariton. They depend on the difference between cavity and exciton energy $\Delta E(k_{||}) = E_{\mathrm{Cav}}(k_{||}) - E_{\mathrm{exc}}(k_{||})$:

$$|X_{k_{||}}|^2 = \frac{1}{2}\left(1 + \frac{\Delta E(k_{||})}{\sqrt{\Delta E(k_{||})^2 + 4g_0^2}}\right), \tag{3.11}$$

$$|C_{k_{||}}|^2 = \frac{1}{2}\left(1 - \frac{\Delta E(k_{||})}{\sqrt{\Delta E(k_{||})^2 + 4g_0^2}}\right). \tag{3.12}$$

The new eigenenergies of the system are

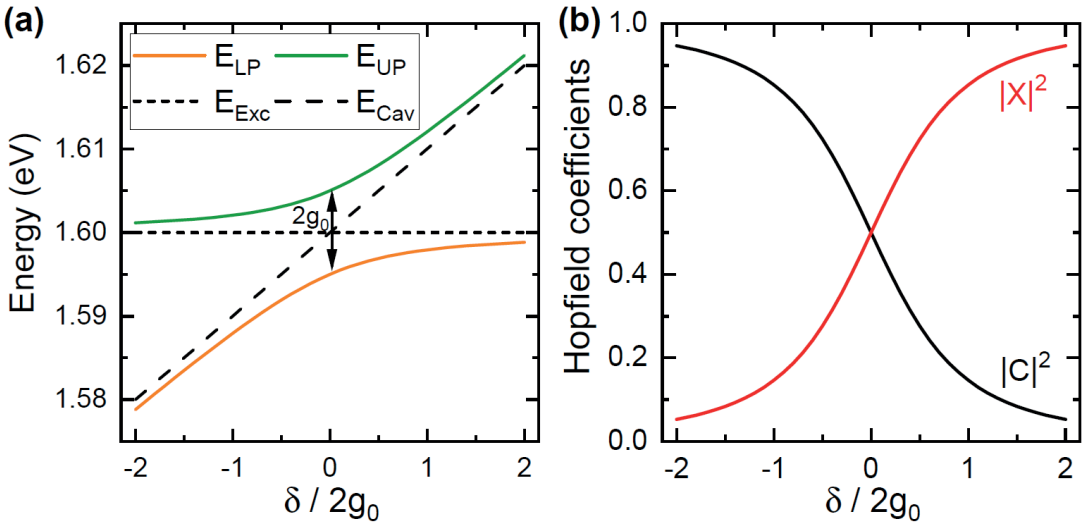

Figure 3.2: (a) Detuning-dependence of the polariton energies at $k_{||} = 0$. The detuning is shown in units of the Rabi splitting $2g_0$. At zero detuning, the cavity and exciton modes cross each other, whereas the two polariton modes anticross, with an energy splitting of $2g_0$. (b) Detuning-dependence of the Hopfield coefficients at $k_{||} = 0$. Both images from [Ber21].

$$E_{\mathrm{LP,UP}}(k_{||}) = \frac{1}{2}\left[E_{\mathrm{exc}}(k_{||}) + E_{\mathrm{Cav}}(k_{||}) \pm \sqrt{4g_0^2 + (E_{\mathrm{exc}}(k_{||}) - E_{\mathrm{Cav}}(k_{||}))^2}\right] \tag{3.13}$$

Obviously, if the coupling strength g_0 was zero, the equation would return the energies of the initial eigenmodes E_{exc} and E_{Cav}, but for finite g_0, we obtain new eigenenergies. The eigenmode with higher energy is called upper polariton (UP) and the other one lower polariton (LP). In practice, only the lower polariton is relevant, being the groundstate of the system and the most populated.

Let us finally derive the exact condition for strong coupling. When taking into account the decay rate of photons γ_{cav} due to imperfect mirrors and the nonradiative decay rate of excitons γ_{exc}, the eigenenergies are

$$E_{\mathrm{LP,UP}}(k_{||}) = \frac{1}{2}\Big[E_{\mathrm{exc}}(k_{||}) + E_{\mathrm{Cav}}(k_{||}) + i(\gamma_{\mathrm{cav}} + \gamma_{\mathrm{exc}}) \pm \sqrt{4g_0^2 + [E_{\mathrm{exc}}(k_{||}) - E_{\mathrm{Cav}}(k_{||}) + i(\gamma_{\mathrm{cav}} + \gamma_{\mathrm{exc}})]^2}\Big]. \tag{3.14}$$

Consequently, there is an anticrossing at $\Delta E(k_{||}) = 0$ as long as $g_0 \gg (\gamma_{\mathrm{cav}} - \gamma_{\mathrm{exc}})/2$ because only then the square root term has a real value $\neq 0$. Otherwise the material is in the weak-coupling regime.

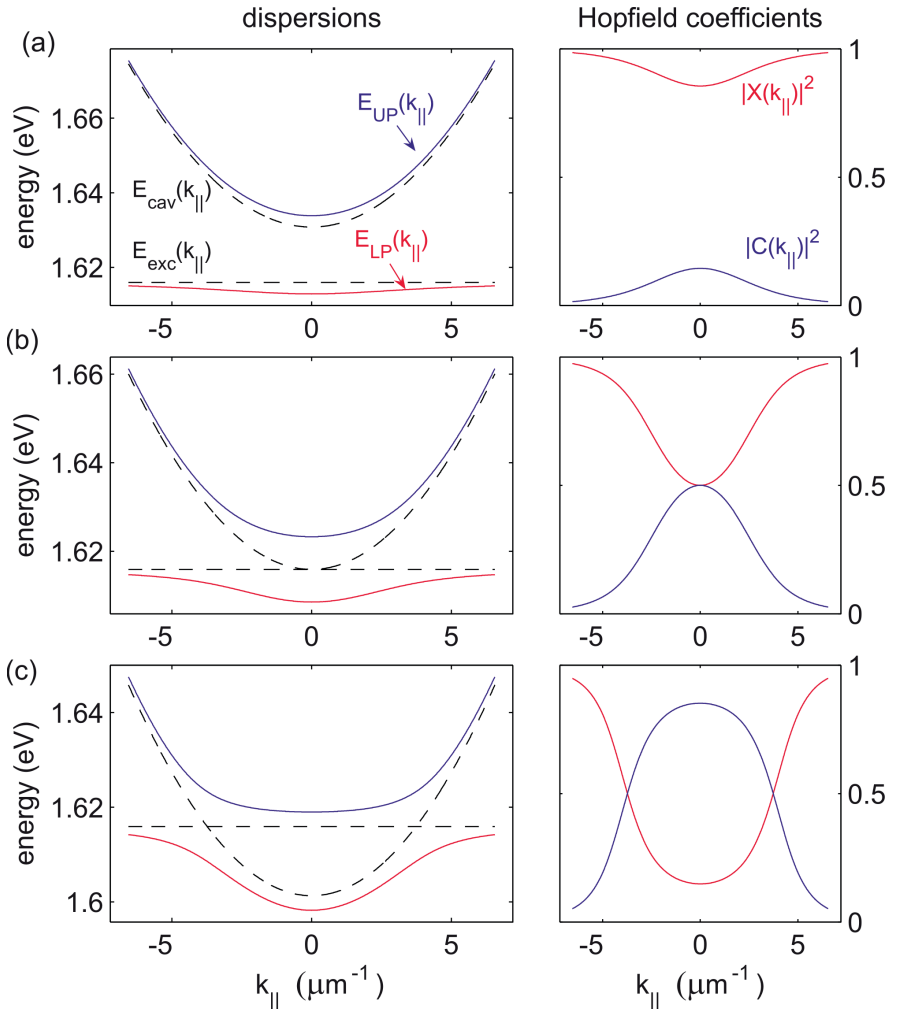

Figure 3.3: Polariton energy dispersions and Hopfield coefficients depending on $k_{||}$, for (a) $\delta = 2g_0$, (b) $\delta = 0$ and (c) $\delta = -2g_0$. The Hopfield coefficients X and C indicate the contributions of exciton and photon, respectively, for the lower polariton and vice versa for the upper polariton. The parabolic exciton dispersion seems to be flat in the depicted range of $k_{||}$ because the much higher exciton mass leads to a much smaller curvature of its dispersion. Image from [DHY10].

As we have seen, the Hopfield coefficients and the new eigenergies depend on the difference between cavity and exciton energy. We discuss this dependence more in detail by defining the detuning between cavity energy and exciton energy at $k_{||} = 0$,

$$\delta = E_{\mathrm{Cav}}(k_{||} = 0) - E_{\mathrm{exc}}(k_{||} = 0). \tag{3.15}$$

In practice, the exciton energy is determined by the bandgap of the material. But the cavity energy can be changed by varying the thickness of the cavity layer across the sample, providing different detunings. Figure 3.2(a) shows the dependence of the polariton energies at $k_{||} = 0$ on the detuning.
Obviously, the minimum energy splitting between LP and UP is reached for zero detun-

ing, having the value $2g_0$ and being called Rabi splitting. For larger absolute detuning, the LP and UP energies approximate the exciton and cavity energies. This is also reflected in the Hopfield coefficients, which are shown in Fig. 3.2(b).
The effect of the detuning on the polariton dispersions and the Hopfield coefficents for all $k_{||}$ is shown in Fig. 3.3. For positive detuning, the lower polariton is mostly "excitonic" and the upper polariton mostly "photonic". For negative detuning, this behavior is more complex. Here, the LP is more "photonic" and the UP more "excitonic" at $k_{||} = 0$; however, it is the other way around for higher wave vectors.

This also has an effect on polariton effective mass and lifetime: The effective mass is the weighted harmonic mean of exciton and photon mass (because the energy dispersion is inversely proportional to the mass), which can be simplified due to $m_{\mathrm{cav}} \ll m_{\mathrm{exc}}$,

$$m_{\mathrm{LP}} = \left(\frac{|X|^2}{m_{\mathrm{exc}}} + \frac{|C|^2}{m_{\mathrm{cav}}} \right)^{-1} \Rightarrow m_{\mathrm{LP}}(k_{||} = 0) \approx m_{\mathrm{cav}}/|C|^2 \tag{3.16}$$

$$m_{\mathrm{UP}} = \left(\frac{|C|^2}{m_{\mathrm{exc}}} + \frac{|X|^2}{m_{\mathrm{cav}}} \right)^{-1} \Rightarrow m_{\mathrm{UP}}(k_{||} = 0) \approx m_{\mathrm{cav}}/|X|^2. \tag{3.17}$$

Also the lifetimes are affected as the decay rates depend on the Hopfield coefficients,

$$\gamma_{\mathrm{LP}} = |X|^2 \gamma_{\mathrm{exc}} + |C|^2 \gamma_{\mathrm{cav}}, \tag{3.18}$$

$$\gamma_{\mathrm{UP}} = |C|^2 \gamma_{\mathrm{exc}} + |X|^2 \gamma_{\mathrm{cav}}. \tag{3.19}$$

Typically, excitons have a lifetime of about 1 ns and cavity photons about 1 – 10 ps, thus polaritons live longer when they are more excitonic. The polariton lifetimes and masses in turn influence their condensation, which we are going to discuss in the next section.

3.4 Condensation under non-resonant excitation

Since excitons and photons are bosons, polaritons are bosons as well. Therefore, an unlimited amount of polaritons is able to populate the same quantum state. When a critical number of polaritons in the system is exceeded, stimulated scattering may lead to a nonlinear increase of the ground state occupation. This behavior, called **Bose-Einstein condensation**, is also found e.g. in atomic gases [DMA+95, BGM+97], molecules [ZSS+03, JBA+03] and semiconductor excitons [HH77]. But compared to these systems, polaritons can condensate at a relatively high temperature thanks to their relatively small masses, because the critical temperature for condensation of a Bose gas is inversely proportional to the particle mass [Fli18]. The only limit is the temperature at which excitons are destroyed thermally, which can even be room temperature, e.g. for organic semiconductors [CGZ+17], making polariton condensates

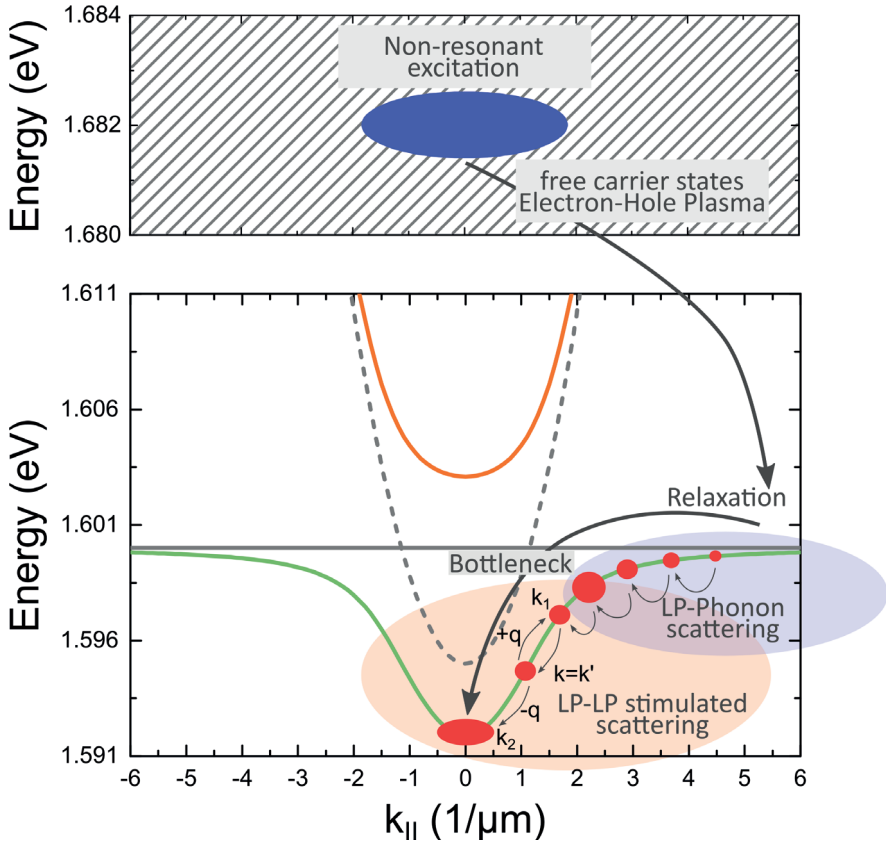

Figure 3.4: Scheme of the condensation process along the lower polariton dispersion for non-resonant excitation. The pump laser creates an electron-hole plasma, which relaxes and forms exciton-like polaritons at high energies and high momenta. These high-energy polaritons relax further due to scattering with phonons, accumulate in the bottleneck region with intermediate $k_{||}$ value and may scatter via polariton-polariton scattering towards the groundstate. The red spheres visualize the density of polaritons at different positions in the dispersion before condensation. Taken from [Sch19].

attractive for research and applications.

However, we investigate a GaAs sample in this thesis, where the exciton binding energy amounts to 4.1 meV [KBML17], corresponding to a temperature of 32 K (according to the kinetic energy in an ideal gas model $E = 3/2 k_B T$ [Nol14] with the Boltzmann constant k_B). Thus, we need cryogenic temperatures for condensation.

The process of condensation is discussed in the following and visualized in Fig. 3.4. We restrict ourselves to the case of nonresonant excitation, which was used in this thesis.

The sample is excited by a laser at much higher energy than the polariton energies, creating large amounts of high-energy electrons and holes. This electron-hole plasma is shown as a cloud at the top of Fig. 3.4.

By scattering with phonons, the electrons and holes lose energy until they bind via Coulomb interaction and form excitons with high energy and $k_{||}$ vector. During this

process, the coherence and polarization properties of the pump laser are lost [KRK$^+$06, KMSL07]. From here, the excitons relax further by scattering with phonons, until they couple to the luminescence light field to become polaritons, in particular lower polaritons (LPs).
These high-energy and high-momentum polaritons form a reservoir until they reach the so-called bottleneck region. At this region of intermediate $k_{||}$ values, the lifetime of the LPs is typically two orders of magnitude longer (because they are more "excitonic") and the density of states much higher than for small $k_{||}$. Therefore, polaritons accumulate in the bottleneck region.
Only when higher polariton densities are created by higher excitation power, they may escape from the bottleneck region towards the groundstate via polariton-polariton scattering. As soon as the groundstate at $k_{||} = 0$ is populated with a number n_0 of polaritons, the scattering rate into this state is enhanced by a factor of $1 + n_0$ due to stimulated scattering. Because of this, at some threshold excitation power, polaritons accumulate nonlinearly in the groundstate and form a condensate. The condensed polaritons then possess a macroscopic wavefunction, forming an order parameter [DHY10]. However, depending on excitation conditions, it is also possible for this process to stop at higher $k_{||}$ values, leading to condensation in excited states. Besides, there are losses due to the finite lifetimes of excitons and photons. Thus, the condensate is not in thermal equilibrium. However, in the case of continuous excitation, which was used here, a stationary polariton distribution exists according to the detailed balance principle [STP$^+$96].

The condensation process described above depends on the excitation conditions, in particular the size and shape of the pump laser spot. As this laser creates the reservoir of high-energy excitons and free carriers, it also shapes a potential that influences in turn the condensing polaritons via repulsive interaction.
The most unfavorable case for condensation at $k_{||} = 0$ is exciting with a small Gaussian spot ($\propto 2\,\mu$m). In this case, the pump laser creates a reservoir with high density, which repels the polaritons due to the repulsive Coulomb interaction, causing them to gain high momentum and condense at $k_{||} \neq 0$ [WCC08].
Since we prefer condensation at $k_{||} = 0$ for good overlap with the local oscillator (see Section 4.1), we need another excitation scheme. One possibility is a rather big pump spot ($\geq 20\,\mu$m), which facilitates condensation around $k_{||} = 0$ [WCC08].
Another option is excitation with a patterned pump spot, e.g. a ring with a diameter on the order of the polariton mean free path, created by an axicon or a spatial light modulator. This has the advantage of separating reservoir and condensate spatially. Via scattering, some polaritons increase their energy and escape while others lose energy and are trapped inside the ring. The latter form a condensate at $k_{||} = 0$; see e.g. [AOK$^+$13].

In this work, we used ring-shaped excitation in Chapter 6 and a relatively large Gaussian spot in Chapters 7 and 8.

3.5 Optical coherence properties of the condensed state

After some state is created in the polariton system, we somehow have to probe it. The particular advantage of polaritons is the one-to-one correspondence between the internal polariton mode and an external photon mode with the same energy and $k_{||}$ [DHY10]. Also, the excitation does not travel through a bulk material until it reaches the surface, but the polaritons couple directly to photons outside of the material. Thus, the energy dispersion $I(E,k_{||})$ of the luminescence measured outside is directly related to the cavity-polariton dispersion curve [HWS+94].
Furthermore, the quantum state of the polariton system is preserved in the emitted light, except for rescaling with some constant [LPR+21], which does not change properties like the quantum coherence. Consequently, the polariton state can be probed just from the emission, opening the path for applying quantum optics methods.
On these grounds, previous studies already investigated coherence properties of the polariton emission like $g^{(1)}$ and $g^{(2)}$. The following paragraphs will summarize their findings and indicate open questions.

One of the indicators of a light state is the equal-time second-order photon correlation $g^{(2)}(0)$ (see Section 2.4). Therefore, many theoretical and experimental studies concentrated on this quantity during the condensation process. Below the condensation threshold, where the thermal phonon bath induces polariton relaxation, most theories predict the thermal value $g^{(2)}(0) = 2$ [HSQ+10, SQ08]. Only in the case of resonant excitation, smaller $g^{(2)}(0)$ was found below threshold, because the polaritons obtained coherence from the pump laser [WDE+17].
For increasing excitation power and beginning condensation, $g^{(2)}(0)$ decreases towards a value close to 1; but in some theoretical studies, another increase is predicted between 1 and 2, staying roughly constant over a larger range of powers; see e.g. [SQ08, HDCT12]. This asymptotic value of $g^{(2)}(0)$ depends on several conditions, one being the noise induced by different modes of the condensate. This can be suppressed, leading to smaller values of $g^{(2)}(0)$, either by spatially confining the sample itself, e.g by using micropillars [KFA+18] and a cavity with lateral confinement [KZW+16], or by spatially filtering the emission [AAB+15]. But also the detuning influences the asymptotic value of $g^{(2)}(0)$ [ATV+11]. Apart from this, the main decoherence sources leading to $g^{(2)}(0) > 1$ are nonresonant polariton-polariton scattering [SQ08, SSQ08] and fluctuations of the reservoir [LKW+08].
Finally, for much higher pump power, the main emission process is not the emission from polaritons in the groundstate anymore, but stimulated emission of photons. This

effect appears as a second threshold and as a jump of the emission energy towards the energy of the bare cavity. Above the second threshold, $g^{(2)}(0)$ drops towards 1, corresponding to conventional photon lasing [TVA$^+$12]. Whether this second threshold corresponds to a breakdown of strong coupling or is caused by a non-Hermitian phase transition within the strong coupling regime is still an open question [HEOL19].
These findings on $g^{(2)}(0)$ leave several unresolved questions. First, there are limitations of the detection methods itself: Most of the experimental studies used a Hanbury-Brown Twiss (HBT) setup and a streak camera. To deliver the correct result, the time resolution of the devices, e.g. of the photo diodes in a HBT setup, should at least match the coherence time of the emission. This is especially a problem below the threshold, where the coherence time is relatively low. However, if the time resolution of the device is known, the measured value can be corrected to obtain the true value; see e.g. [LKW$^+$08, KZW$^+$16].
A further problem of most detection methods is their vulnerability to environmental noise sources, like mechanical vibrations, thermal effects, air turbulence, and stray light entering the detector. These effects are enhanced by the long integration times most detection methods require and might lead to a higher value of $g^{(2)}(0)$ because they make the signal seem more noisy than it actually is.
Besides, not all studies filtered the emission from different polariton condensate modes before detecting them, which means that a mixture of quantum states is measured.
These problems are addressed in Chapter 6, where we performed time-resolved measurements of $g^{(2)}(0)$ of a polariton condensate. But even if perfect detection methods were available, $g^{(2)}(0)$ does not distinguish uniquely between different quantum states. For example, a coherent state gives $g^{(2)}(0) = 1$, but also a particle number eigenstate and a squeezed state, which are all predicted by different theories, approach $g^{(2)}(0) = 1$ for high photon numbers [DWS$^+$02][1]. Thus, more sophisticated methods are needed to gain more complete information about the quantum state.

Another property of interest is the temporal decay of the coherence and the coherence time. For this purpose, previous experimental studies measured the time dependence of the first-order correlation of the light field $g^{(1)}(\tau)$, most of them using Michelson and Mach-Zehnder interferometers. These studies show several influencing factors on the coherence time, among these the excitation conditions. Noise of the exciting laser can diminish the coherence, and therefore a study using a noise-free single-mode excitation laser was one of the first to find relatively high coherence times on the order of 100 ps [LKW$^+$08]. The remaining decoherence mechanism is attributed

[1] For a particle number state, the mean photon number is $\bar{n} = n_0$ and the photon number variance is $\mathrm{Var}(n) = 0$. By inserting this into Eq. (2.18), we get $g^{(2)}(0) = 1 - \frac{1}{n_0}$, which approaches 1 for big n_0. For a squeezed state, under the condition of high amplitudes, we get $g^{(2)}(0) = 1 + \frac{1}{\alpha^2}(\mathrm{e}^{-2r} - 1)$ [Wal83], with coherent amplitude α and squeezing parameter r. Depending on r, this can be greater or less than one, i.e. bunching or anti-bunching, but for big amplitudes, it approaches one.

by this study to polariton number fluctuations and polariton-polariton interactions.
But also interaction with the exciton reservoir may cause decoherence. These interactions can be diminished by trapping the condensate with a patterned pump, whereby even nanosecond coherence times were demonstrated [OTP+21, APA+19, BZS+22]. Also top-hat-shaped pump lasers led to coherence times of up to 90 ps, with increasing pump spot diameter causing longer coherence times [APA+19]. However, Refs. [APA+19, LKW+08] reported a Gaussian temporal shape of $g^{(1)}(\tau)$, which suggests inhomogeneous broadening of the signal, although Ref. [LKW+08] filtered the signal spectrally.
Thus, apart from the excitation conditions, the other influencing factor is the presence of several modes in the signal. A study that employed a spatially confined cavity for single-mode emission [KZW+16] achieved a coherence time on the order of 60 ps with an exponential time decay, indicating a single-mode signal, for small excitation powers close to the threshold. For increasing powers, this study nevertheless found a decrease of the coherence time and a Gaussian decay, which the authors attribute to polariton-polariton interactions and shot noise of the condensate.
To complement these findings, theoretical studies found that polariton-polariton interaction in the groundstate leads to phase diffusion and therefore increased linewidth and decreased coherence time, e.g. Ref. [PT03]. This effect increases with higher number of polaritons in the condensate and leads to inhomogeneous broadening for higher powers, whereas the linewidth is smallest just above threshold (and therefore the coherence time is the longest).
Furthermore, Ref. [HDCT12] distinguishes the effects of resonant and nonresonant scattering: Resonant scattering involves two polaritons from an intermediate state, of which one is scattered to the ground state and the other is scattered to a higher-energy state, whereby total energy and momentum are conserved. In contrast to this, for nonresonant scattering, two polaritons from the groundstate scatter to excited states with opposite momentum, conserving momentum but not energy, which is possible when the energy gap is smaller than the energy broadening. Resonant scattering destroys the coherence more than nonresonant scattering. If lateral confinement leads to a large energy gap between the ground state and the first-excited states, nonresonant scattering is suppressed. In this situation, resonant scattering is the dominant mechanism and the coherence time decreases for higher powers. This might explain the results for higher powers in Ref. [KZW+16]. But if there is no lateral confinement, nonresonant scattering prevails, thus the coherence time stays roughly constant with increasing pump power, and $g^{(1)}(\tau)$ has an exponential decay in the long-time limit.
Additionally, Ref. [WE09] investigates the effect of polariton number fluctuations and found that for high excitation power or for a large size of the condensate, these fluctuations should decay fast, leading to motional narrowing and a slower, exponential decay of $g^{(1)}(\tau)$.

All in all, the main reasons leading to temporal decoherence, found by experiments and theory, are: interaction with the exciton reservoir, which is influenced by the pump spot shape; a multi-mode signal, which can be removed by filtering during detection; and internal effects like polariton number fluctuations, interaction and scattering between polaritons, which depend on lateral confinement and on excitation power.
Consequently, if one wants to measure the "true" temporal decay of the coherence, one should take care of diminishing the influence of the reservoir on the condensate and filter the signal for a single mode. But even if this is possible, Michelson and Mach-Zehnder interferometers deliver only limited information. One only measures the interference of the light field in total, without distinguishing the effects of diffusing phase and decaying amplitude. Also, similar to $g^{(2)}(\tau)$, $g^{(1)}(\tau)$ in itself does not reveal the quantum state of the system.

More properties aside from $g^{(1)}$ and $g^{(2)}$ were studied in Ref. [KSF$^+$18], which used a photon-number-resolving transition edge sensor to measure the emitted photon-number distribution. They observed a monotonous transition from thermal to Poisson distribution with increasing excitation power. Assuming a displaced thermal state, they extracted the thermal and coherent photon numbers. Besides, correlations $g^{(n)}(\tau = 0)$ of all orders could be derived, but not temporally resolved. The correlations decreased monotonously towards one with increasing excitation power.

Another important property is the spatial coherence of the system since long-range spatial order serves as the smoking-gun evidence for demonstrating Bose-Einstein condensation [DP12]. Spatial coherence of polaritons was studied e.g. in Refs. [KRK$^+$06, DSH$^+$07, WFS$^+$10]. This work, though, focuses on temporal coherence and has not measured spatial coherence. Therefore, a more detailed discussion of this property is omitted here for the sake of brevity.

To conclude, many results are already found on coherence properties of polariton condensates. But they still suffer from experimental limitations, and they do not deliver complete information on the quantum state of the condensate. Also, these results lack a unified concept of coherence that applies to both matter and light, e.g. the concept of quantum coherence introduced in Section 2.5. Therefore, this work attempts to fill in some of these gaps and provide methods for future investigations. We did so by employing a different detection method, homodyne detection, which is explained in the next chapter.

Chapter 4

Experimental Methods

The following chapter explains the basic experimental methods that all experiments in this thesis have in common. These methods are homodyne detection (here only in one channel) in Section 4.1 and exciton-polariton spectroscopy in Section 4.2.

4.1 Homodyne Detection

4.1.1 Principle

Homodyne detection is a technique for measuring the field quadratures of a light field, developed by Yuen and Chan [YC83, ACY83]. The idea of the technique is shown in Fig. 4.1. The investigated signal light field is overlapped on a beam splitter with a strong coherent light field, being called local oscillator (LO). On the beam splitter, these fields interfere with each other if they belong to the same spectral, spatial and temporal mode. Thus, one can select the investigated mode of the signal by chosing the LO appropriately. The two mixed beams emanating from the output ports of the beam splitter impinge on the two photodiodes of a balanced photodetector which measures the difference photocurrent. As we show in the following, the resulting difference photocurrent is proportional to the field quadratures of the signal multiplied with the LO amplitude. Thus, the LO acts as an amplifier for the chosen signal mode.

The following derivation of the functioning principle is based on Ref. [LR09]. We start by assuming a signal light field composed of several modes. The electric field operator can be written as a sum of positive- and negative-frequency parts, with the positive part given by

$$\hat{\vec{E}}_S^{(+)}(\vec{r},t) \propto \sum_j \hat{b}_j \vec{\epsilon}_j \exp(\mathrm{i}\vec{k}_j\vec{r} - \mathrm{i}\omega_j t). \tag{4.1}$$

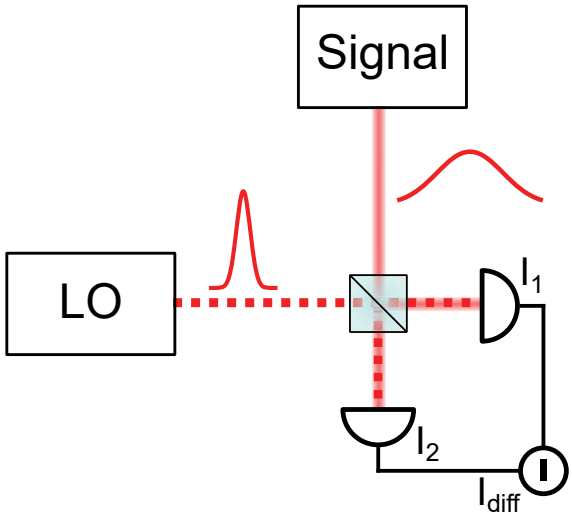

Figure 4.1: Scheme of homodyne detection. A signal beam and a local oscillator beam (LO) interfere on a beam splitter and impinge on a balanced photodetector, whose difference photocurrent $I_{\mathrm{diff}} = I_1 - I_2$ is recorded. Often, the LO has a more narrow spectrum than the signal, effectively selecting only this spectral part for the homodyne measurement.

Here, $\hat{b}_j$ is the annihilation operator of the mode j with polarization $\vec{\epsilon}_j$, wavevector $\vec{k}_j$ and frequency ω_j. We omit prefactors here for sake of simplicity.
The LO field is considered to be a strong coherent pulse

$$\hat{\vec{E}}_L^{(+)}(\vec{r},t) \propto |\alpha_L| \mathrm{e}^{\mathrm{i}\theta_L} \vec{\epsilon}_L v(x,y) g(t) \exp(\mathrm{i}\vec{k}_L\vec{r} - \mathrm{i}\omega_L t), \tag{4.2}$$

having a spatiotemporal mode given by $v(x,y)g(t)$. Because of the high intensity, we assume a classical coherent-state amplitude $|\alpha_L|\mathrm{e}^{\mathrm{i}\theta_L}$, with phase θ_L.
When signal and LO field meet on a beam splitter set to 50:50 reflection and transmission, the overlapped fields exiting the beam splitter at the different exit ports are given by

$$\hat{\vec{E}}_1^{(+)} = \frac{1}{\sqrt{2}} \left(\hat{\vec{E}}_L^{(+)} + \hat{\vec{E}}_S^{(+)} \right); \tag{4.3}$$

$$\hat{\vec{E}}_1^{(+)} = \frac{1}{\sqrt{2}} \left(\hat{\vec{E}}_L^{(+)} - \hat{\vec{E}}_S^{(+)} \right). \tag{4.4}$$

These fields hit the photodetectors, creating a number of photoelectrons proportional to the intensity

$$N_i \propto \int\int \hat{\vec{E}}_i^{(-)} \hat{\vec{E}}_i^{(+)} \mathrm{d}x\mathrm{d}y\mathrm{d}t, \tag{4.5}$$

with $i \in 1,2$. The integration is performed over the detector area and the measurement time. In the case of a pulsed LO, the measurement time $\Delta\tau$ is given by the pulse duration. The difference of the number of photoelectrons between both detectors is

$$N_{\text{diff}} = N_1 - N_2 \propto \int\int \left(\hat{\vec{E}}_L^{(-)} \hat{\vec{E}}_S^{(+)} + \hat{\vec{E}}_S^{(-)} \hat{\vec{E}}_L^{(+)} \right) \mathrm{d}x\mathrm{d}y\mathrm{d}t. \tag{4.6}$$

Inserting the expressions for the fields gives

$$N_{\text{diff}} \propto |\alpha_L|(\hat{a}\mathrm{e}^{-\mathrm{i}\theta_L} + \hat{a}^\dagger \mathrm{e}^{\mathrm{i}\theta_L}). \tag{4.7}$$

Using the correct prefactors, the line above represents an equation instead of a proportionality. Here, $\hat{a}$ represents the detected signal mode having the same spectral and spatial shape, wave vector and polarization as the LO. This mode is determined by

$$\hat{a} = \sum_j c_j \hat{b}_j, \tag{4.8}$$

with the Fourier coefficients for the LO pulse

$$c_j = \int\int \vec{\epsilon}_j \vec{\epsilon}_L^* v^*(x,y) g^*(t) \mathrm{e}^{\mathrm{i}(\vec{k}_j - \vec{k}_L)\vec{r}} \mathrm{e}^{-\mathrm{i}(\omega_j - \omega_L)t} \mathrm{d}x\mathrm{d}y\mathrm{d}t. \tag{4.9}$$

Now we insert the definition of the phase-dependent field quadrature (2.32) into Eq. (4.7). We find that the number of photoelectrons is proportional to the field quadrature, with the quadrature axes of the coordinate system chosen to be in-phase with the LO and orthogonal to it, respectively.

$$N_{\text{diff}} = |\alpha_L| \frac{1}{A} \hat{q}_{\theta_L}. \tag{4.10}$$

Experimentally, the number of photoelectrons can be determined by temporally integrating the photocurrent, i.e. numerically integrating the recorded signal over a certain time window. More about data processing can be found in Subsection 4.1.3.

In order to remove the LO amplitude $|\alpha_L| = \sqrt{\bar{n}_L}$ from the measured data, we have to measure it beforehand. For such a measurement, one blocks the signal beam so that only vacuum enters the signal port. In this case, the mean value of the squared number of photoelectrons is [RC13]

$$\langle N_{\text{diff}}^2 \rangle_{\text{vac}} = |\alpha_L|^2 \langle 0|(\hat{a}\mathrm{e}^{-\mathrm{i}\theta_L} + \hat{a}^\dagger \mathrm{e}^{\mathrm{i}\theta_L})^2|0\rangle = |\alpha_L|^2 \langle 0|\hat{a}\hat{a}^\dagger|0\rangle = |\alpha_L|^2. \tag{4.11}$$

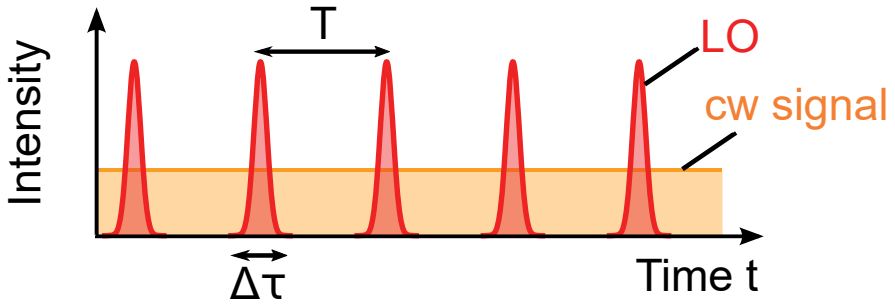

Figure 4.2: Illustration of the time scales in a homodyne detection experiment. The red peaks and the orange line symbolize the LO pulses and a cw signal, respectively. The duration of one LO pulse $\Delta\tau$ is the time over which one quadrature value is averaged. The distance T between two pulses determines the sampling rate $1/T$ with which the quadratures are recorded.

Since the mean value $\langle N_{\text{diff}}\rangle_{\text{vac}}$ is zero for vacuum, we get the standard deviation

$$\Delta N_{\text{diff,vac}} = \sqrt{\langle N_{\text{diff}}^2\rangle_{\text{vac}} - \langle N_{\text{diff}}\rangle_{\text{vac}}^2} = \sqrt{\langle N_{\text{diff}}^2\rangle_{\text{vac}}} = |\alpha_L|. \tag{4.12}$$

Thus, the standard deviation of the photoelectron number obtained from a vacuum measurement can be used to normalize the data from a signal measurement via

$$\hat{q}_{\theta_L} = N_{\text{diff,sig}} \frac{A}{\Delta N_{\text{diff,vac}}}. \tag{4.13}$$

All in all, homodyne detection enables phase-sensitive measurements of the field quadratures of a light field. However, in cases where the signal phase fluctuates with respect to the LO on the time scale of the experiment, only a phase-averaged measurement is possible. This problem can be overcome by using more detection channels to reconstruct the phase between channels, as explained in Chapter 8.
Furthermore, homodyne measurements intrinsically yield temporal resolution when using a pulsed LO. For better understanding, the temporal properties of the signal and LO are illustrated in Fig. 4.2. The red peaks represent the LO pulses while the orange line shows a continuous wave (cw) signal. During each pulse, the signal is amplified by the LO and photoelectrons in the detector are created, whose total number corresponds to one quadrature value up to a scaling factor. Thus, the quadrature value is measured with a time resolution given by the LO pulse duration $\Delta\tau$. A better time resolution is not possible since the detector electronics — being slower than our LO pulse length — can not differentiate between electrons being created in the beginning, the middle or the end of the pulse but mixes them all together. Furthermore, the time T between different pulses determines the sampling rate $1/T$ with which the quadratures are measured.
Note that if one used a cw LO instead of a pulsed one, both T and $\Delta\tau$ would be limited

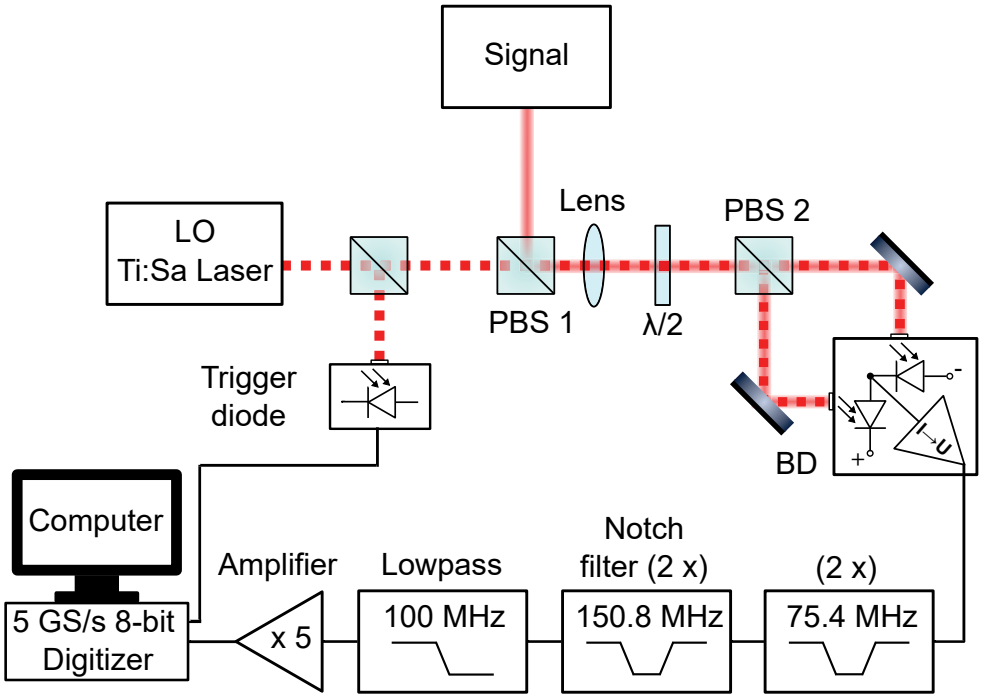

Figure 4.3: Scheme of the homodyne detection setup in one channel. LO: Local oscillator; PBS: polarizing beam splitter; $\lambda/2$: half-wave plate; BD: balanced detector.

by the sampling rate of the detector. Especially $\Delta\tau$ would be much higher, leading to a much worse time resolution.
Technical details of the setup are described in the next section.

4.1.2 Implementation

Our homodyne detection setup is shown schematically in Figure 4.3. This setup is also described in Ref. [LTA18]. Details on handling and aligning the setup and a characterization of the detectors can be found in Ref. [The18].
The local oscillator (LO) and the signal are combined on a polarizing beam splitter (PBS 1). One has to align the two beams carefully with the help of a camera to achieve good overlap in real space and k space. After this is assured, the combined beam is focused onto the balanced detector (BD) by a lens with 30 cm focal length. A half-wave plate ($\lambda/2$) sets the splitting ratio of the combined beam on the second polarizing beam splitter (PBS 2) to roughly 50 % reflection and transmission for both LO and signal. The half-wave plate can be fine-tuned with a micrometer screw such that the two photodiodes of the detector deliver an equal average photocurrent. This is necessary to account for slightly different properties of the two photodiodes. Also, the half-wave plate rotates the polarizations of the LO and signal beam by 45° so that they are able to interfere. The difference photocurrent is converted to a voltage in the detector and

subsequently amplified and digitized.
As explained in the previous subsection, the time resolution of this setup is determined by the temporal properties of the LO. On the one hand, the temporal resolution $\Delta\tau$ is given by the duration of one LO pulse, and on the other hand, the sampling rate for recording the signal quadratures corresponds to the LO pulse repetition rate $1/T$.
Our LO originates from a MIRA 900 Ti:Sapphire laser from the company Coherent with an adjustable wavelength between 700 and 980 nm, adaptable to the signal wavelength. The pulse repetition rate is 75.4 MHz, corresponding to $T = 13.3$ ns. The pulses have a minimum duration of $\Delta\tau = 130$ fs. However, with a grating-slit combination (not shown in the image), the LO spectrum can be narrowed, providing longer pulse durations. This is beneficial for detecting narrow-line continuous-wave signals. With a longer LO pulse duration, more signal photons can be detected in total, as long as the signal spectrum is fully covered by the LO spectrum. Also, for signals with a broad spectrum, a narrower LO spectrum selects only the parts of the signal spectrum one is interested in.
The LO power can be adjusted by a $\lambda/2$-PBS combination (not shown) and is measured before the last beam splitter PBS 2. The power is usually set to a value between 2 and 5.0 mW. A small fraction of the LO beam is split off and directed towards a photodiode (model HCA-S-200M-SI-FS manufactured by FEMTO Messtechnik), which sends a trigger signal to the digitizer.
While the time scales of the experiment are determined by the LO, they may be limited by the detection and data acquisition setup. Therefore, all components need to possess a sufficient bandwidth. For the detection, we use a balanced photodetector provided by the company FEMTO Messtechnik with a bandwidth of 100 MHz. The detector is based on the model HCA-S but was customized for our application. It contains two Si-PIN photodiodes and a transimpedance amplifier with a gain of 5 kV/A, converting the difference photocurrent into voltage. We determined its common mode rejection ratio to be 69 dBm and verified shot-noise limited performance for LO powers above 1 mW.
Subsequently, signal components at the LO repetition rate and its higher harmonics are removed from the voltage signal by two notch filters at 75.4 MHz and two notch filters at 150.8 MHz from Rittmann-HF-Technik and a 100 MHz lowpass filter from Crystek. The filtered signal is then amplified with a voltage amplifier SR445 from Stanford Research Systems, having a bandwidth of 300 MHz. Finally, the signal is digitized by the M4i.2234-x8 digitizer from Spectrum Instrumentation, providing sampling rates of up to 5 GS/s at 8 bit resolution. Such a high sample rate is only achieved for one channel, though. When recording data from several detectors simultaneously, the sampling rate is divided between the different channels (2.5 GS/s for two channels, 1.25 GS/s for three to four channels).

4.1.3 Data processing

As explained in Subsection 4.1.1, we need a vacuum measurement without signal in order to normalize measurements where signals are recorded. In practice, a custom Labview program is used to acquire a vacuum measurement and a signal measurement subsequently and store each in a raw-data file with adjustable file size. From these two raw-data files, we compute the normalized signal quadratures with custom-written Matlab functions; see Appendix A.

One crucial step in this computation is a numerical summation of the recorded voltage values over a specified time window around each LO pulse. Since the voltage values are proportional to the difference photocurrent recorded by the detector, the sum of them is proportional to the total number of created photoelectrons, which in turn is proportional to one value of the signal field quadrature averaged over the LO pulse duration.

Let us mention here that instead of integrating the recorded voltages numerically after data acquisition, one could also perform direct electronic integration of the photocurrent with help of a built-in capacitor in the detector. Such a scheme was used e.g. in Ref. [RC13]. However, such a RC circuit is too slow to work at 100 MHz since the capacitor needs time to decharge.

After numerically obtaining the quadrature values q_i, one possible problem is that values q_i and q_{i+1} belonging to subsequent LO pulses might be correlated. The reason is ringing of the detectors and the electronic filters. Such correlations can be removed numerically [KBM$^+$12, The18]; see Appendix A. However, this removing only works if the quadratures do not possess any physical correlations, otherwise these real correlations would be removed as well. Such physical correlations between subsequent quadratures are present if there is a fixed phase relation between signal and LO that is preserved during the time between one LO pulse and the next. For light sources emitting independently of the LO, the phase between signal and LO is randomized if the signal coherence time is smaller than the time between two LO pulses. But in experiments where the signal is in some way derived from the LO, e.g. by optical parametric amplification, there exists a fixed phase relation and the correlation removal scheme should not be used.

4.2 Exciton-polariton spectroscopy

This section explains the setup for performing exciton-polariton spectroscopy.

4.2.1 Sample

The investigated sample is a planar GaAs-based microcavity (identification number M3396-9.2) that has been grown at the University of Würzburg by Christian Schnei-

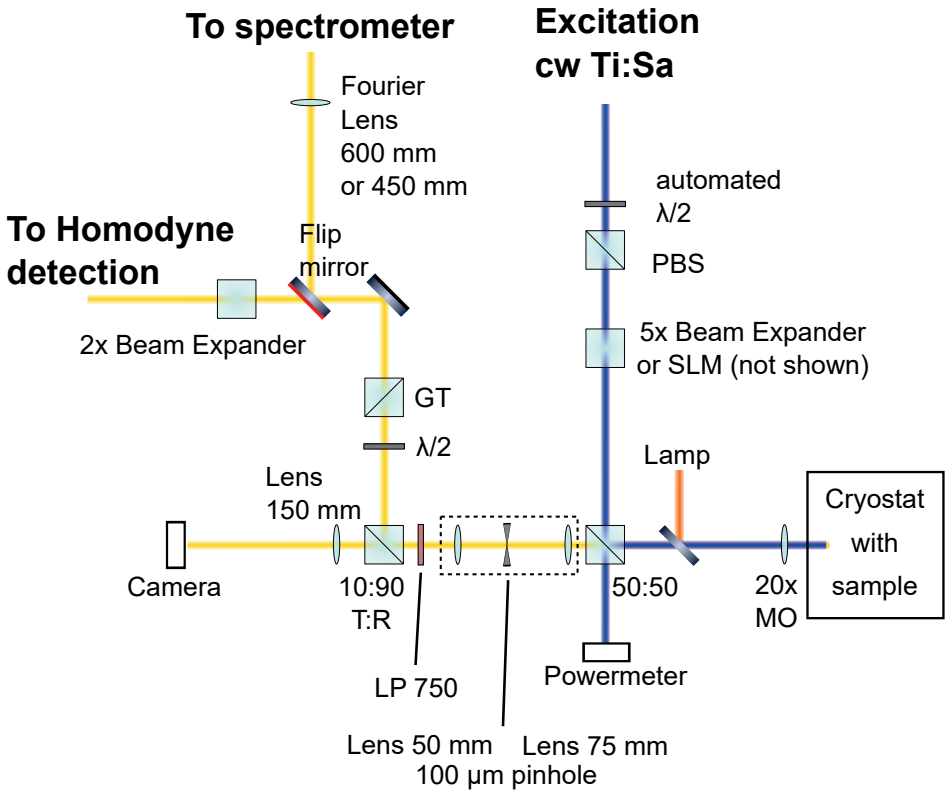

Figure 4.4: Setup for polariton spectroscopy. $\lambda/2$: Half-wave plate; PBS: polarizing beam splitter; 50:50: beam splitter with 50 % transmission and 50 % reflection; MO: microscope objective; LP 750: longpass for transmission above 750 nm; 10:90: beam splitter with 10 % transmission and 90 % reflection; GT: Glan-Thompson prism.

der and Sven Höfling via molecular beam epitaxy. The microcavity consists of two distributed-Bragg reflectors with 32 top and 36 bottom layer pairs of $Al_{0.2}Ga_{0.8}As$ and AlAs, having a quality factor of about 20 000. Between the DBRs lies a $\lambda/2$ cavity, containing four GaAs quantum wells. The Rabi splitting $2g_0$ of the sample is 9.5 meV. The detuning varies along one axis of the sample due to its wedged shape. A detailed characterization of the sample can be found in Refs. [MBA+20, Ber21]. Also, a characterization conducted within this thesis is shown in Chapter 5.

4.2.2 Setup

Figure 4.4 depicts the setup for polariton spectroscopy.

The sample is held in a flow cryostat at a temperature of 10 K. The cryostat can be moved in horizontal and vertical direction in order to find a suitable sample spot. Besides, in horizontal direction, the sample has a wedge for varying the exciton-cavity detuning. The used detuning is explicitly stated in the results chapters and is always negative.

The sample is excited nonresonantly at the first minimum of the stop band with a tunable continuous-wave Ti:Sa laser (SolsTiS 2000 PSX-XF manufactured by M Squared Lasers). This laser provides single-mode light with a very narrow linewidth of $< 50\,\mathrm{kHz}$. The required wavelength depends on the sample spot and is 735.55 nm for most of the experiments presented here, if not indicated otherwise. Remarkably, in the case of nonresonant excitation, the coherence of the exciting laser is completely lost during the energy relaxation process of the polaritons. Thus, the polaritons do not inherit coherence from the pump laser [KRK$^+$06, KMSL07].
As explained in Section 3.4, the excitation spot should be either ring-shaped or large to enable condensation at $k = 0$. For the experiment in Chapter 6, a Spatial Light Modulator (SLM, PLUTO-2 from HOLOEYE) is used to create a ring-shaped excitation spot with a diameter of 12 µm on the sample. Unfortunately, this SLM also modulates the intensity of the beam, which is part of the investigation in Chapter 6, but unwanted in later experiments. Therefore, in Chapter 7 and 8, the SLM is removed. Instead, the exciting beam is transformed with an adjustable 5x beam expander (GBE05-B from Thorlabs) to create a large Gaussian spot with a diameter of 70 µm full width at half maximum (FWHM) on the sample. By fine-tuning the beam expander while observing the polariton dispersion, one can find an optimal beam size for condensation at $k = 0$. The excitation beam is reflected by a 50:50 beam splitter towards the cryostat. The excitation power is controlled by an automatized half-wave plate and measured behind the unused exit port of the beam splitter. A 20 x microscope objective (MO, M Plan Apo NIR 20X Mitutoyo with 10 mm effective focal length) focuses the beam onto the sample. The same MO also collects and collimates the polariton emission. This has the advantage that excitation and emission belong to the same microscopic region of the sample. Additionally, light from a whitelight lamp can be reflected via a glass plate onto the sample for illumination.
Half of the collimated emission passes the 50:50 beam splitter. A longpass filter transmits only light above 750 nm to remove the excitation laser from the beam. Then, a second beam splitter (10:90 T:R) reflects 90 % of the emission towards the analysis section of the experiment while a small part is transmitted and focused with a lens onto a camera to monitor the spatial properties of the emission. This is useful for finding a sample position where condensation of polaritons occurs in a single bright spot. Otherwise, there are regions on the sample where impurities cause unstable condensation in several spots. While the interplay of these spots might be interesting, it is outside the scope of this work. To further remove the emission from neighboring spots, a telescope with a pinhole may be inserted before the 10:90 beam splitter to spatially filter the emission. This is only used in Chapter 7 and 8. In these experiments, a telescope consisting of a 75 mm focusing lens, a 100 µm pinhole and a 50 mm collimating lens delivers a beam size that matches the LO size roughly for maximum homodyne signal. This spatial filtering corresponds to a region with 13 µm diameter on the sample —

given by $\varnothing_{\text{pinhole}}\, f_{\text{MO}}/f_{\text{focusing lens}}$ — and to a k space region around $k = 0$ with a FWHM of 1 µm^{-1}.
After the 10:90 beam splitter, the polarization of the emission can be chosen with a half-wave plate and a Glan-Thompson prism. Then, the emission propagates towards the homodyne detection setup or via a flip mirror towards the spectrometer.
On the path to the spectrometer, a 600 mm or 450 mm lens (Fourier lens) can be inserted for imaging the k space. The focal length of this lens has to match the distance to the last optical element collimating the beam, which is either the MO or the last lens of the telescope. The position of the lens should be fine-tuned in order to achieve a sharp Fourier image. When this lens is omitted, the real space of the sample can be observed with the spectrometer. Subsequently, a 400 mm lens — not shown in the Figure — focuses either the Fourier image or the real-space image onto the spectrometer camera. The spectrometer is an Acton SP-2500i $f = 500$ mm monochromator, equipped with a liquid nitrogen cooled CCD camera. The CCD camera (PyLoN:400BR_eXcelon from Princeton Instruments) consists of 1340 x 400 pixels with a pixel size of 20 µm x 20 µm. Blazed gratings with 300, 600 and 1200 blazes are available. For polariton dispersions, the 1200 blazed grating is used for maximum spectral resolution.
On the path towards the homodyne detection setup, a 2x beam expander (GBE02-B from Thorlabs) further matches the signal beam size to the LO beam size. However, a perfect matching is not possible due to the non-perfect spatial properties of the emission. This flaw could be overcome by coupling the signal and the LO each into single-mode fibers. After such fibers, the beams possess a well-defined spatial single mode and thus their sizes match perfectly. However, in this work, free-space beams are used.
The LO wavelength is set equal to the most intense zero-momentum ground-state mode of the polariton emission. Besides, the LO has a Gaussian spatial mode and a FWHM in k space of 1.3 µm^{-1}, centered at $k = 0$. Therefore, the LO overlaps only with signal components around $k \approx 0$.

4.2.3 Calibration of the k space

When measuring a polariton dispersion with the spectrometer, another step is necessary for calibrating the k axis. Initially, the image from the spectrometer has only pixels as an x axis. To find a relation between pixels and k values, one has to perform a measurement of the k space beforehand. For this purpose, the slit of the spectrometer is removed and the grating is set to the position of 0th diffraction order. Now, the Fourier lens images the complete angle space onto the spectrometer camera as a bright circle. The diameter of this circle in pixels p_{max} equals twice the maximum angle that the microscope objective (MO) is able to capture, given by $\alpha_{\text{max}} = \arcsin(NA/n)$.

Here, $n = 1$ is the refractive index of air and $NA = 0.4$ is the numerical aperture of the MO. Thus, each pixel p in the dispersion image is related to an angle α via

$$\alpha = (p - p_0)2\alpha_{\max}/p_{\max}, \tag{4.14}$$

with p_0 being the pixel in the center of the image. Each angle is then related to an in-plane k value [KRK$^+$06],

$$k_{||} = \frac{E}{\hbar c}\sin\alpha, \tag{4.15}$$

with the energy E of the polariton dispersion at that angle.

Chapter 5

Characterization of the sample

This chapter presents a characterization of basic properties of our microcavity sample that will help us to understand the results from homodyne detection presented in later chapters. All results in this chapter are derived from dispersion measurements performed using a spectrometer. First, I determine the detuning gradient along the sample and identify a suitable detuning for later measurements. Then, for this detuning, I identify the relevant polarization directions and k-space modes that arise in the formation of the polariton condensate.

5.1 Detuning across the sample

For determining the detuning, I measured the polariton dispersion below the condensation threshold at different positions across the sample. Fig. 5.1 shows one example.

The image is intentionally saturated in order to render faint features visible. The bright parabola corresponds to the lower-polariton emission. The red line shows a fit of the parabola, from which the energy of the ground state $E_{LP}(k_{||} = 0)$ can be determined.

While the parabola of the upper polariton cannot be seen, a broad horizontal stripe of light is visible at higher energies around 1.62 eV. Assuming that this is the exciton luminescence, the exciton energy can be determined from the maximum of this energy distribution as 1.6195 eV, indicated by a white line. This relatively high energy compared to bulk GaAs is explained by the additional confinement energy in the quantum well, which can be on the order of several 100 meV and increases with decreasing quantum well thickness [MLC92].

Using the found energies of the exciton and of the lower polariton at $k_{||} = 0$, it is possible to calculate the detuning. We start by inserting the definition of the detuning $\delta = E_{\mathrm{cav}}(k_{||} = 0) - E_{\mathrm{exc}}(k_{||} = 0)$ (cf. Eq. (3.15)) into the equation for the lower-polariton energy Eq. (3.13). Then we solve this equation for the detuning,

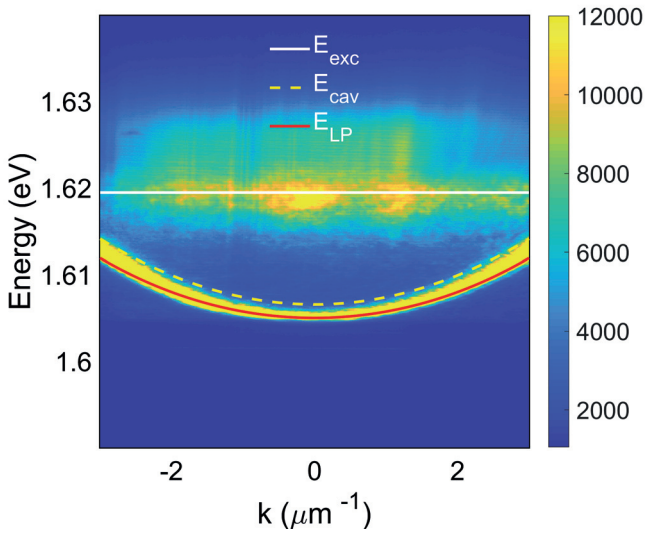

Figure 5.1: An exemplary dispersion measured below the condensation threshold. Red line: fit of the lower-polariton dispersion. Yellow dashed line: cavity dispersion. White line: exciton dispersion. The colorscale is limited to a maximum value of 12000 counts in order to render the exciton luminescence visible.

$$\delta = \frac{(2g_0)^2}{4[E_{\text{exc}}(k_{||}=0) - E_{\text{LP}}(k_{||}=0)]} - [E_{\text{exc}}(k_{||}=0) - E_{\text{LP}}(k_{||}=0)], \tag{5.1}$$

with the Rabi Splitting $2g_0$.
Using the detuning, we obtain the cavity energy $E_{\text{cav}}(k_{||}=0) = \delta + E_{\text{exc}}(k_{||}=0)$. Subsequently, the complete cavity dispersion can be calculated via Eq. (3.3) and (3.4). Here, the refractive index of GaAs in the relevant range of wavelengths is inserted as $n_c = 3.7$. [1] The calculated cavity dispersion is depicted in Fig. 5.1 as a dashed yellow line.

In this way, the detuning can be determined along the sample; see Fig. 5.2a. The sample exhibits negative detunings from about -2 meV to -18 meV. The plotted energies vs detuning in Fig. 5.2b show a similarity to the theoretical expectation presented in Fig. 3.2(a).

While it might be worthwile to investigate the effect of different detunings, for the later measurements I chose a detuning around -6 meV, corresponding to -0.6 $2g_0$. At this detuning, the condensate forms only one spot whereas for more negative detunings, the condensate tends to fragment into several spots, making it difficult to overlap with the LO for homodyne detection. A similar behavior was observed in Ref. [EGB+18], where the filamentation of the condensate at strongly negative detunings is ascribed to

[1] Different databases give values for the refractive index between 3.6 and 3.8 in the wavelength range from 768 nm to 775 nm [Pol22, Bat22].

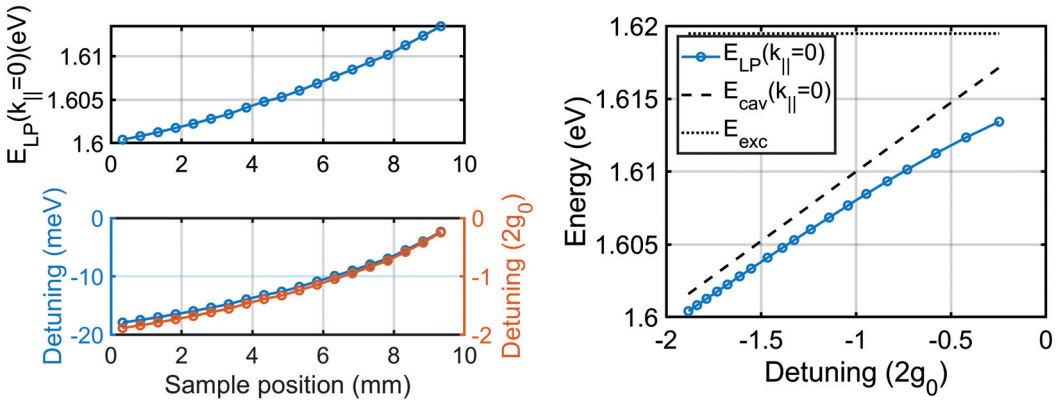

Figure 5.2: (a) Top: Measured ground-state energy of the lower polariton versus sample position relative to the edge. Bottom: Calculated detuning in meV (blue) and in units of the Rabi splitting $2g_0$ (orange) versus sample position. (b) Detuning-dependence of the lower-polariton energy at $k_{||} = 0$. On this sample, only negative detunings are available.

an effective attractive nonlinearity while the more homogeneous condensates at more positive detunings are explained by less attraction and a more efficient phonon-assisted energy relaxation suppressing high-momentum excitations. However, for more positive detunings than -6 meV on our sample, the emission intensity decreases. Thus, -6 meV detuning gives a good tradeoff with a homogeneous condensate and sufficient emission intensity. For this detuning, the condensation process is studied in the following.

5.2 Characterization of the condensation process

In order to understand the results from homodyne detection measurements in later chapters, it is important to gain information about the emission properties of the sample beforehand. Specifically, we should know which modes - with respect to polarization, k space and energy - contribute to the formation of the polariton condensate. Here, we must keep in mind that we can only measure the ground-state mode around $k = 0$ via homodyne detection; however, in future works it might be worthwhile to shape the LO to detect other modes as well. Besides, knowing the interplay between the different modes helps understanding the results observed for the ground-state mode.

5.2.1 Excitation with a large Gaussian spot without SLM

First, we study the condensation process for excitation with a large Gaussian spot without an SLM since this configuration is used for the major part of this thesis because of its temporal stability.

Initially, we determine the relevant polarization directions. Figure 5.3 shows the polarization dependence of the intensity of the ground-state mode for three different

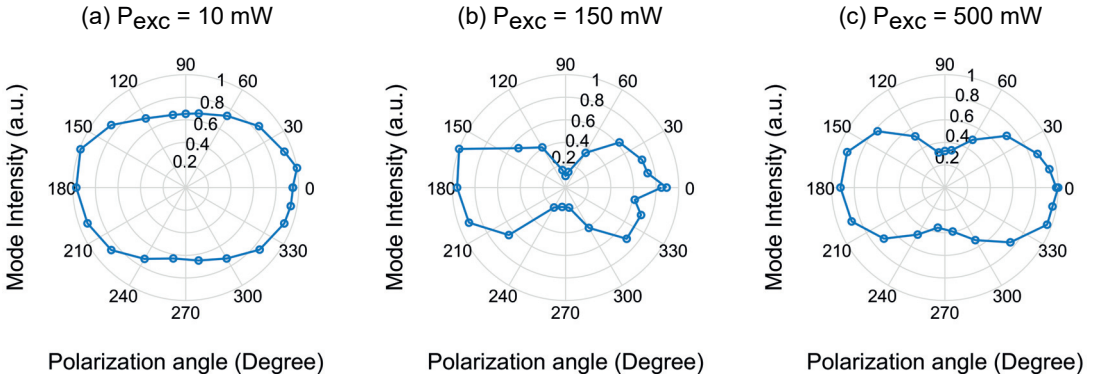

Figure 5.3: The polar plots show the ground-state intensity as a function of the linear polarization angle for three different excitation powers. The ground-state intensity is determined by integrating over a rectangular area in the dispersion with $k \in [-0.5, 0.5]$ µm^{-1}.

excitation powers, i.e. below the condensation threshold, intermediate and high. For this measurement, the polarization of the emission is filtered with a half-wave plate and a Glan-Thompson prism on the path to the spectrometer. The Glan-Thompson prism transmits only a fixed polarization direction, onto which the incoming light is rotated by the half-wave plate, in order to avoid any impact of the polarization-dependent efficiency of the spectrometer grating. To obtain the ground-state intensity from the measured dispersions, the intensity is integrated over a rectangular part of the dispersion with $k \in [-0.5, 0.5]$ µm^{-1} because this range of k values is also selected later by the pinhole and the LO for homodyne detection. The corresponding energy range of the integrated rectangle is varied with excitation power to account for the blue- or red shift of the emission.

According to Fig. 5.3, the dominant polarization direction is (0°,180°). Already below threshold, there is a degree of linear polarization between 0° and 90° given by $DLP = \frac{I_0 - I_{90}}{I_0 + I_{90}} = 0.18$. At the intermediate power, the emission is temporally instable, producing a more chaotic image. Supposedly this is caused by mode competition that occurs in this power range as we will see in the following. Finally, for the highest excitation power, the emission is clearly linearly polarized with a polarization degree $DLP = \frac{I_0 - I_{90}}{I_0 + I_{90}} = 0.5$.

Such a linear polarization of the polariton emission has also been observed in the literature. In particular, Refs. [KRK$^+$06, KMA$^+$06, KAD$^+$07] found that the polarization is aligned along one of the crystallographic axes of the sample, independently of the polarization of the excitation. Ref. [KMA$^+$06] attributes this pinning of the polarization along the crystal axis to a small birefringence in the cavity, probably being caused by weak uniaxial strain. Such a birefringence causes a splitting of the cavity energy for the two polarization directions. According to Ref. [KAD$^+$07], the system selects the polarization with lower energy in order to minimize the free energy in the presence of

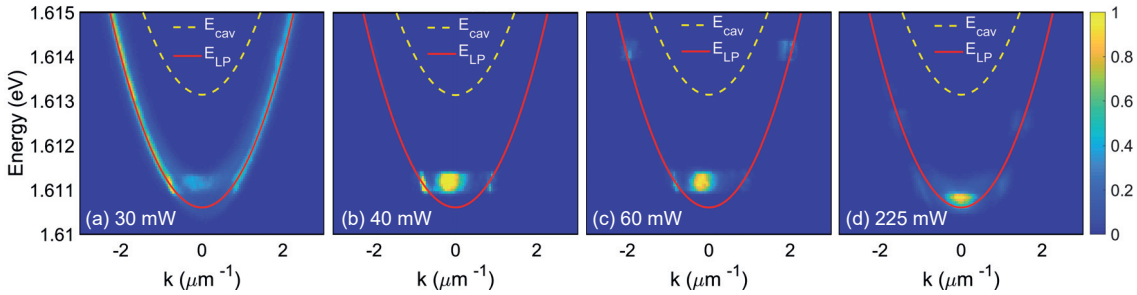

Figure 5.4: Dispersion curves measured at different excitation powers for excitation with a large Gaussian spot. In each panel, the emission is normalized to one and plotted on a linear color scale. The red line shows the LP dispersion obtained from a fit below threshold. The yellow dashed line indicates the calculated cavity dispersion. In plot (a) at 30 mW, in (b) at 40 mW and in (c) at 60 mW, the emission around $k = 0$ is blueshifted because of polariton-polariton interaction. In (b), emission at $k = \pm 0.8$ µm^{-1} is visible. In (c), there is also faint emission at $k = \pm 2$ µm^{-1}. In panel (d), 225 mW, the emissions at higher k are mostly suppressed compared to the dominant emission at $k = 0$, which is redshifted because of heating.

polariton-polariton interactions.
Consequently, the two basic polarization directions are 0°, which presumably corresponds to the crystal axis, and 90°, being orthogonal to this axis. Therefore, the following more detailed power dependence is only measured for these two polarizations.

In order to observe the buildup of a polariton condensate, I recorded dispersions for varying excitation power. The goal is to obtain an input-output relation of emission intensity versus excitation power, also called I-O curve. In this I-O curve, a nonlinear increase indicates the formation of a polariton condensate. However, the I-O curve should be considered with respect to a well-defined emitting mode. Preferably, we want the condensate to form in the ground state around $k = 0$. To check this, the dispersions reveal which modes are contributing at which power.

Figure 5.4 shows dispersions at four different powers for 0° polarization. At 30 mW, emission starts to form around $k = 0$ and $E = 1.611$ eV, becoming more bright at 40 mW. This is the ground-state mode; notably, it is blueshifted compared to the polariton dispersion at very low powers, indicated by the red parabola. This blueshift is caused by repulsive polariton-polariton interaction [DHY10].
Remarkably, at 40 mW, bright emission appears at $k = \pm 0.8$ µm^{-1}. This emission originates from polaritons being repelled by the excitonic reservoir and scattered to higher-k states and probably also to different spatial positions. Particularly for negative detuning, polaritons can accumulate at high-k states under continuous-wave excitation because energy relaxation is less efficient [EGB+18]. Furthermore, between 60 and 100 mW, there is also a faint emission around $k = \pm 2$ µm^{-1} but much weaker than the other modes.

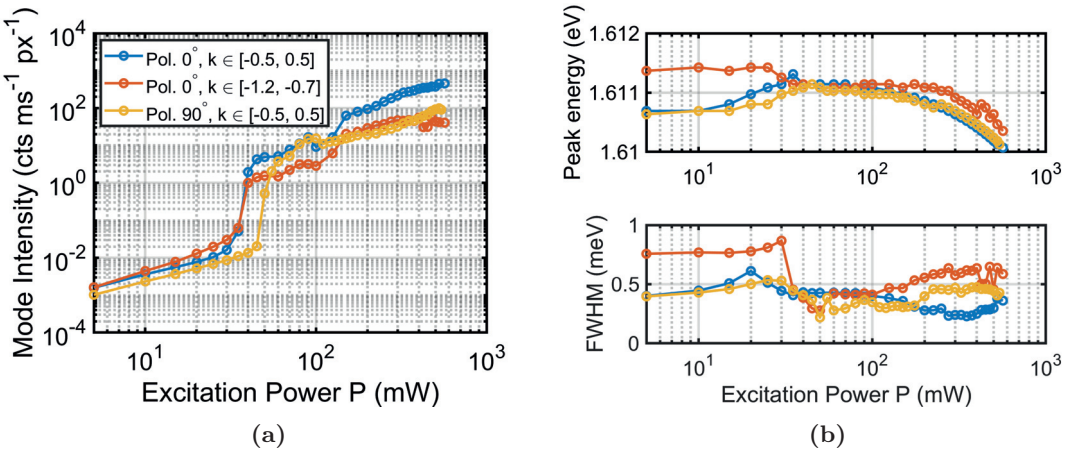

Figure 5.5: (a) Integrated intensity of the selected mode rectangle versus excitation power for excitation with a large Gaussian spot. For comparability, the intensity has been divided by the acquisition time and the size of the rectangle in pixels. Blue: Polarization 0°, ground-state mode $k \in [-0.5, 0.5]$ µm^{-1}. Red: Polarization 0°, $k \in [-1.2, 0.7]$ µm^{-1}. Yellow: Polarization 90°, ground-state mode $k \in [-0.5, 0.5]$ µm^{-1}. (b) Top: Peak energy for the selected k ranges. Bottom: FWHM of the peak for the selected k ranges.

These higher-momentum modes almost vanish for 225 mW. Then, most emission comes from the ground state, which is now redshifted due to heating of the sample.
Here, we also note that the energy of the condensate lies below the cavity energy (indicated in yellow) for all powers. Therefore, we conclude that the strong-coupling regime is preserved.
Thus, the most important modes for constructing an I-O curve are the one around $k = 0$ and the one at $k = \pm 0.8$ µm^{-1}.

The I-O curves of the different modes are depicted in Fig. 5.5a. For each data point, the emission intensity is integrated in a rectangle around the selected mode and divided by the acquisition time and the rectangle size for comparability. At 90° polarization, only the ground-state mode has a significant contribution and is evaluated here. Figure 5.5b shows in the upper panel the peak energy for the selected k range and in the lower panel the FWHM of the peak.

The I-O curve for the ground-state mode at 0° polarization (blue) exhibits a nonlinear increase of intensity at 30 mW. This nonlinearity is usually ascribed to the onset of condensation and the corresponding power is called threshold power. Around this power also the maximum blueshift occurs and the FWHM undergoes a change.
However, the behavior is more complex since also the intensity of $k \in [-1.2, 0.7]$ µm^{-1} (red) nonlinearly increases at this power, and the ground-state intensity at 90° polarization (yellow) nonlinearly increases at slightly higher powers as well. These modes also possess a low FWHM in the range of 30 - 200 mW excitation power. Note that a narrowing of the linewidth is one of the hallmarks of condensation [DP12]. Thus, the three different modes compete for the formation of a condensate in this power range.

For powers above 150 mW, the intensity of the high-k mode stagnates and its FWHM increases, leaving the ground state predominating. But still the two polarizations compete in the ground state.
Such a mode competition and bistability between the two cross-linearly polarized components has also been predicted in Ref. [Sig20] and observed in Ref. [BZS+22].
Only above 200 mW, the FWHM of the ground state at 0° polarization decreases additionally while the FWHM at 90° increases again. Thus, for $P > 200\,\mathrm{mW}$, the 0° polarization "wins" the competition and contributes solely to the polariton condensate. Eventually, for $P > 400\,\mathrm{mW}$, the intensity of the ground state at 0° polarization stagnates and its FWHM increases slightly. Here we also observe a significant redshift of the peak energy. Both can be attributed to heating of the sample.
In conclusion, the condensation process is complex and governed by mode competition between 30 and 200 mW. Only for higher powers, the condensate in the 0° polarized ground state predominates. These observations are compared with the results from homodyne detection in Chapters 7 and 8. Also, note that the blue- and redshift of the emission requires us to adapt the LO energy accordingly. Therefore, I chose the spectral width of the LO broad enough to cover the entire energy range of the ground state; see Chapter 7.

5.2.2 Ring-shaped excitation with SLM

In this subsection, I present the characterization for the ring-shaped excitation with an SLM. The results are similar to the ones above up to a few differences. One difference is that the powers needed for condensation are lower since the excitation area is smaller and the trap enhances the accumulation of polaritons in the ground state.
The dominant direction of linear polarization has been found to be 10°, and the one orthogonal to it 100° (corresponding to 5° and 50° settings of the half-wave plate). These are very similar to the 0° and 90° directions (0° and 45° settings of the half-wave plate) found above. The deviation between the directions might stem from an uncertainty when setting the half-wave plate, or from a variation of the sample birefringence at different sample spots. Another reason might be an imperfect excitation ring. If the ring is slightly elliptic, the major and minor axis of the ellipse are the preferred axes of polarization [GST+21].

In the dispersions (Figure 5.6), there are mainly two modes visible: the ground-state mode around $k = 0$ and energy $E \in [1.611, 1.6112]\,\mathrm{eV}$ and another mode at slightly higher energy $E \in [1.6113, 1.6116]\,\mathrm{eV}$ and with broader k range $k \in [-1, 1]\,\mu\mathrm{m}^{-1}$, which appears only for 100° polarization. The I-O curves of these modes are plotted for the two principal linear polarizations in Fig. 5.7(a).

The peak position and FWHM are shown in Fig. 5.7(b). The DLP of the two modes is shown in Fig. 5.7(c).

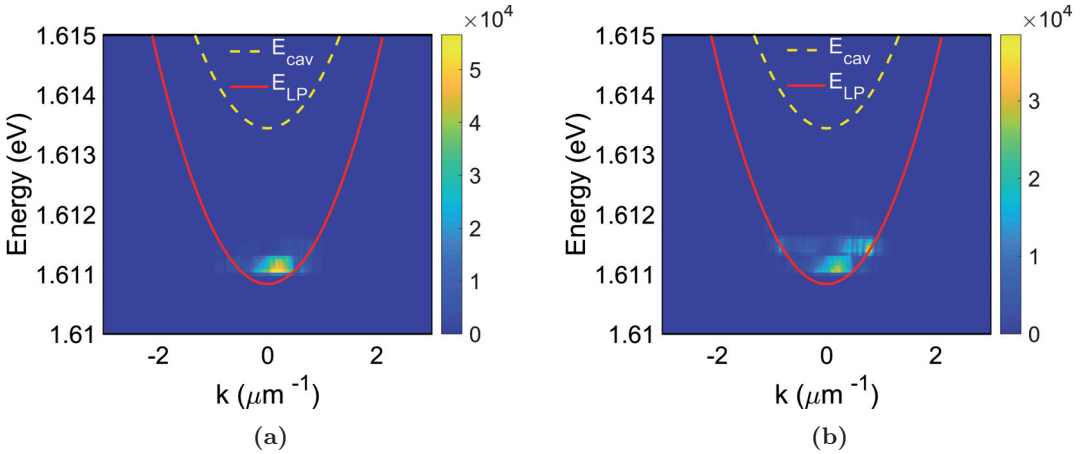

Figure 5.6: Dispersions for ring-shaped excitation at 20.4 mW excitation power. (a) 10° polarization. (b) 100° polarization. The red line shows the LP dispersion obtained from fitting the dispersion at a power below threshold. The yellow dashed line indicates the calculated cavity dispersion.

All I-O curves exhibit a threshold at 7 mW, indicating the onset of condensation. The ground-state mode with polarization 10° (blue) is the most intense one for all powers and also has the lowest FWHM, being ca 0.25 meV above threshold. This stands in contrast to Gaussian excitation, where such a low FWHM of the 0° polarized ground state is reached only above 200 mW. Thus, the condensation into this mode is more stable for ring-shaped excitation, probably because the reservoir has less influence.
The 100° polarized emission in the ground-state (red) is significantly less intense. The degree of polarization $DLP = \frac{I_{10}-I_{100}}{I_{10}+I_{100}}$ of the ground state is also shown in Fig. 5.7(c). Below threshold, the DLP has the opposite sign — apparently pinned orthogonal to the crystal axis — whereas above threshold, it has a high positive value.
Interestingly, for the higher mode, above threshold, the 100° polarization predominates and the DLP is negative. Thus, the ground state and the higher-energy mode are cross-polarized.
This is different from Gaussian excitation, where both polarizations compete apparently in the same energy mode. Maybe the size of the birefringence-induced energy splitting varies at different sample spots. Another reason might be an energy splitting that occurs for a slightly elliptical excitation spot [GST+21].
To conclude, for ring-shaped excitation, the most dominant mode is the ground state at 10° polarization. Its energy exhibits much less blue- or redshift than the mode energy observed for Gaussian excitation, probably because there is less interaction with the reservoir and less heating due to lower powers. Thus, a less broad LO spectrum is needed to cover it. This mode is measured with homodyne detection in Chapter 6.

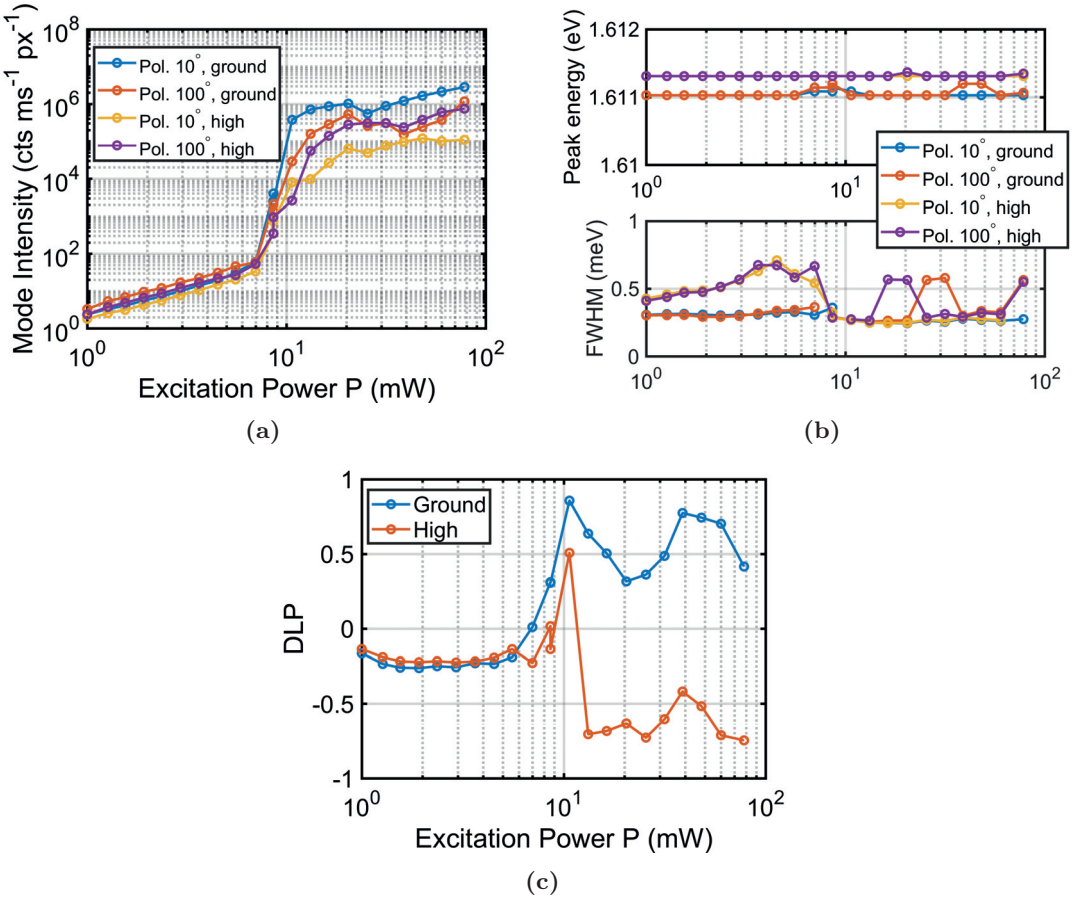

Figure 5.7: (a) Integrated intensity of the selected mode rectangle versus excitation power for ring-shaped excitation. For comparability, the intensity has been divided by the acquisition time and the size of the rectangle in pixels. Blue: Polarization 10°, ground-state mode $k \in [-0.5, 0.5]$ µm^{-1}, $E \in [1.611, 1.6112]$ eV. Red: Polarization 100°, ground-state mode. Yellow: Polarization 10°, higher mode $k \in [-1, 1]$ µm^{-1}, $E \in [1.6113, 1.6116]$ eV. Purple: Polarization 100°, higher mode $k \in [-1, 1]$ µm^{-1}, $E \in [1.6113, 1.6116]$ eV. (b) Peak energy and FWHM. Note that the FWHM values for 100° polarization are erratically high at some powers because the two peaks of the ground state and the higher-energy state lie too close to each other for a proper estimation of their respective FWHMs. (c) Degree of Linear Polarization (DLP) of the ground-state mode (blue) and of the higher mode (red).

Chapter 6

One-channel homodyne detection: Distinguishing noise sources in photon correlations

The second-order photon correlation function $g^{(2)}$ serves as a criterion to distinguish different states of light (although not completely unambiguous), cf. Section 2.4 and Section 3.5. Unfortunately, many detection methods for $g^{(2)}$ that rely on photon counting, e.g. the HBT setup or the streak camera, require long integration times and can be influenced by external noise sources, distorting the measured value of $g^{(2)}$. This flaw can be overcome by a detection method with sufficient time resolution and short integration time.
In this chapter, I present time-resolved measurements of $g^{(2)}(\tau = 0,t)$ of the polariton emission and analyze these measurements with respect to the frequency with which the $g^{(2)}$ values are sampled. My results show that via differentiating $g^{(2)}$ by frequency, external noise can be separated from the intrinsic $g^{(2)}$ value of the light field, as long as the typical time scales of the external noise and of the internal photon-number fluctuations differ sufficiently. Usually, this condition is fulfilled since mechanical noise occurs in the Hz to kHz range while intrinsic photon-number fluctuations happen on the time scale of the coherence time of the light field, which is typically in the range of pico- to nanoseconds in semiconductor physics. This chapter is mostly based on Ref. [LA20].

6.1 Setup

For the measurements presented in this chapter, I used the basic one-channel homodyne detection setup that is explained in Chapter 4. I excited the sample with a ring-shaped beam created by a Spatial Light Modulator (SLM). The SLM causes a temporal modulation of the excitation intensity and leads to a modulated sample emission. This "bug" is actually a "feature" for our purpose, providing a suitable testing ground for

the frequency-resolved $g^{(2)}$ analysis.
The LO energy was set to 1.611 eV, matching the ground-state condensate energy shown in Fig. 5.6. The FWHM of the LO spectrum was 0.0018 eV, corresponding to a pulse length of about 1 ps.

6.2 Calculation of $g^{(2)}$ from quadratures

A homodyne measurement provides us with a set of subsequent quadrature values q_i. Each value is measured with a time resolution $\Delta\tau$ given by the pulse width of the LO, and the temporal distance between consecutive values corresponds to the time T between subsequent LO pulses, being inversely proportional to the LO pulse rate $1/T$; cf. Fig. 4.2.
Now, for each subset of x consecutive quadrature values q_i,q_{i+1},...q_{i+x-1}, corresponding to a time span $t_{av} = xT$, we can calculate the average photon number and the average $g^{(2)}$ via the second and forth statistical moment of the quadratures [RC13]. We derive the second moment from the definition Eq. (2.32) of the phase-dependent quadrature $\hat{q}_\theta$,

$$\langle \hat{q}_\theta^2 \rangle_{t_{av}} = A^2 \langle \hat{a}^\dagger \hat{a} + \hat{a}\hat{a}^\dagger + \hat{a}^\dagger \hat{a}^\dagger \mathrm{e}^{\mathrm{i}2\theta} + \hat{a}\hat{a}\mathrm{e}^{-\mathrm{i}2\theta} \rangle_{t_{av}}. \tag{6.1}$$

Here, the two terms containing the phase vanish when averaging over all possible phases between LO and signal. This requires the phase of the signal to be sufficiently randomized so all possible phases are realized equivalently in the time span t_{av}, which is the case if the coherence time of the light source is lower than t_{av}. When this condition is fulfilled, the equation can be simplified with help of the bosonic commutator relation, delivering the mean photon number

$$\boxed{n_{av} = \langle \hat{a}^\dagger \hat{a} \rangle_{t_{av}} = \frac{\langle \hat{q}_\theta^2 \rangle_{t_{av}}}{2A^2} - \frac{1}{2}.} \tag{6.2}$$

Similarly, when omitting all phase-dependent terms, the fourth moment results in

$$\langle \hat{q}_\theta^4 \rangle_{t_{av}} = \frac{1}{A^4} \langle \hat{a}^\dagger \hat{a}\hat{a}^\dagger \hat{a} + \hat{a}^\dagger \hat{a}\hat{a}\hat{a}^\dagger + \hat{a}\hat{a}^\dagger \hat{a}^\dagger \hat{a} + \hat{a}\hat{a}^\dagger \hat{a}\hat{a}^\dagger + \hat{a}^\dagger \hat{a}^\dagger \hat{a}\hat{a} + \hat{a}\hat{a}\hat{a}^\dagger \hat{a}^\dagger \rangle_{t_{av}} \tag{6.3}$$

$$= \frac{1}{A^4} \langle 6\hat{a}^\dagger \hat{a}^\dagger \hat{a}\hat{a} + 12\hat{a}^\dagger \hat{a} + 3 \rangle_{t_{av}}. \tag{6.4}$$

From this follows

$$\boxed{\langle \hat{a}^\dagger \hat{a}^\dagger \hat{a}\hat{a} \rangle_{t_{av}} = \frac{A^4}{6} \langle \hat{q}_\theta^4 \rangle_{t_{av}} - 2\langle \hat{a}^\dagger \hat{a} \rangle_{t_{av}} - \frac{1}{2}.} \tag{6.5}$$

Then, the results of Eq. (6.2) and (6.5) can be inserted into the definition of the equal-time photon correlation $g^{(2)}(\tau = 0,t)$ (2.15)

$$\boxed{g^{(2)}(\tau = 0,t) = \frac{\langle \hat{a}^\dagger \hat{a}^\dagger \hat{a}\hat{a}\rangle_{t_{av}}}{\langle \hat{a}^\dagger \hat{a}\rangle^2_{t_{av}}}.} \tag{6.6}$$

Thus, for each time span $t_{av} = xT$, one value of the mean photon number and of $g^{(2)}(\tau = 0,t)$ can be calculated. This corresponds to a sampling frequency $f_{av} = 1/t_{av}$. For example, when $T = 13.3\,\text{ns}$ and $x = 1000$, the averaging time is $t_{av} = 13.3\,\mu\text{s}$, corresponding to a frequency $f_{av} = 75.4\,\text{kHz}$. By choosing different subset sizes x for the average, different frequencies f_{av} can be investigated.
Note that the time resolution $\Delta\tau$ which determines the range of delays for which two photons are considered to arrive simultaneously ($\tau = 0$) is given by the LO pulse length.

On the other hand, the slow intensity noise over the full duration of the measurement may be quantified via the conventional intensity correlation function

$$g^{(2)}_{slow}(0) = \frac{\langle n^2_{av}\rangle_{full}}{\langle n_{av}\rangle^2_{full}}. \tag{6.7}$$

.

For clarity, we will refer to the photon correlation function given by Eq. (6.6) as $g^{(2)}_{fast}(0,t)$.

Now, it is possible to distinguish different noise components via their frequency. When calculating $g^{(2)}_{fast}(0,t)$ with an averaging time t_{av}, one includes all fluctuations that happen within this time span, contributing to a higher value. On the other hand, fluctuations that occur on a longer time scale do not play a role in the time window t_{av} and do not influence the value of $g^{(2)}_{fast}(0)$. Considering the frequency space, let us assume a fluctuation having a typical frequency f_{noise}. Then, for $f_{av} < f_{noise}$, this fluctuation enhances the value of $g^{(2)}_{fast}(0)$ whereas for $f_{av} > f_{noise}$, the fluctuation does not influence $g^{(2)}_{fast}(0)$. Thus, by choosing a sufficiently high averaging frequency f_{av}, it is possible to remove the influence of slower noise sources. In particular, slow mechanical noise with a typical frequency range of Hz to kHz can be separated from the intrinsic photon-number fluctuations of the light source.
By contrast, $g^{(2)}_{slow}(0)$ experiences the opposite effect: for $f_{av} < f_{noise}$, the fluctuations in n_{av} are smoothed away and do not enter $g^{(2)}_{slow}(0)$ whereas for $f_{av} > f_{noise}$, the fluctuations in n_{av} are resolved and lead to a higher value of $g^{(2)}_{slow}(0)$. Thus, $g^{(2)}_{slow}(0)$ contains every kind of noise that occurs at a frequency smaller than f_{av} while $g^{(2)}_{fast}(0)$ indicates noise that occurs at frequencies higher than f_{av}, including the intrinsic photon-number noise of the light source.
Note that for typical detection methods that rely on photon counting, t_{av} corresponds to the integration time that is needed to obtain a single value of $g^{(2)}(0)$ and can amount to minutes, see e.g. Ref. [KvHR$^+$20], making different kinds of noise indistinguishable.

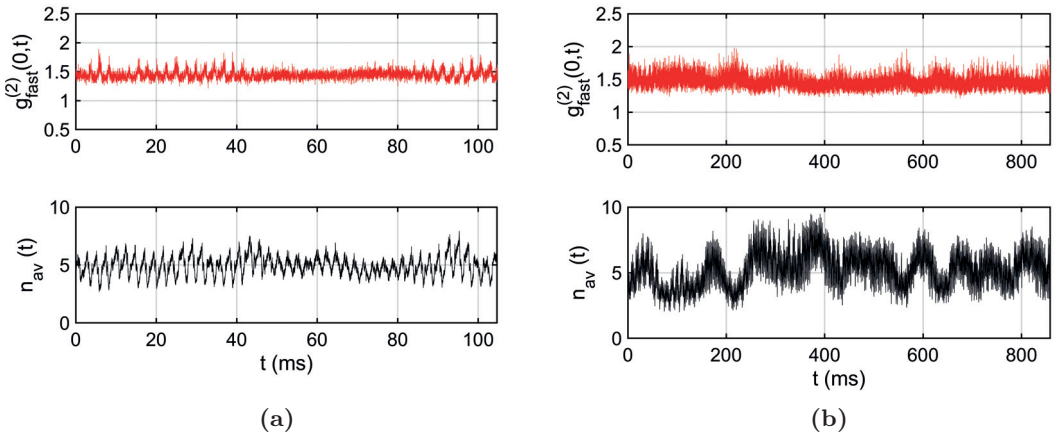

Figure 6.1: (a) Time-resolved $g^{(2)}_{fast}(0,t)$ and n_{av} for an excitation power $P_{\mathrm{exc}} = 85\,\mathrm{mW}$. The averaging frequency is $f_{av} = 75.4\,\mathrm{kHz}$. (b) The longer time-trace shows a measurement under the same conditions as in (a) but with mechanical noise applied to the setup.

In contrast, for our fast homodyne detection, the maximum frequency is limited by the repetition rate of the laser $1/T = 75.4\,\mathrm{MHz}$, which is significantly faster than most mechanical noise sources. After data acquisition, f_{av} can be chosen freely when analyzing the data, enabling us to investigate noise on different time scales.
In the following, the results for the polariton emission are discussed.

6.3 Results

For the frequency analysis, we pick two different excitation powers: one far above the threshold — which was determined to be 7 mW in Section 5.2.2 — at 85 mW, where the emission is rather stable, and one closer to the threshold at 30 mW, where the system undergoes a non-linear change and reacts strongly to external noise.
For the higher power, the temporal dependence of $g^{(2)}_{fast}(0,t)$ and $n_{av}(t)$ is shown in Fig. 6.1 to give an impression of the fluctuations. Fig. 6.1(a) displays a shorter measurement without additional noise and Fig. 6.1(b) a longer measurement with additional slow mechanical noise that was added by tapping on the optical table. An averaging frequency $f_{av} = 75.4\,\mathrm{kHz}$ was chosen to resolve most fluctuations. The time-trace reveals several modulations at different time scales.

The frequencies of these modulations are quantified by a Fourier transform of n_{av}. A typical Fourier transform in the presence of external noise is shown in Fig. 6.2. Below 50 Hz, a continuum of noise is present, probably being caused by mechanical vibrations of the setup. Furthermore, discrete peaks appear at multiples of 60 Hz, which have a significant influence up to about 1 kHz. These stem from the SLM, which is a digitally-addressed spatial light modulator with an addressing frequency of 120 Hz

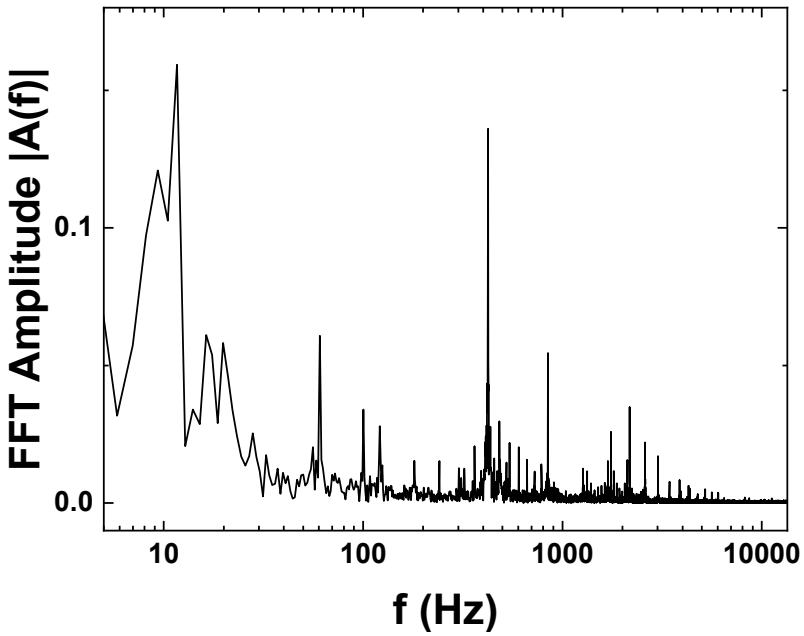

Figure 6.2: Fourier transform of $n_{av}(t)$ where $f_{av} = 75.4\,\mathrm{kHz}$ was used. The noise spectrum exhibits a continuum of mechanical noise below 50 Hz and discrete lines at multiples of 60 Hz that arise due to the pulse-width modulation of the SLM. Image from [LA20].

for pulse-width modulation. In order to generate intermediate greyscale values on the display pixels to create a refractive pattern for the excitation beam, only two voltage states are actually applied to the modulator. The dwell time in these voltage states is varied at the addressing frequency. This modulation scheme causes noise at half the addressing frequency and harmonics of that value [FSLQ$^+$11].

Now we know the relevant frequencies where external noise is expected to become prominent and can compare these to the dependence of $g^{(2)}_{fast}(0)$ on f_{av}.

To this purpose, we calculate the mean value of $g^{(2)}_{fast}(0,t)$ for each value of f_{av} for the full measurement. Thereby, $g^{(2)}_{fast}(0,t)$ is weighted with the squared photon number $n_{av}(t)^2$ via

$$g^{(2)}_{fast}(0) = \frac{\sum_t n_{av}(t)^2\, g^{(2)}_{fast}(0,t)}{\sum_t n_{av}(t)^2}. \tag{6.8}$$

This correction is used to neutralize the effect of exceptionally small photon numbers leading to an exceptionally high $g^{(2)}_{fast}(0,t)$ since $n_{av}(t)^2$ contributes in the denominator of Eq. (6.6).

The result is shown in Fig. 6.3 for $P_{\mathrm{exc}} = 85\,\mathrm{mW}$. Full symbols and open symbols denote $g^{(2)}_{fast}(0)$ and $g^{(2)}_{slow}(0)$, respectively. Black data points represent the standard measurement while red data points depict the measurement where mechanical noise

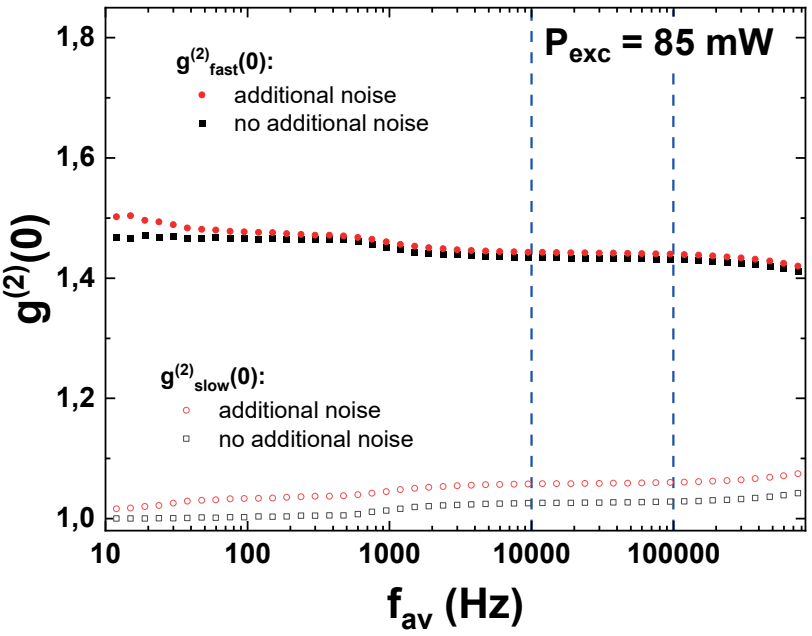

Figure 6.3: Frequency-dependence of $g^{(2)}(0)$ for $P_{\mathrm{exc}} = 85\,\mathrm{mW}$. Full symbols: mean value of $g^{(2)}_{fast}(0)$ versus the averaging frequency f_{av}. Open symbols: $g^{(2)}_{slow}(0)$. Black: standard measurement. Red: measurement with additional mechanical noise. Dashed lines indicate the frequency region where external noise does not influence $g^{(2)}_{fast}(0)$. Adapted from [LA20].

was added.

In both cases, the values of $g^{(2)}_{fast}(0)$ lie in a rather small range between 1.42 and 1.5, which implies that the polariton condensate is rather stable against environmental noise for this high excitation power. Nevertheless, we observe three different frequency regions with slightly different $g^{(2)}$ values.

First, for f_{av} below 1 kHz, $g^{(2)}_{fast}(0)$ has a plateau around 1.47. For $f_{av} > 1\,\mathrm{kHz}$, $g^{(2)}_{fast}(0)$ decreases and reaches another plateau around 1.43. Finally, for $f_{av} > 100\,\mathrm{kHz}$, $g^{(2)}_{fast}(0)$ reduces further. On the other hand, $g^{(2)}_{slow}(0)$ experiences the opposite trend: It is lower in the first region, increases in the second region and again in the third region.

Regarding the first region, in the low frequency range below 50 Hz, $g^{(2)}_{fast}(0)$ is significantly higher in the presence of external noise (red) than without (black). But for higher frequencies, both are very similar. Apparently, this difference at very low frequency stems from the continuum of mechanical noise apparent in the Fourier transform below 50 Hz. This supports our assumption that mechanical noise only has an impact at low frequencies and can be removed by sampling at higher frequencies.

But even if only standard environmental noise is present, $g^{(2)}_{fast}(0)$ is higher in the region below 1 kHz than above 1 kHz, probably because of the modulation by the SLM that is significant in this range.

In the second region, where $f_{av} > 1\,\mathrm{kHz}$, the modulation by the SLM does not impact

$g^{(2)}_{fast}(0)$ anymore and therefore the value is lower. On the other hand, $g^{(2)}_{slow}(0)$ increases. This demonstrates that as soon as f_{av} becomes comparable to the frequency of a certain noise component, this noise is transferred from $g^{(2)}_{fast}(0)$ to $g^{(2)}_{slow}(0)$. In the frequency range between 10 kHz and 100 kHz, $g^{(2)}_{fast}(0)$ is almost constant and very similar both with and without external mechanical noise whereas $g^{(2)}_{slow}(0)$ differs considerably with and without external noise. Thus, in this range, $g^{(2)}_{fast}(0)$ is probably unperturbed by external noise and represents the intrinsic photon correlation of the polariton emission while $g^{(2)}_{slow}(0)$ indicates external perturbations.
Finally, in the third region beyond 100 kHz, the value of $g^{(2)}_{fast}(0)$ reduces further. This effect is an artifact of the averaging procedure. As explained above, in order to calculate $g^{(2)}(0)$ correctly from the quadrature values, all relative phases between signal and LO need to be included equally. In our case, there is no fixed phase between LO and signal and the time between two subsequent LO pulses is significantly longer than the coherence time of the polariton condensate. Thus, each quadrature value is measured at a random phase between signal and LO. However, at high f_{av}, the number of quadrature measurements x within a single averaging time window t_{av} may become too small to include all relative phases equally; e.g. at $f_{av} = 100$ kHz, x amounts to 750. Thus, the results are reliable only for f_{av} up to 100 kHz.
We conclude that in the frequency range between 10 kHz and 100 kHz, $g^{(2)}_{fast}(0)$ represents the intrinsic photon-number fluctuations of the light field emitted from the sample.

Now let us examine the results for a power closer to the threshold, 30 mW, which are shown in Fig. 6.4. At this excitation power, the condensate is less stable and more susceptible to perturbations.

Again, full symbols denote $g^{(2)}_{fast}(0)$ and open symbols $g^{(2)}_{slow}(0)$. Black symbols indicate a standard measurement while red symbols show a measurement with added mechanical noise. In general, the values of $g^{(2)}$ are higher for 30 mW than for 85 mW but the three different frequency regions observed before can be identified as well.
In the low frequency range, where most detection methods work, the $g^{(2)}$ values are exceptionally high. For the standard measurement, $g^{(2)}_{fast}(0)$ is 2 below 1 kHz — which would correspond to the value for thermal light — and even 2.1 at very low frequencies below 50 Hz. With external noise, the values are drastically higher, and reach 2.3 below 1 kHz and 2.8 below 50 Hz. These values even exceed the value for thermal light and are not physically realistic anymore. Thus, in this low frequency range, the external noise completely overlays the true photon statistics of the emitted light field.
On the contrary, in the relevant frequency range between 10 and 100 kHz that we identified previously, $g^{(2)}_{fast}(0)$ lies between 1.83 and 1.88 without and with added external noise, respectively. Again, the additional mechanical noise strongly influences $g^{(2)}_{slow}(0)$. However, even in this frequency range, $g^{(2)}_{fast}(0)$ differs slightly with and without external noise. Thus, the external noise is capable of altering $g^{(2)}$ even in the optimum

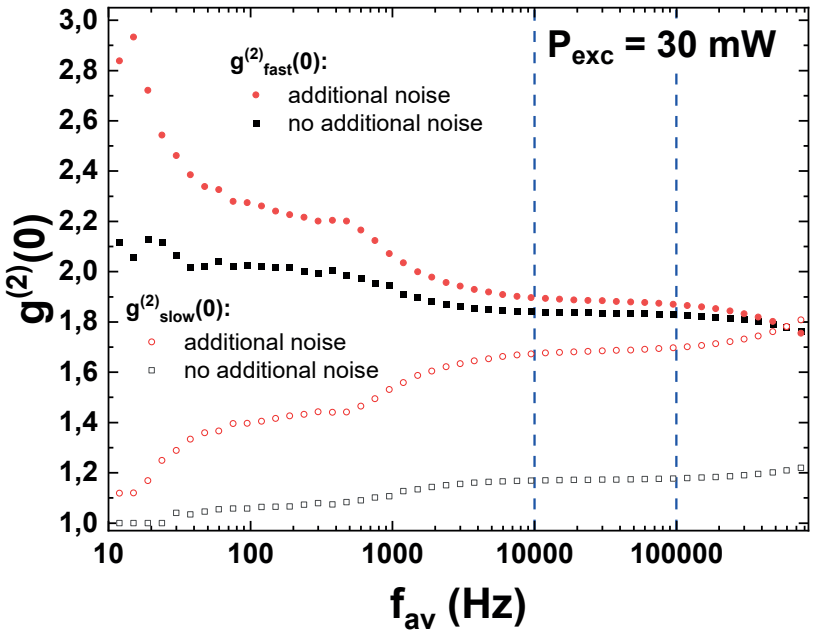

Figure 6.4: Frequency-dependence of $g^{(2)}(0)$ for $P_{\mathrm{exc}} = 30\,\mathrm{mW}$. Full symbols: mean value of $g^{(2)}_{fast}(0)$ versus the averaging frequency f_{av}. Open symbols: $g^{(2)}_{slow}(0)$. Black: standard measurement. Red: measurement with additional mechanical noise. Adapted from [LA20].

frequency range.

In order to explain this effect, let us discuss different ways how external noise may affect the measured photon correlation. On the one hand, mechanical noise can impact the detection by perturbing the alignment of optics and the overlap of the light field with the detector or the LO. In this case, the noise slowly modulates the measured intensity but does not change the intrinsic relative photon-number fluctuations of the emission. On the other hand, mechanical noise may also influence the incoupling of the excitation beam into the microcavity, acting as a slow modulation of the excitation power. In particular close to the condensation threshold, a change in excitation power also non-linearly changes the state of the polaritons between condensed and uncondensed, which directly impacts the photon statistics of the emitted light. A similar effect has been observed for systems with a nonlinear optical response, which emit light with enhanced photon correlation when excited by a noisy source [AB15, KSA$^+$15]. This impact on the $g^{(2)}$ value of the emission cannot be eliminated by using different values of f_{av}.

Still, $g^{(2)}_{fast}(0)$ shows a more realistic value in the frequency range between 10 and 100 kHz than for low f_{av}. Thus, this method is more reliable than slower detection methods.

6.4 Conclusion

To conclude, in this chapter, I presented time-resolved measurements of the photon number and the second-order correlation function $g^{(2)}(0,t)$ of a polariton microcavity that is excited non-resonantly by cw coherent light shaped via an SLM. The second-order correlation function is perturbed by mechanical noise in the setup and by a modulation of the excitation intensity caused by the SLM. My results indicate that these slower external influences can be separated from the faster intrinsic photon-number fluctuations by using a sufficiently high averaging frequency f_{av} for obtaining the $g^{(2)}(0,t)$ values. Specifically, in the frequency range between 10 and 100 kHz, the slower external noise is almost completely suppressed.
Thus, time-resolved homodyne detection is a suitable tool for investigating the photon statistics of a light source where external noise might be a problem. This is especially an issue when noise itself is an important figure of merit, e.g. for the detection of squeezed light [BBA$^+$14, AAF$^+$17].

However, $g^{(2)}(0)$ alone does not deliver a complete description of the state of light. To gain a more complete description, I employ two-channel homodyne detection in order to reconstruct phase-space functions of the polariton emission in the next chapter.

Chapter 7

Two-channel homodyne detection: Quantifying quantum coherence from Husimi functions

One of the phase-space distributions introduced in Section 2.7 is the Husimi Q function. This distribution can be obtained from two-channel homodyne measurements. In this chapter, I explain the two-channel homodyne setup[1], introduce the theoretically expected Husimi function for the polariton emission, and show the measured results. From the Husimi function, I determine the emission's quantum coherence. Furthermore, I compare the results to numerical simulations performed by the group of Stefan Schumacher at Paderborn University. The theoretical background of quantum information science was provided by Jan Sperling at Paderborn University. This chapter is mostly based on Ref. [LPR$^+$21].

7.1 Two-channel setup

The pump laser exciting the sample has the wide Gaussian shape introduced before. For using two homodyne detection channels simultaneously, the basic setup described in Section 4.1.2 is slightly modified, as shown in Fig. 7.1. constituting a so-called eight-port interferometer [Sch01, p. 361].

The signal beam and the LO beam are each split into two partial beams which enter the two homodyne channels where the quadratures X_1 and X_2 are measured. Both signal beams should have the same mean photon number to obtain a symmetric Husimi function. Furthermore, in order to obtain correct Husimi functions, it is crucial that the signal in both channels is measured at exactly the same time. This requires that

[1] In the literature, this is sometimes also called heterodyne setup; see e.g. Ref. [TMJ$^+$17]. However, this may lead to confusion, since heterodyne detection also describes a technique where the local oscillator has a slightly different frequency than the signal in order to detect their beating at the much lower difference frequency [DeL68].

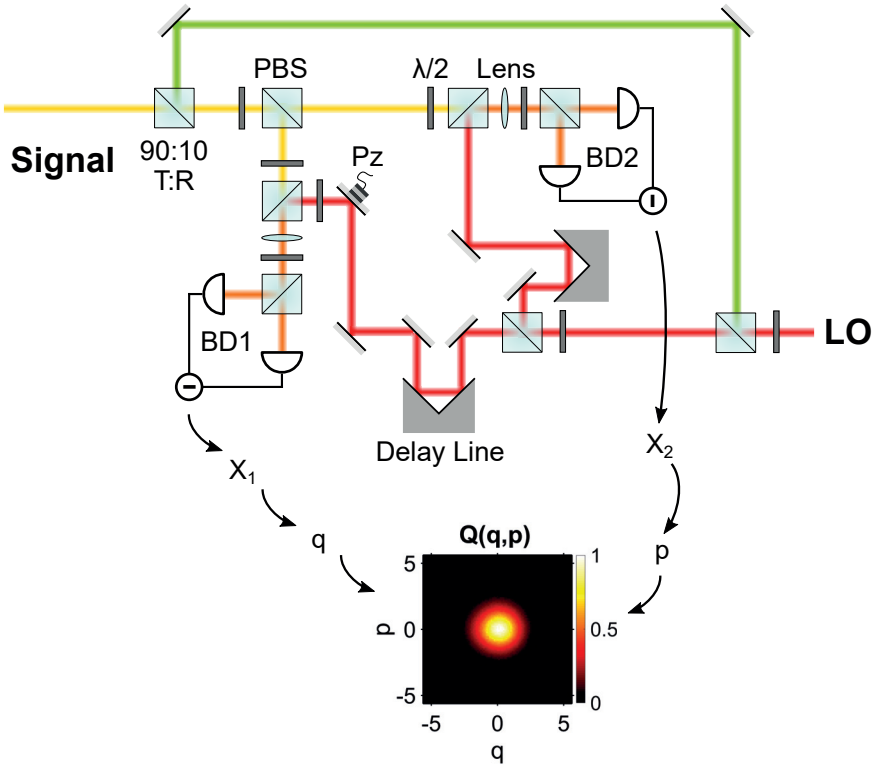

Figure 7.1: Scheme of two-channel homodyne detection. The signal beam (yellow) and the local oscillator beam (LO) (red) are each split into two beams which then interfere in two homodyne detection channels. A piezo mirror (Pz) sweeps the relative phase between the LOs in the two channels. From the LO, an additional beam for alignment of the time delay is derived (green). The two detectors BD1 and BD2 measure the quadratures X_1 and X_2. From these, orthogonal quadratures q and p are selected. A two-dimensional histogram of q and p delivers the Husimi Q distribution. LO: Local oscillator; PBS: polarizing beam splitter; $\lambda/2$: half-wave plate; BD: balanced detector; Pz: Piezo mirror; 90:10: beam splitter with 90% transmission and 10% reflection. The path lengths are not drawn to scale. In the actual setup, all LO paths should have equal lengths and all signal paths should have equal lengths, too.

the two signal beams travel exactly the same distances from their point of separation to the detectors. This can be ensured by using a part of the LO as a signal for alignment (depicted in green in Fig. 7.1). For each channel, one can observe the overlap of this alignment beam (green) and the LO beam (red) on a camera, while slowly scanning the corresponding delay line. The delay line consists of a retroreflector mounted on a motorized translation stage, allowing to change the length of the LO beam path by several centimeters without distorting the beam alignment. If the pulses of the LO beam and the alignment beam travel the same distance, i.e. arrive at the same time, interference fringes appear on the camera. When this optimal delay is found for both channels, the alignment beam can be blocked and the polariton signal can be aligned to travel along the same path.

For the measurements in this chapter, the LO energy was set to 1.6107 eV. The FWHM

of the LO spectrum was 0.003 eV, corresponding to a pulse length of about 660 fs. With such a big spectral width, the LO covers the signal spectrum even when a red- or blue-shift occurs.
Another important feature is a piezo mirror in one of the two LO paths. The mirror is equipped with the piezo actuator S-303.CDI from Physik Instrumente (PI) and controlled by an E-725 piezo controller. With this mirror, the LO path length in this channel can be varied by 2 µm. Thereby, the relative phase between the LOs in the two channels can be swept continuously. A trigger signal is sent from the piezo controller to our digitizer card in order to measure only when the piezo is moving linearly and not changing the direction of movement; see Ref. [The18, p. 45-46]. Later, the data can be sorted into segments according to the piezo movement.

7.2 Obtaining the Husimi function

For obtaining the Husimi function, one needs orthogonal quadratures q and p, i.e. quadratures that are phase-shifted by 90°. However, currently it is not possible to hold the relative phase between the two channels fixed. Therefore, we scan the relative phase continuously by modulating the piezo mirror — typically in a sinusoidal waveform with a frequency of 50 Hz — and later compute the product of the quadratures of the two channels X_1X_2. This product has a sinusoidal shape when plotted against time resulting from the continuous phase sweeping. Then, we select only data where the smoothed product X_1X_2 equals zero within a ±2.5% margin of the peak-to-peak value. These selected quadratures q and p are approximately orthogonal to each other and hence represent coordinates of the phase space.
In the next step, we create a histogram of the occurrences of pairs (q,p), which gives us the Husimi Q distribution of the signal light field [Sch01, p. 367]. See section A.4 in the appendix for the used Matlab scripts.
However, this Husimi function is phase-averaged since the phase of the polariton emission fluctuates on a timescale of 1 ns, given by its coherence time, as observed in Chapter 8. Therefore, in a measurement over several hundred milliseconds, we record all possible phases between signal and LO equally. Nevertheless, the phase-averaged Q function allows us to determine the amount of quantum coherence in the polariton system.
In the next section, we discuss what kinds of Husimi functions are expected for our system and what information we can learn from them.

7.3 Expected Husimi function for coherent, thermal and displaced thermal states of light

In this section, we introduce the expected Husimi functions for the light states investigated in this work. In general, this is the family of displaced thermal states, whose limiting cases are the coherent state and the thermal state, which we introduce first.

7.3.1 Husimi function of a coherent state

The Husimi function of a coherent state is given by [Sch01, p. 324]:

$$Q(\alpha) = \frac{\langle\alpha|\hat{\rho}|\alpha\rangle}{\pi} = \frac{1}{\pi}\exp\left[-|\alpha-\alpha_0|^2\right], \tag{7.1}$$

with the coherent amplitude $\alpha_0 \in \mathbb{C} = |\alpha_0|e^{i\phi}$, where $\phi = \arg\alpha_0$. A visualization is shown in Fig. 7.2 and Fig. 7.3, depicting a Gaussian bell curve located at the offset. The offset can be related to the quadratures, via definition (2.26) and eigenvalue equation (2.7). Thus, we obtain the following expectation values and variances: [2]

$$\begin{aligned}
\langle\hat{q}\rangle &= \langle\alpha_0|\, A(\hat{a}^\dagger + \hat{a})\,|\alpha_0\rangle = A(\alpha_0^* + \alpha_0) = 2A\mathrm{Re}\alpha_0 \equiv q_0; && \text{(7.2a)}\\
\langle\hat{p}\rangle &= \langle\alpha_0|\, Ai(\hat{a}^\dagger - \hat{a})\,|\alpha_0\rangle = Ai(\alpha_0^* - \alpha_0) = 2A\mathrm{Im}\alpha_0 \equiv p_0; && \text{(7.2b)}\\
\langle\hat{n}\rangle &= \langle\alpha_0|\, \hat{a}^\dagger\hat{a}\,|\alpha_0\rangle = |\alpha_0|^2 = (\mathrm{Re}\alpha_0)^2 + (\mathrm{Im}\alpha_0)^2 = \frac{1}{(2A)^2}(q_0^2 + p_0^2); && \text{(7.2c)}\\
\mathrm{Var}(\hat{q}) &= \langle\hat{q}^2\rangle - \langle\hat{q}\rangle^2 = A^2 = \mathrm{Var}(\hat{p}). && \text{(7.2d)}\\
& && \text{(7.2e)}
\end{aligned}$$

The product of the widths $\Delta q\Delta p = A^2$ corresponds to the Heisenberg limit. These widths also correspond to the width of the vacuum state.

Expressed in terms of quadratures, the phase of the state is:

$$\phi = \arctan\left(\frac{p_0}{q_0}\right). \tag{7.3}$$

[2] Note that the expectation values can be either evaluated from knowledge of the coherent state or from the Husimi function. E.g. from the property (2.7) of the coherent state we get for the mean photon number: $\langle\hat{n}\rangle = \langle\alpha_0|\,\hat{a}^\dagger\hat{a}\,|\alpha_0\rangle = \alpha_0^*\alpha_0 = |\alpha_0|^2 = (\mathrm{Re}\alpha_0)^2 + (\mathrm{Im}\alpha_0)^2$.
However, if we evaluate the term with the Husimi function, we have to make sure that the operators are antinormally ordered [Sch01, p. 330]: $\langle\hat{n}\rangle = \langle\hat{a}^\dagger\hat{a}\rangle = \langle\hat{a}\hat{a}^\dagger - 1\rangle = \langle\alpha^*\alpha\rangle_{\mathrm{Husimi}} - 1 = \langle(\mathrm{Re}\alpha)^2\rangle_{\mathrm{Husimi}} + \langle(\mathrm{Im}\alpha)^2\rangle_{\mathrm{Husimi}} - 1$.
Thereby, $\langle x\rangle_{\mathrm{Husimi}} = \int_{-\infty}^{\infty}\int_{-\infty}^{\infty} xQ(\alpha)d\mathrm{Re}(\alpha)d\mathrm{Im}(\alpha)$. This gives the result $\langle\hat{n}\rangle = \frac{1}{2} + (\mathrm{Re}\alpha_0)^2 + \frac{1}{2} + (\mathrm{Im}\alpha_0)^2 - 1 = |\alpha_0|^2$. Thus, both methods yield the same expectation values, but only when the operators are antinormally ordered when averaging over the Husimi function.

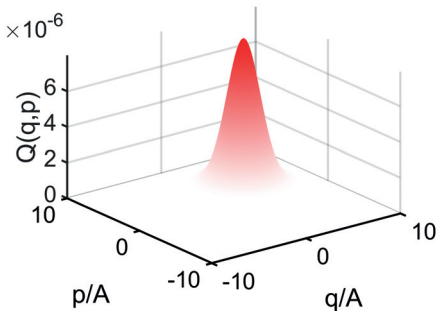

Figure 7.2: Simulated Husimi function of a coherent state with mean photon number $|\alpha_0|^2 = 10$.

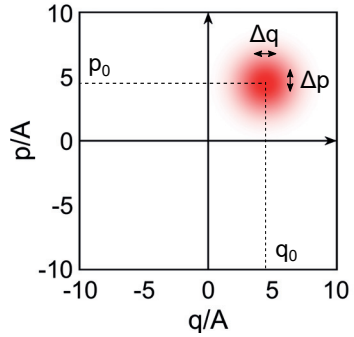

Figure 7.3: 2D image of the simulated Husimi function of a coherent state with mean photon number $|\alpha_0|^2 = 10$. Annotations indicate the offset q_0,p_0 and the widths Δq,Δp.

7.3.2 Husimi function of a thermal state

The other limiting case is the thermal state, whose Husimi function is given by [Sch01, p. 328]:

$$Q(\alpha) = \frac{\exp\left[-\frac{|\alpha|^2}{\bar{n}+1}\right]}{\pi(\bar{n}+1)}, \tag{7.4}$$

with the mean photon number $\bar{n}$. A visualization is shown in Fig. 7.4 and Fig. 7.5. It is a Gaussian that is considerably broader than the coherent counterpart. It has no offset but is centered around zero because the phases of the light field are randomized. Thus, the expectation values are:

$$\langle\hat{q}\rangle = 0; \tag{7.5a}$$
$$\langle\hat{p}\rangle = 0; \tag{7.5b}$$
$$\langle\hat{n}\rangle = \bar{n}; \tag{7.5c}$$
$$\mathrm{Var}(\hat{q}) = \langle\hat{q}^2\rangle - \langle\hat{q}\rangle^2 = \langle\hat{q}^2\rangle = A^2(2\bar{n}+1) = \mathrm{Var}(\hat{p}). \tag{7.5d}$$

7.3.3 Husimi function of a displaced thermal state

As we have seen, the coherent state has the minimum product of quadrature widths and an offset that is related to the coherent photon number. On the other hand, the thermal state has a width related to the thermal photon number and zero offset. Both are limiting cases for the family of displaced thermal states, which possess an offset related to a coherent photon number as well as a width related to a thermal photon number. Mathematically, the displaced thermal state is obtained by applying

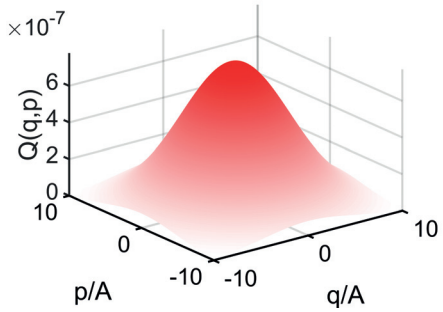

Figure 7.4: Simulated Husimi function of a thermal state with mean photon number $\bar{n} = 10$.

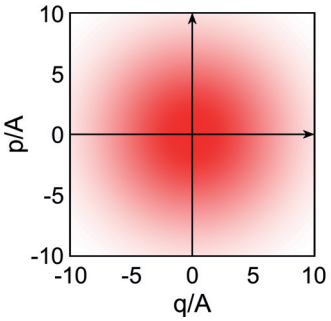

Figure 7.5: 2D image of the simulated Husimi function of a thermal state with mean photon number $\bar{n} = 10$.

a displacement operator to a thermal state. This state represents a superposition of thermal light with coherent light in one mode and is a simple model for single-mode laser light [VW06, p. 131].

For a laser, the coherent light originates from stimulated emission and the thermal light from spontaneous emission. This is different for polaritons, where stimulated scattering of polaritons towards the ground state takes place instead of stimulated emission; see [BKY14] for a comparison of laser and polariton condensate. The emitted light stems from leakage of the photonic part of the polaritons out of the cavity and has the same state as the polaritons up to a rescaling; see Section 3.5. The thermal part of the emission comes from uncondensed polaritons that are thermalized by the phonon bath whereas the coherent part results from condensed polaritons. These polaritons build up coherence when forming a condensate, i.e. they possess a macroscopic wavefunction with a fixed quantum-mechanical phase, which serves as the order parameter [DHY10]. This polariton wavefunction $\Psi = \Psi_0 e^{i\phi}$ describes a macroscopically coherent state. Therefore, it is reasonable to assume that the model of the displaced thermal state applies to polaritons as well. This educated guess is compared to the experimental results in Section 7.5.1. Beforehand, let us review the properties of the displaced thermal state.

The P distribution and density matrix are given in Ref. [VW06, p. 131]; from these we obtain the Husimi function

$$Q(\alpha) = \frac{\exp\left[-\frac{|\alpha-\alpha_0|^2}{\bar{n}+1}\right]}{\pi(\bar{n}+1)}, \tag{7.6}$$

with a width given by the mean thermal photon number $\bar{n}$ and a coherent displacement $\alpha_0 \in \mathbb{C}$, related to the coherent photon number $|\alpha_0|^2$. A visualization is shown in Fig. 7.6. It resembles a coherent state that is broadened due to the thermal background, as specified through the thermal photon number. In the limit $|\alpha_0|^2 \to 0$ the function corresponds to the Husimi function of a thermal state, and in the limit $\bar{n} \to 0$ it

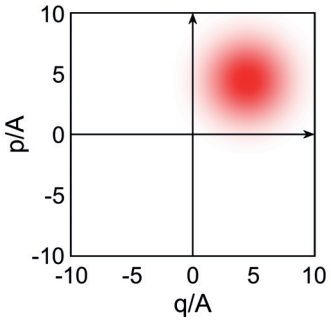

Figure 7.6: 2D image of the Husimi function of a displaced thermal state with $|\alpha_0|^2 = 10$ and $\bar{n} = 1$.

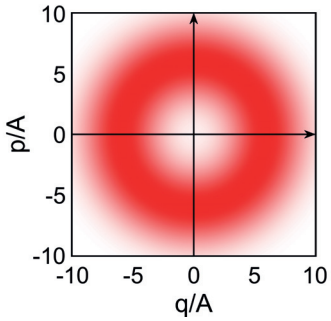

Figure 7.7: 2D image of the phase-averaged Husimi function of a displaced thermal state with $|\alpha_0|^2 = 10$ and $\bar{n} = 1$.

corresponds to a coherent state. If both parameters are zero, we obtain the vacuum state. The expectation values are:

$$\langle \hat{q} \rangle = 2A\mathrm{Re}(\alpha_0) \equiv q_0; \tag{7.7a}$$

$$\langle \hat{p} \rangle = 2A\mathrm{Im}(\alpha_0) \equiv q_0; \tag{7.7b}$$

$$\langle \hat{n} \rangle = \bar{n} + |\alpha_0|^2; \tag{7.7c}$$

$$|\alpha_0|^2 = \frac{1}{(2A)^2}(q_0^2 + p_0^2); \tag{7.7d}$$

$$\mathrm{Var}(\hat{q}) = \mathrm{Var}(\hat{p}) = A^2(2\bar{n} + 1). \tag{7.7e}$$

However, as mentioned above, the emission has no fixed phase relation to the local oscillator in our measurements. Thus, the relative phases between LO and signal are randomized and the obtained Husimi function is a phase-averaged version of the one given by Eq. (7.6). This phase-averaged version reads [LPR+21]

$$\boxed{Q_{\mathrm{pav}}(\alpha) = \frac{\exp\left(-\frac{|\alpha|^2+|\alpha_0|^2}{\bar{n}+1}\right)}{\pi(\bar{n}+1)} I_0\left(\frac{2|\alpha||\alpha_0|}{\bar{n}+1}\right).} \tag{7.8}$$

Herein, I_0 denotes the zeroth modified Bessel function of the first kind, $2\pi\, I_0(\lambda) = \int_0^{2\pi} d\varphi\, e^{\lambda\cos(\varphi)}$. This function is visualized in Fig. 7.7. It looks like a ring, whose width is related to the thermal photon number and whose radius is related to the coherent photon number.

7.4 Calculating the quantum coherence of a displaced thermal state

In Section 2.5 we introduced the quantum coherence as a measure for the amount of superpositions of basis states in the system. If $|\alpha_0|^2 \neq 0$, there are superpositions of

Fock states present, indicated by off-diagonal elements in the density matrix $\rho_{n,m} = e^{-|\alpha_0|^2}\alpha_0^n\alpha_0^{*m}/\sqrt{n!m!} \neq 0$. Thus, if we assume particle states as the classical reference and superpositions of them as a quantum resource, then a coherent state possesses a large amount of quantum coherence.
The exact amount of quantum coherence $\mathcal{C}$ can be computed from the Husimi function. To recall Eq. (2.22), $\mathcal{C}$ is given by

$$\mathcal{C}(\hat{\rho}) = \mathrm{tr}\left(\hat{\rho}^2\right) - \mathrm{tr}\left(\hat{\rho}_{\mathrm{inc}}^2\right), \tag{7.9}$$

where ρ_{inc} is an incoherent state with the same diagonal elements as the original state. Before, we expressed these terms in the Fock basis, but they can also be calculated from phase-space distributions. Specifically, the best incoherent approximation $\hat{\rho}_{\mathrm{inc}} = \sum_n \rho_{n,n}|n\rangle\langle n|$ [SW18] is obtained by a phase-averaging over the corresponding phase-space distribution [LPR+21]. Thus, $\hat{\rho}_{\mathrm{inc}}$ corresponds to the phase-averaged Husimi function Q_{pav} from Eq. (7.8). Note that, as explained above, we only measure the phase-averaged Husimi function, which actually constitutes the incoherent limit we use here. However, we can reasonably assume that the state is in fact a usual displaced thermal state and the phase averaging only occurs due to the lack of phase stability between LO and signal. Thus, the measured phase-averaged function allows us to derive the parameters $\bar{n}$ and $|\alpha_0|^2$ of the original displaced thermal state and to compute the quantum coherence from them as follows.
To obtain $\mathcal{C}(\hat{\rho})$, we need the purities $\mathrm{tr}\,(\hat{\rho}^2)$ and $\mathrm{tr}\,(\hat{\rho}_{\mathrm{inc}}^2)$. In general, the purity of a state can be written as

$$\begin{aligned}\mathrm{tr}\left(\hat{\rho}^2\right) =& \int d^2\alpha\, d^2\alpha'\, P(\alpha)P(\alpha')\exp\left(-|\alpha-\alpha'|^2\right)\\ =& \pi\int d^2\alpha P(\alpha)Q(\alpha),\end{aligned} \tag{7.10}$$

where we used the Glauber-Sudarshan P distribution P, the overlap $|\langle\alpha|\alpha'\rangle|^2 = e^{-|\alpha-\alpha'|^2}$ and the representation $Q(\alpha) = \langle\alpha|\hat{\rho}|\alpha\rangle/\pi$ for the Husimi function.
For the displaced thermal state, we obtain the purities

$$\mathrm{tr}\left(\hat{\rho}^2\right) = \frac{1}{(\bar{n}+1)^2-\bar{n}^2} \tag{7.11}$$

and

$$\mathrm{tr}\left(\hat{\rho}_{\mathrm{inc.}}^2\right) = \frac{\exp\left[-\frac{2|\alpha_0|^2}{(\bar{n}+1)^2-\bar{n}^2}\right]}{(\bar{n}+1)^2-\bar{n}^2} I_0\left[\frac{2|\alpha_0|^2}{(\bar{n}+1)^2-\bar{n}^2}\right]. \tag{7.12}$$

The difference of both purities then yields the coherence measure from Eq. (2.22) for displaced thermal states:

$$\boxed{\mathcal{C}(\hat{\rho}) = \frac{1 - \exp\left[-\frac{2|\alpha_0|^2}{(\bar{n}+1)^2-\bar{n}^2}\right] I_0\left[\frac{2|\alpha_0|^2}{(\bar{n}+1)^2-\bar{n}^2}\right]}{(\bar{n}+1)^2 - \bar{n}^2}.} \tag{7.13}$$

Thus, the quantum coherence of displaced thermal states only depends on the parameters $\bar{n}$ and $|\alpha_0|^2$, visualized in Fig. 7.8.

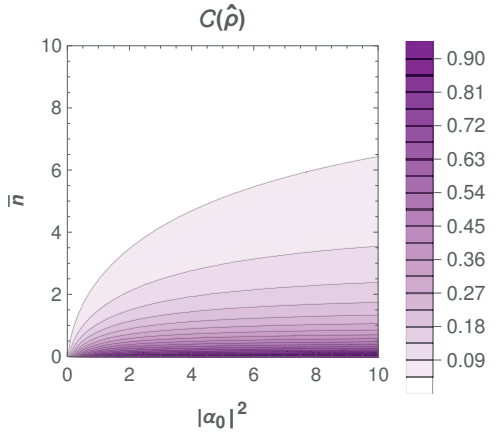

Figure 7.8: Quantum coherence $\mathcal{C}(\hat{\rho})$ as a function of the coherent and thermal photon numbers, $0 \leq |\alpha_0|^2 \leq 10$ and $0 \leq \bar{n} \leq 10$, respectively. The quantum coherence increases with increasing displacement α_0 and reduces when the thermal background $\bar{n}$ increases. The figure is taken from Ref. [LPR+21].

As can be seen, the quantum coherence becomes large for high coherent photon number $|\alpha_0|^2$ and for low thermal photon number $\bar{n}$. Furthermore, $\mathcal{C}$ even monotonically increases with $|\alpha_0|^2$ and monotonically decreases with $\bar{n}$ [LPR+21]. It saturates at a maximum value of 1 in the limit of a large coherent amplitude, $|\alpha_0| \to \infty$, and vanishing thermal background, $\bar{n} \to 0$.

With this knowledge, quantum coherence can be quantified by measuring the Husimi function of the polariton condensate emission, indicating the system's usefulness for quantum protocols.

7.5 Results

7.5.1 Measured Husimi functions

In the following, we fix the normalization $A = \frac{1}{\sqrt{2}}$, i.e. the commutator convention $[\hat{q},\hat{p}] = i$.

First, let us examine two exemplary measured Husimi functions for the dominant 0° linear polarization. Figure 7.9(a) shows a Husimi function measured at $P_{\text{exc}} = 30\,\text{mW}$ and (b) at $P_{\text{exc}} = 226\,\text{mW}$. The measured functions are fitted with the model of a displaced thermal state, from which the thermal and coherent photon numbers are ob-

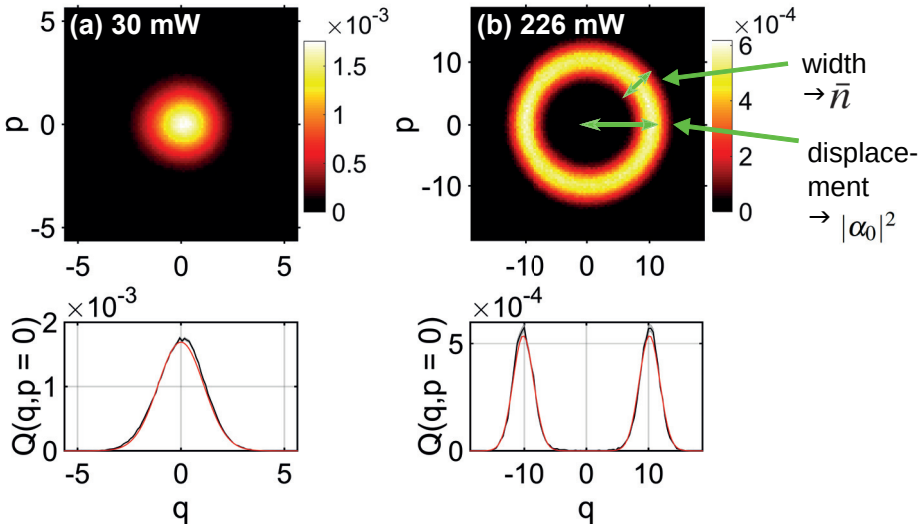

Figure 7.9: Measured phase-averaged Husimi functions for (a) $P_{\mathrm{exc}} = 30\,\mathrm{mW}$ and (b) $P_{\mathrm{exc}} = 226\,\mathrm{mW}$. In (b), the offset and the width are indicated, which deliver the values of $|\alpha_0|^2$ and $\bar{n}$, respectively. The bottom plots show cuts along $p = 0$. The black line corresponds to the data, with the shaded area (that is mostly not visible) representing a one standard-deviation error margin that results from the standard error of the counting statistics. The red curve depicts the fitted model of a displaced thermal state. Adapted from [LPR+21].

tained. The fits are shown in the lower panels for a cut around $p = 0$. Apparently, the model of a displaced thermal state matches our measured data well.

At 30 mW, the Husimi function is a Gaussian distribution around zero. This corresponds to a thermal state with almost zero coherent photons and $\bar{n} = 0.214 \pm 0.003$ thermal photons.

In contrast, at 226 mW, the Husimi function resembles a ring with a radius of $(q_0^2 + p_0^2)^{1/2} = 10.4$ in quadrature units, as expected for a phase-averaged displaced thermal state, cf. Fig 7.7. From the width of the ring, the thermal photon number $\bar{n} = 1.71 \pm 0.01$ can be derived, and from the displacement we obtain the coherent photon number $|\alpha_0|^2 = (q_0^2 + p_0^2)/2 = 53.01 \pm 0.02$ according to Eq. (7.7d).

Thus, somewhere between these two powers, a phase transition from a thermal to a mostly coherent state must occur. This spontaneous appearance of coherence in the polariton system can be related to Bose-Einstein condensation, cf. Sections 3.4 and 3.5.

Before we study this transition in a series of excitation power measurements, we must remark one difficulty. The two Husimi functions shown in Fig. 7.9 were both created with data from a complete measurement that takes several hundred milliseconds. However, this only works if the state of light is sufficiently stable during this time span. Nevertheless, in a certain range of powers, i.e. 170 mW to 205 mW, the emission is not

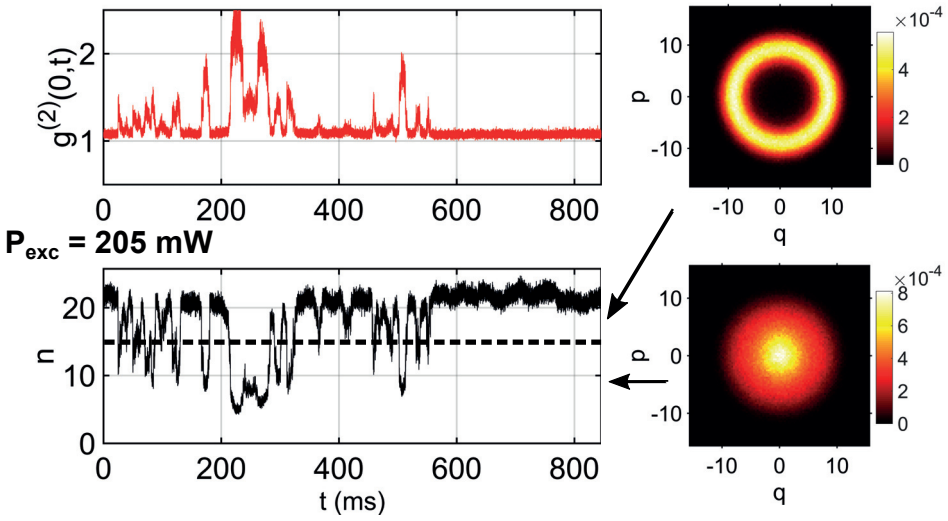

Figure 7.10: Bistable emission at $P_{\mathrm{exc}} = 205\,\mathrm{mW}$. On the upper and lower left side, the time-resolved $g^{(2)}(\tau = 0,t)$ and photon number is shown, respectively. The initial time $t = 0$ is chosen as the beginning of the measurement. A dashed line in the bottom panel indicates the distinction between the states with high and low intensity. For these two states, the Husimi functions are shown on the right. Adapted from [LPR+21].

stable but switches between a state with high intensity and one with low intensity, as can be seen in a plot of the time-resolved photon number and $g^{(2)}(\tau = 0,t)$ in Fig. 7.10.

In the high state, $g^{(2)}(\tau = 0,t)$ is close to one, indicating mostly coherent emission, while in the lower state, $g^{(2)}(\tau = 0,t)$ lies around two, implying mostly thermal light. Therefore, it does not make sense to sample one Husimi function from the complete dataset, but to create one Husimi function for each of the two states separately. To differentiate between both states, we define the "high" state where the photon number exceeds the mean of the maximum and minimum photon number of the dataset and the "low" state as the instances with a photon number below that. This distinction between both states is marked with a dashed line in the bottom panel of Fig. 7.10. The Husimi functions for these two states are shown on the right.
Consequently, in the range of powers where bistability occurs, we create separate Husimi functions for the low and the high state, perform a fit for each of them and receive two separate resulting sets of parameters. Thus, our time-resolved detection method allows us to take the bistability of the semiconductor dynamics into account, the causes of which we will elaborate further in the following.

7.5.2 Dependence on excitation power

In order to investigate the transition towards the condensed state, the Husimi functions are measured for varying excitation power. From each Husimi function, we obtain the thermal and coherent photon numbers $\bar{n}$ and $|\alpha_0|^2$ via fitting the displaced thermal state

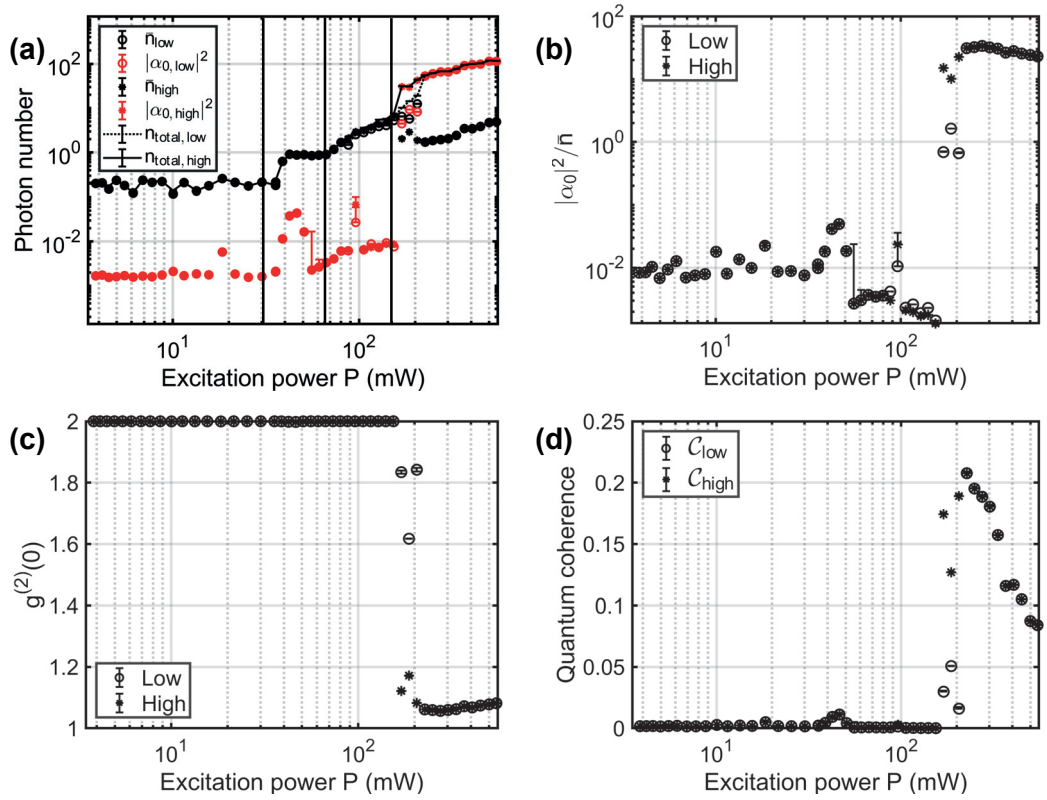

Figure 7.11: Results obtained from fitting the Husimi functions versus excitation power for 0° polarization. (a) Coherent (red circles) and thermal (black circles) photon numbers. The black line shows the total photon number n_{total}. Black vertical lines mark thresholds between different regimes of emission. (b) Ratio between the coherent and thermal photon numbers. (c) Equal-time, second-order correlation function $g^{(2)}(\tau = 0)$. (d) Amount of quantum coherence. Open and closed symbols correspond to the low and high state of the bistable emission, respectively. When both symbols overlap, the emission is stable. Error bars are obtained from a Monte Carlo error propagation (see Appendix B for details); because of the asymmetry of the logarithmic scale, only the upper part of the error margin is shown. Adapted from [LPR+21].

model to the data. From these photon numbers, we calculate the quantum coherence $\mathcal{C}$ via Eq. (7.13). Furthermore, a mean value for $g^{(2)}(\tau = 0)$ can be computed via Eq. (2.20). All these quantities are plotted versus excitation power for the dominant 0° linear polarization in Fig. 7.11. Let us now examine the power-dependence of these values in order to study the phase transition of the system, and, most importantly, the build-up of quantum coherence.

For low excitation powers, $|\alpha_0|^2$ is two orders of magnitude smaller than $\bar{n}$ and the correlation function $g^{(2)}(\tau = 0)$ equals 2, indicating almost completely thermal emission. Also, the amount of quantum coherence is close to zero. From this follows that the polaritons in the sample are in an incoherent state without quantum superpositions. Since the thermal phonon bath induces polariton relaxation [HSQ+10, SQ08], and the polaritons cannot directly inherit the coherence from the nonresonant excitation, they

form a thermal ensemble as long as the critical density for condensation is not reached.

Slightly above the power of 30 mW, where we found a non-linear intensity increase in the dispersions (cf. Chapter 5.2.1), both the thermal and coherent photon numbers rise. In particular, the coherent photon number $|\alpha_0|^2$ increases significantly, and the quantum coherence $\mathcal{C}$ as well. Probably, this behavior corresponds to the emergence of a macroscopic occupation in the ground state, enabling stimulated scattering to the ground state and initializing the condensation process.

However, when the power is increased further, the coherent photon number and the quantum coherence drop again, and the total photon number stays on a plateau up to about 65 mW. Also, $g^{(2)}(\tau = 0)$ is still 2 because the thermal photon number is much higher than the coherent photon number. Notably, in this power range, we observed in the dispersions an appearance of emission around $k = \pm 0.8\ \mu\text{m}^{-1}$ that competes for the formation of a condensate, cf. Chapter 5.2.1. These modes at higher k values do not overlap with the LO and are therefore not measured with our homodyne detection setup. Because of this competition of polaritons being scattered to higher k states, the critical density in the ground state is not achieved, and a condensate at $k = 0$ cannot form yet.
These higher k modes fade away for $P_{\text{exc}} > 60$ mW and the emission from $k = 0$ predominates, leading to an increase in the total photon number n_{total}. But still there is too much gain competition from the other modes, which can be also seen in Chapter 5.2.1, to enable the build-up of quantum coherence in the ground state.

Only for powers above 170 mW, there is a significant rise of the coherent photon number and the quantum coherence, accompanied by a drop of $g^{(2)}(0)$. However, in the range between 170 mW and 205 mW, the emission is not stable but switches between high and low intensity, as shown in Fig. 7.10. In this range of powers, the gain competition with the orthogonal 90° polarization comes into play that was also observed in Chapter 5.2.1. There, we found this competition in a similar range of powers up to 200 mW. This assumption is further confirmed by the excitation-power dependence of Husimi function fit parameters for the 90° polarization that is shown in Fig. 7.12. Here, a significant coherent photon number, quantum coherence and a reduction of $g^{(2)}(0)$ are found in the power range of 140 - 206 mW. Thus, in this range of powers, there is a formation of a state with coherent quantum superpositions, but it is alternating between the two polarizations.

Eventually, at 226 mW, the 0° polarized emission becomes stable and reaches the maximum observed amount of quantum coherence, $\mathcal{C} = 0.208 \pm 0.001$. This value is in good agreement to the one expected from a numerical simulation, $\mathcal{C} = 0.2$, as discussed in the next Section 7.6. Also, $g^{(2)}(0)$ reaches a minimum value of 1.0615 ± 0.0003. This

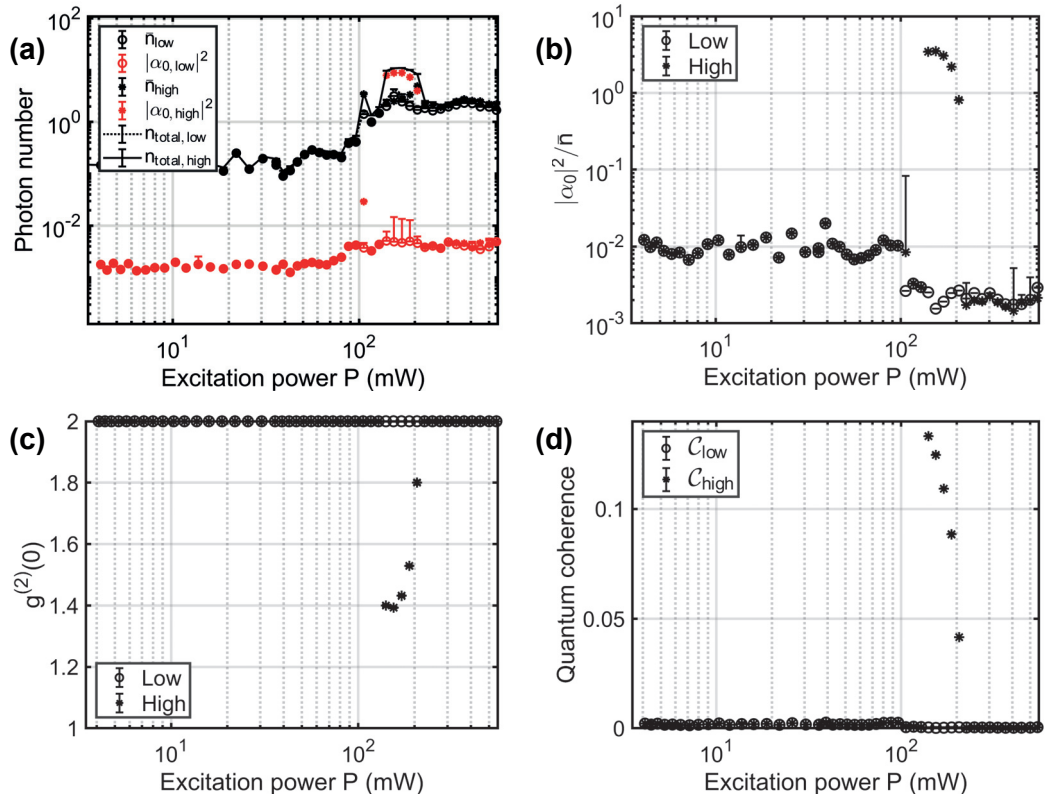

Figure 7.12: Fitted photon numbers from the Husimi functions, $g^{(2)}(\tau = 0)$ and quantum coherence versus excitation power for 90° polarization.

observation of $\mathcal{C} > 0$ tells us that there are significant quantum superpositions of Fock states present in the polariton system, cf. Section 2.5 and 7.4.

Finally, for excitation powers above 226 mW, the coherent photon number saturates whereas the thermal photon number further increases, leading to a slight increase in $g^{(2)}(\tau = 0)$ and a loss of quantum coherence. For these higher powers, the sample is heated by the pump laser, which causes decoherence via the thermal bath of the lattice and carriers. The effect of heating can also be observed in a redshift of the polariton emission in Fig. 5.4(d). Another effect leading to decoherence is the polariton-polariton interaction that increases for higher powers.

7.6 Comparison to numerical simulations

In addition to the measurements, a numerical simulation was performed at Paderborn University by Matthias Pukrop in the group of Stefan Schumacher in order to confirm the build-up of quantum coherence in the polariton condensate. The numerical results are also published in Ref. [LPR+21]. The simulation is based on an open-dissipative

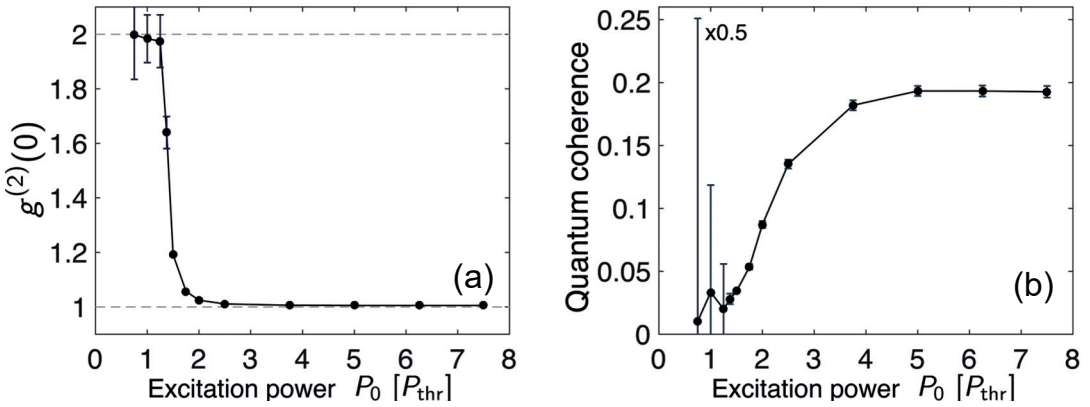

Figure 7.13: Results from a numerical simulation versus excitation power. (a) Photon correlation $g^{(2)}(\tau = 0)$. (b) Quantum coherence. Adapted from [LPR$^+$21].

Gross-Pitaevskii equation (which describes the dynamics of the order parameter for Bose-Einstein condensation [PS03]) coupled to an incoherent reservoir. In order to study coherence properties, fluctuations are included with the help of the truncated Wigner approximation [CC13, SLC02, WS09]. With this approximation, one obtains a set of stochastic partial differential equations that describe the temporal evolution of the polariton field ψ on a finite two-dimensional grid when coupled to an incoherent reservoir [WS09]. These equations include several microscopic and intrinsic properties of the sample, namely the decay rates of the condensate and the reservoir γ_c and γ_r, the interaction strength between polaritons g_c, the condensation rate R and the condensate-reservoir interaction g_r. The parameter values used in the simulation can be found in Ref. [LPR$^+$21]. Also, Wiener noise is included to account for classical and quantum fluctuations, making the equations stochastic.

The equations are then solved via a fourth-order stochastic Runge-Kutta algorithm [HP06]. To this aim, 300 (below threshold, 200 otherwise) stochastic realizations of the system are evolved over a time interval of 4 ns with a fixed time step of 0.04 ps. Then, the expectation values of the sought-after quantities are given by the steady-state average over those realizations, making use of Monte Carlo techniques. Thereby, the average is taken across a small square in k space in the vicinity of $k \approx 0$.

Specifically, one obtains the expectation values of the mean polariton number and its variance inside the selected k space area. From these, the mean thermal and coherent polariton number can be computed with help of Eq. (2.19), giving the photon correlation $g^{(2)}(0)$ via Eq. (2.20) and the quantum coherence via Eq. (7.13). The results for different excitation powers are shown in Fig. 7.13.

The excitation-power dependence shows a phase transition from a mostly thermal ($g^{(2)}(0) \approx 2$) to a mostly coherent ($g^{(2)}(0) \approx 1$) state. During this transition, the quantum coherence $\mathcal{C}$ reaches a value of about 0.2. Furthermore, it is evident that $g^{(2)}$ and quantum coherence describe distinct properties since $g^{(2)}$ reaches saturation for lower

powers than $\mathcal{C}$.
Let us now compare these results to the experimental ones. First of all, both in simulation and experiment, we observe a phase transition of the system accompanied by a rapid decrease of $g^{(2)}(\tau = 0)$ and an increase of quantum coherence. In both cases, the maximum value of quantum coherence is very similar, indicating that the simulation describes the system well.
However, there are also a few differences between simulation and experiment. First, the simulation delivers the polariton number inside the sample whereas the experiment measures the photon number outside the sample; however, both are directly proportional to each other [LPR$^+$21].
Furthermore, the threshold found in the simulation is also the power where $g^{(2)}(\tau = 0)$ drops. In the experimental system, the behavior is more complicated because of the aforementioned mode competition that is not included in the simulation. Thus, the threshold for an intensity increase in the dispersion does not directly coincide with a decrease of $g^{(2)}$ and a build-up of quantum coherence in the selected mode. Instead, one could define the threshold for our purposes as the power where the coherent photon number rises in the selected mode. Then, the threshold is comparable to the simulation. In addition, in the experiment the quantum coherence decreases again for higher powers due to heating and polariton-polariton scattering. This is not taken into account in the simulation, thus the quantum coherence stays on a plateau for higher powers.

However, since the simulated and experimentally determined maximum amount of quantum coherence matches closely, the simulation describes the experiment well enough. Furthermore, the simulation allows us to probe how the maximum amount of quantum coherence reacts to changes of the microscopic parameters, which are fixed in the experiment. Specifically, the saturation value of $\mathcal{C}$ increases slightly with decreasing interaction strength between polaritons g_c and increasing condensation rate R. The parameter g_c is mostly influenced by the detuning since the interaction between polaritons is caused by the excitonic part of the polaritons and is therefore stronger if they are more excitonic. The condensation rate R describes the scattering rate from the reservoir into the condensate, which depends on the detuning but also on the overlap between reservoir and condensate. However, the quantum coherence is not very sensitive to changes of these parameters. Furthermore, changing the decay rate of the condensate γ_c has almost no influence on the quantum coherence.

7.7 Conclusion

To conclude, I have measured the phase-averaged Husimi function of the emission from a nonresonantly driven polariton condensate using two-channel homodyne detection.

The experimentally determined Husimi function was found to be in good agreement to the model of a displaced thermal state. With increasing excitation power, the emission underwent a transition from a mostly thermal to a mostly coherent state.
I observed not only a drop of the photon correlation $g^{(2)}(0)$ from 2 towards 1, but most importantly, a build-up of a significant amount of quantum coherence, $\mathcal{C} \approx 0.2$, which was confirmed both by the experiment and by a numerical simulation. While the decrease in $g^{(2)}$ corresponds to a transition of the photon statistics — given by the diagonal density matrix elements — from a thermal to a Poisson one, the build-up of quantum coherence proves the presence of off-diagonal density matrix elements. Thus, there are significant quantum superpositions of Fock states present in the polariton system, cf. Section 2.5 and 7.4. These quantum superpositions provide a resource for quantum protocols and could be transformed into entanglement, cf. Section 2.5. Therefore, the polariton system might be useful for certain quantum-information processing tasks. Hereby, polaritons are advantageous compared to ordinary lasers since they possess quantum coherence both in the emitted light and in the matter system, enabling both information transfer and local computing as a so-called hybrid system, whereas the laser only possesses quantum coherence in the emitted light. Furthermore, the polariton condensate occurs at a carrier density that is several orders of magnitude smaller than for a laser and is thus more energy efficient [DHY10, DP12].
However, I have not carried out a quantum protocol in this work but laid the foundation for further investigations. Importantly, I showed the capability of our homodyne detection method to characterize quantum optical properties of a system via the emitted light.
As an outlook, the value of quantum coherence still leaves room for improvement since only 20% of what is possible was reached. To optimize this value, different pump shapes might be employed to spatially separate condensate and reservoir, whereby a spatially narrow ring-shaped pump profile is particularly promising; a ring-shaped profile improves the quantum coherence with unchanged or increased polariton number and a smaller pump spot improves the quantum coherence but reduces the polariton number [Puk22]. Besides, vortex modes might deliver a higher quantum coherence [Puk22]. Furthermore, for quantum information tasks it is also important how fast the quantum coherence decays. Here, I only measured a steady-state value. The temporal dynamics is investigated in the next Chapter 8.

Chapter 8

Three-channel homodyne detection: Tracking quantum coherence from the regularized P function

In the previous Chapter 7, I measured the Husimi function of polariton emission and quantified the amount of quantum coherence carried by the state. Yet, these measurements were conducted for a steady-state light field and did not reveal the temporal decay of quantum coherence. But applications in quantum information processing need temporally stable quantum superpositions, therefore their evolution should be investigated.

The dynamics of coherence in polariton condensates has been previously studied, mainly by measuring the field correlation $g^{(1)}$ with help of Michelson and Mach-Zehnder interferometry and the second-order correlation $g^{(2)}$ via Hanbury Brown–Twiss interferometry; see Section 3.5. But these correlation functions do not yield information about quantum coherence, as explained in Chapter 2.

Furthermore, the measurements in Chapter 7 were phase-averaged, not giving a phase-sensitive quantum state description of the polariton emission.

To improve these shortcomings, in this chapter, I present time-resolved and phase-sensitive measurements of an advanced phase-space function, the regularized P function P_Ω, allowing me to track the evolution of quantum coherence.

To this aim, I use the nonstationary quantum tomography method that was introduced by Johannes Thewes, Marc Aßmann and myself [The18, TLA20]. Usually, for tomography with homodyne detection, a stable phase between LO and signal is required. But when a semiconductor is excited nonresonantly and the luminescence is studied, the exciting laser can not be used as an LO because it has a different wavelength than the signal. Thus, there is no available phase reference and the usual method is not applicable. To circumvent this problem, Thewes et al. developed an advanced method to reconstruct the phase with help of three homodyne channels, where no fixed phase

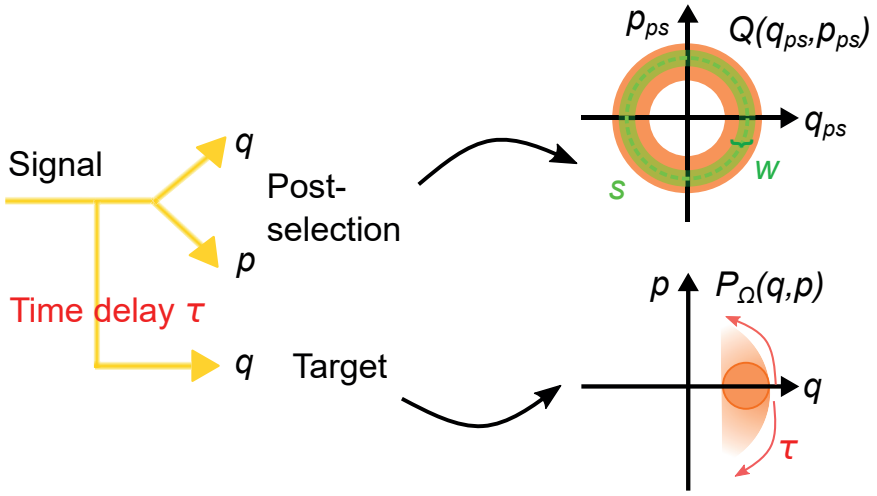

Figure 8.1: Basic idea of nonstationary quantum tomography. The signal is split into three homodyne detection channels. Two of them constitute the postselection / proxy channel, where the Husimi function is measured. The third one is the target channel with an adjustable time delay τ. From the measured Husimi function, a ring-shaped region with radius s and width w is selected after data acquisition. The corresponding quadratures in the target channel q and the reconstructed phase allow to sample the regularized P_Ω function, whose decay with growing time delay can be observed.

reference is needed. This multi-channel homodyne detection is a powerful tool for monitoring the stochastic dynamics of a light field, depending on initial conditions that can be freely postselected.

From the phase-sensitive data acquired in such a way, I sample the relatively new phase-space function P_Ω directly using pattern functions. I quantify the quantum coherence based on the phase variance of P_Ω and observe its decay, finding exceptionally long coherence times up to 1390 ps. These findings are supported by simulations carried out by the group of Stefan Schumacher at Paderborn University. The quantum information theory was provided by Jan Sperling at Paderborn University. This chapter is mostly based on a manuscript titled "Tracking quantum coherence in polariton condensates with time-resolved tomography", which is submitted for publication [LPB+].

8.1 Three-channel setup

The basic idea of the nonstationary quantum tomography method is illustrated in Fig. 8.1. A detailed explanation of the setup can be also found in Ref. [The18].

The signal is split into three partial beams, each of which is sent to a homodyne detection unit for measuring the field quadratures. Two of these channels, called post-selection or proxy channels, are kept at the same temporal delay. From these, we select orthogonal quadratures q_{ps} and p_{ps} and assemble the Husimi function $Q(q_{ps},p_{ps})$ as explained in Chapter 7. The third channel, called target channel, has a time delay τ

set by a delay line with respect to the proxy channels. After acquiring quadratures in all three channels, the postselection step follows where we choose an annular region of the Husimi function, specified by a radius s and a width w, thereby selecting a range of momentary intensities of the signal. For example, if s exceeds the average radius of the Husimi function, this means we select all instances when the momentary intensity was above average. For these instances, we pick the corresponding quadratures q of the target channel and we also reconstruct the phase φ as explained below. Then, we are able to reconstruct the P_Ω function for these (q,φ) values. By setting different delays τ between target and proxy channels, we can observe how the P_Ω function relaxes towards the steady state, giving us insight both in the decay of phase and amplitude. This continuous-variable approach renders it possible to resolve the complete phase space for the selected light mode and to analyze the dynamics of different phase-space regions separately.
In some way, our method is similar to a pump-probe experiment. But while in a pump-probe scheme, the sample is excited with a pump laser and then probed with a probe laser after some time delay, here we do not excite the system actively but select a posteriori from the data when the system was excited stochastically in order to monitor spontaneous processes. A similar concept can be found e.g. in spin-noise spectroscopy, where one observes stochastic fluctuations of spin orientations in a sample [CRBS04, ORHH05]; but contrary to our method, spin-noise spectroscopy operates in the frequency domain.

Let us now explain the setup in more detail. A schematic drawing is displayed in Fig. 8.2 while Fig. 8.3 shows the complete setup as it was realized on the optical table.

The sample is excited with a wide-Gaussian spot as before. The polarization of the emission is selected with a half-wave plate and a Glan–Thompson prism. In this chapter, only the dominant 0° linear polarization is measured. LO and signal are each split into the three channels for homodyne detection. For the measurements in this chapter, the LO's wavelength was resonant to the most intense zero-momentum ground-state mode of the polariton emission at 1.6109 eV, having a spectral FWHM of 1.88 nm or 0.004 eV, corresponding to a pulse duration of about 460 fs. With such a big spectral width, the LO covers the signal spectrum even when a red- or blue-shift occurs.
The two proxy channels are set to equal delay as explained in 7.1 while the delay τ of the target channel is varied with a delay line. For each delay, a dataset of quadratures X_1, X_2, and X_3 in the three channels is measured. The photon numbers are set equal in the proxy channels but smaller in the target channel since this provides a reduced phase uncertainty [The18, TLA20]. For example, for the highest excitation power, I sent 14 photons into each of the proxy channels, giving 28 in total, and 9 photons into the target channel.
During measurement, the relative phase between the channels is swept continuously

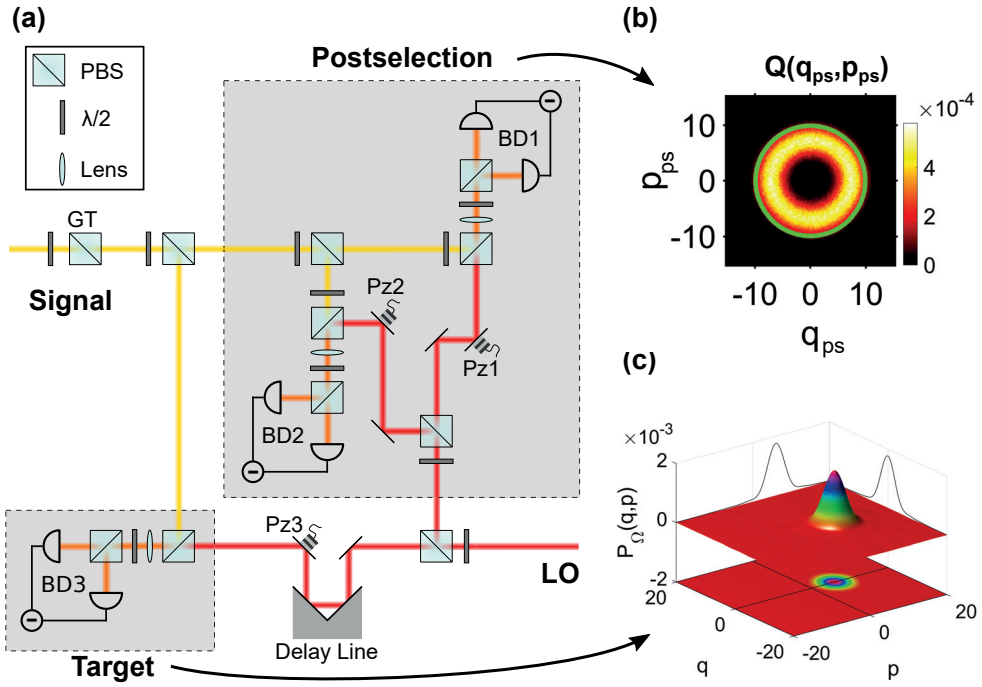

Figure 8.2: Experimental setup (a). The signal is split into three channels and interfered with the local oscillator (LO), before being detected by a balanced homodyne detector (BD). The two postselection channels measure the Husimi Q function (b) of the signal light field while the target channel is used to reconstruct the regularized P_Ω function (c). The green ring in (b) exemplifies one selected phase-space region. PBS: polarizing beam splitter; GT: Glan-Thompson prism; $\lambda/2$: half-wave plate; Pz: piezo mirror; BD: balanced detector.

by a piezo mirror in the LO path in one of the proxy channels. This is necessary for finding the orthogonal quadratures for assembling the Husimi function, see Section 7.2, but also for reconstructing the relative phase to the target channel. The trigger signal from the piezo controller is used to restrict measurements to the linear piezo movement intervals and to sort the data into segments for the back-and-forth movement directions; see Ref. [The18, p. 45-46].

8.2 Data processing for postselection and phase reconstruction

In this chapter, we fix the normalization $A = 1$ such that the fluctuation for vacuum yields $\Delta q_{\text{vac}} = 1$ and the commutator convention obeys $[\hat{q},\hat{p}] = 2i$.
The Matlab scripts for data processing are explained in the Appendix A.5.
After computing and normalizing the quadratures, we remove a slow drift of the mean photon numbers over the course of the delay series and only use data where the photon number is stable inside a given range during one measurement, omitting jumps outside

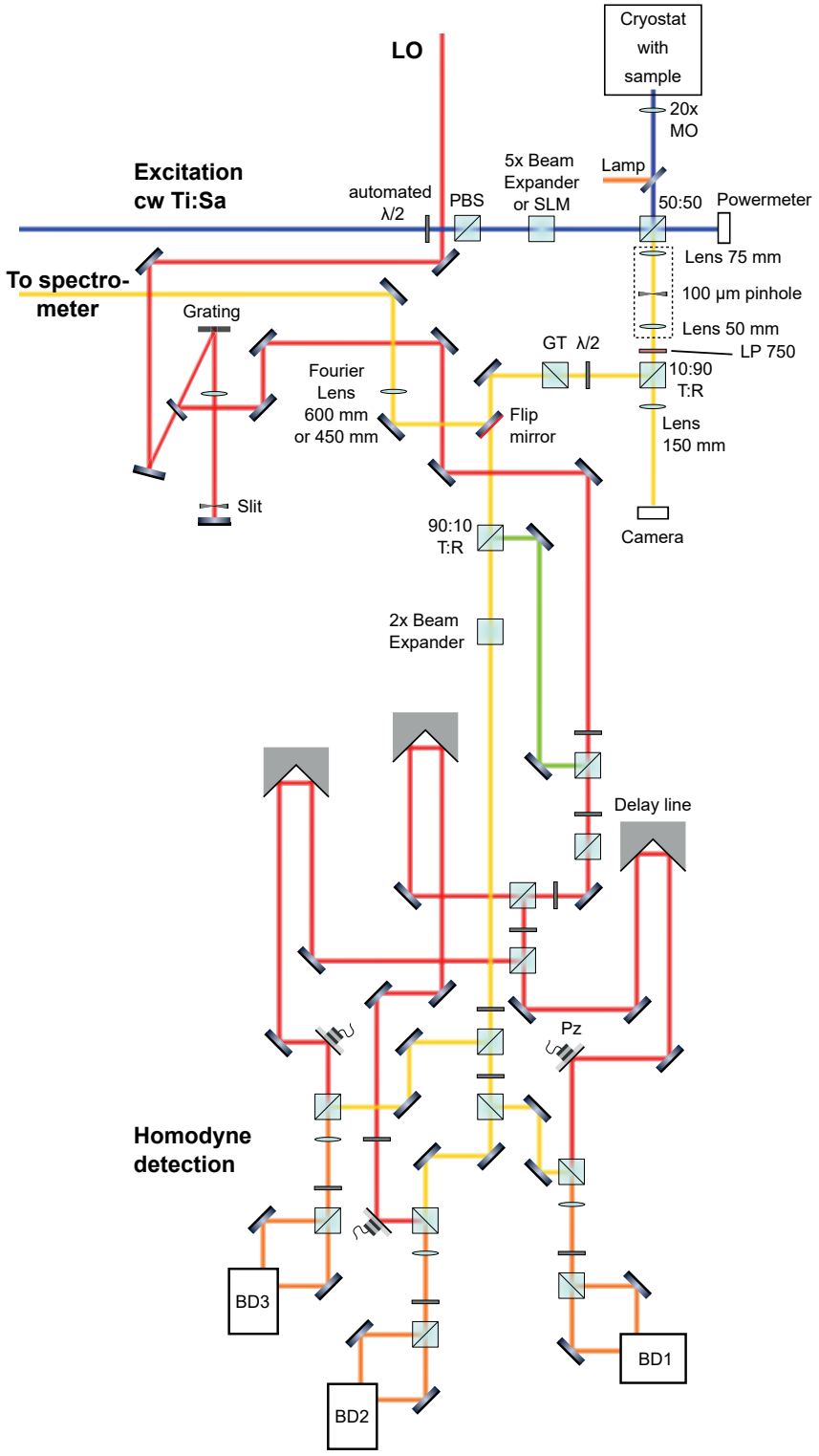

Figure 8.3: The complete setup as realized on the optical table. PBS: polarizing beam splitter; GT: Glan-Thompson prism; $\lambda/2$: half-wave plate; Pz: piezo mirror; BD: balanced detector.

that range. The following process is also elaborated in more detail in Ref. [The18, p. 79-84].
Let us assume here that X_1 and X_2 are the quadratures from the two proxy channels, where X_1 is from the channel subject to piezo modulation, and X_3 corresponds to the target channel. From the quadratures X_1 and X_2 we pick orthogonal quadratures q_{ps} and p_{ps} and assemble the Husimi distribution $Q(q_{ps},p_{ps})$ as described in 7.2.
Besides, we calculate the relative phase between the signal in the target channel and the LO. To this aim, we need two partial phases; one of them is the relative phase between signal and LO in the postselection channels $\varphi_{ps} = \arctan(p_{ps}/q_{ps})$, using the four-quadrant inverse tangent function. The other one is the relative phase $\Delta\varphi$ between the LOs in postselection and target channel, which is derived from the time dependence of $X_1 \times X_3$. This product $X_1 \times X_3$ has a sinusoidal time dependence due to the piezo modulation in channel 1. Applying an inverse sine function to the smoothed product delivers the relative phase $\Delta\varphi$ between the LOs. From these two partial phases, the relative phase between signal and LO in the target channel φ is computed via $\varphi = (\Delta\varphi + \varphi_{ps}) \bmod 2\pi$.
Altogether, we obtain a dataset $(q_{ps},p_{ps},X_3,\varphi)$. From this, we select an annulus-shaped phase-space region of the Husimi function, specified by a radius s and a thickness w. An example is indicated in green in Fig. 8.2. For this selection, we pick the corresponding target quadrature values $q_i \in X_3$ and the corresponding phases φ_i. This dataset $\{(q_i,\varphi_i)\}_{i=1,\ldots,N}$ is then used to reconstruct the regularized P function as explained in the following.

8.3 The regularized P distribution

This section derives the specific regularized P distribution we are using [LPB+], following the general approach in Ref. [KV10]. As discussed in Section 2.7, well-behaved phase-space functions can be obtained by convoluting the Glauber-Sudarshan P distribution with a kernel. Gaussian kernels provide the well-known Husimi and Wigner functions, but to avoid some of their drawbacks, non-Gaussian kernels have been introduced. To this aim, we convolute the P distribution with a non-Gaussian kernel Ω:

$$P_\Omega(\alpha) = \int_{\mathbb{C}} d^2\alpha' \, \Omega(\alpha') P(\alpha - \alpha'). \tag{8.1}$$

Ω should be a sufficiently smooth, non-negative, and normalized function, i.e., probability density, and it has to ensure that $P_\Omega(\alpha)$ is not singular. Also a non-negative $P_\Omega(\alpha)$ is desirable for classical states.[1] To find a suitable function Ω, it is useful to

[1] In most contexts, coherent states are seen as classical and photon number states, among others, non-classical. In such contexts, researchers wish to indicate these non-classical states via negative phase-space distributions. However, this choice of a classical reference is somewhat arbitrary and historically connected to Maxwell's wave-like theory for light.

consider the problem in Fourier space. According to the convolution theorem [AWH13, p. 985 - 987][2], $P_\Omega(\alpha)$ can be written as the inverse Fourier transform of a product of the Fourier transforms of the kernel Ω and P:

$$P_\Omega(\alpha) = \int_{\mathbb{C}} \frac{d^2\beta}{\pi^2}\, e^{\beta^*\alpha - \beta\alpha^*}\, \widetilde{\Omega}(\beta)\widetilde{P}(\beta). \tag{8.2}$$

If this product $\widetilde{\Omega}(\beta)\widetilde{P}(\beta)$ (also called characteristic function) is square-integrable in Fourier space, then $P_\Omega(\alpha)$ is well-behaved and not singular in the original space. Therefore, we need a suitable $\widetilde{\Omega}(\beta)$, acting as a cut-off filter in Fourier space. Besides, in order to keep $P_\Omega(\alpha)$ non-negative for classical states, the filter $\widetilde{\Omega}(\beta)$ should have a non-negative Fourier transform. To this aim, we can use an appropriate function $\widetilde{\omega}(\beta)$ in Fourier space. It should be symmetric $\widetilde{\omega}(\beta) = \widetilde{\omega}(-\beta)$ and decay sufficiently fast so that $\widetilde{\omega}(\beta)\mathrm{e}^{u|\beta|^2}$ is square-integrable for any $u > 0$. Then the filter can be constructed as the auto-correlation of $\widetilde{\omega}(\beta)$:

$$\widetilde{\Omega}(\beta) = \frac{1}{N}\int d^2\beta' \widetilde{\omega}(\beta')\widetilde{\omega}(\beta' + \beta), \tag{8.3}$$

with a normalization constant N, so that $\widetilde{\Omega}(0) = 1$. This filter is also symmetric, its Fourier transform is always non-negative and it decays sufficiently fast so that $\widetilde{\Omega}(\beta)\mathrm{e}^{u|\beta|^2}$ is square-integrable for any $u > 0$.

There are many possible functions $\widetilde{\omega}(\beta)$ that fulfill these conditions. For example, a super-Gaussian has been used in Refs. [KVHS11, KVBZ11]. Following Ref. [KV12], we choose a rotationally invariant Heaviside function in Fourier space, giving a Bessel-type filter function in the original space. This filter is also a special case of the family of filters introduced in Ref. [KV14] and used in Ref. [KVT$^+$21, ASV$^+$15], when setting a parameter that is called q in these references to ∞. Being invariant under rotations, this filter does not perturb the phase of the original quantum state. With this choice, the constructing function $\widetilde{\omega}(\beta)$ is given by:

$$\widetilde{\omega}(\beta) = \frac{\sqrt{\pi}\varphi(R - |\beta|)}{R^2}, \tag{8.4}$$

where φ is the Heaviside step function. It has a compact support, $R \geq |\beta|$, and its autocorrelation function has a support $2R \geq |\beta|$. This ensures that coordinates with $|\beta| > 2R$ will not take part in the integration in Eq. (8.2). Thus, divergences of $\widetilde{\Omega}(\beta)\widetilde{P}(\beta)$ are suppressed and the resulting phase-space distribution is regular.

The filter parameter R has to be chosen to achieve the best results for the data at hand. Note that in the limit $R \to \infty$, we retrieve the original and often highly singular Glauber-Sudarshan distribution.

[2]Per Definition (2.26), the complex parameter $\alpha = \frac{1}{2A}(q + ip)$ decomposes into two real numbers, position q and momentum p. Hence, the same rules for the Fourier transforms apply as on $\mathbb{R}^2$.

Applying known rules for Fourier transformations[3], from this choice follows the regularizing function in the original space:

$$\Omega(\alpha) = |\omega(\alpha)|^2 = \left[\frac{J_1(2R|\alpha|)}{\sqrt{\pi}|\alpha|}\right]^2, \tag{8.5}$$

with J_n denoting the nth Bessel function of the first kind.
The procedure to sample the regularized P function $P_\Omega(\alpha)$ from data is elaborated in the next section.

Now let us shortly consider the coherence properties of P_Ω. Previously we defined quantum coherence as the summed magnitude of off-diagonal density matrix elements in the Fock basis; see Section 2.5. It can be shown that a decrease of these off-diagonal elements corresponds to a broader phase distribution of $P_\Omega(\alpha)$ [LPB$^+$]. At the extreme, an incoherent mixture of photon-number states corresponds to a completely phase-averaged P distribution. This is not changed by regularizing the P distribution with our filter. Thus, the phase variance of $P_\Omega(\alpha)$ can be used as a measure of quantum coherence. In particular, we apply the circular variance that can lie between 0 and 1, with a small value corresponding to a high amount of quantum coherence and a value one for an incoherent quantum state. Using the relation $\alpha = q + ip$, the circular variance is defined as [Fis93]

$$\begin{aligned}\mathrm{Var}(\phi) &= 1 - \int d^2\alpha\, P_\Omega(\alpha)\frac{\alpha}{|\alpha|} \\ &= 1 - \sqrt{\left(\sum_{q,p}\cos(\phi_{q,p})\, P_\Omega(q,p)\right)^2 + \left(\sum_{q,p}\sin(\phi_{q,p})\, P_\Omega(q,p)\right)^2},\end{aligned} \tag{8.6}$$

with $\phi_{q,p} = \arctan(p/q)$.

8.4 Sampling the regularized P distribution

After obtaining phase-sensitive quadrature data $\{(q_i,\varphi_i)\}_{i=1,\ldots,N}$, these allow us to sample the regularized P distribution $P_\Omega(\alpha)$ that was introduced in the last section. The basic idea is to decompose $P_\Omega(\alpha)$ into one part that depends on the measured data and another part, a so-called pattern function, that is independent of the data and can be calculated in advance to save time during data analysis. This idea has been introduced in Ref. [KVHS11] and applied e.g. in Refs. [ASV$^+$15, KVT$^+$21].

[3]From the convolution theorem follows that the Fourier transform of a product fg is given by $\int_{\mathbb{C}} \frac{d^2\beta_0}{\pi^2}\, \widetilde{f}(\beta-\beta_0)\widetilde{g}(\beta_0)$. Thus, $\widetilde{\Omega}(\beta) = \frac{1}{N}\int d^2\beta' \widetilde{\omega}(\beta')\widetilde{\omega}(\beta'+\beta)$ is the Fourier transform of $\Omega(\alpha) = |\omega(\alpha)|^2 * \pi^2/N$. From the normalization condition $\widetilde{\Omega}(0) = 1$ follows $N = 1/\pi^2$ for our filter choice. Thus, $\Omega(\alpha) = |\omega(\alpha)|^2$. Also, $\omega(\alpha)$ is the inverse Fourier transform of $\widetilde{\omega}(\beta)$, i.e. $\omega(\alpha) = \int_{\mathbb{C}} \frac{d^2\beta}{\pi^2}\, e^{\beta^*\alpha-\beta\alpha^*}\widetilde{\omega}(\beta) = \frac{\sqrt{\pi}}{\pi^2 R}\int_{\mathbb{C}} d^2\beta\, e^{\beta^*\alpha-\beta\alpha^*}\varphi(R-|\beta|) = \frac{J_1(2R|\alpha|)}{\sqrt{\pi}|\alpha|}$.

A derivation is provided in [LPB+] and also in Appendix C. According to this derivation, we can analytically write

$$P_\Omega(\alpha) = \int_{-\infty}^{\infty} dq \int_0^\pi \frac{d\varphi}{\pi} \frac{p(q,\varphi)}{\int_{\mathbb{R}} dq'\, p(q',\varphi)} \pi f_\Omega(\alpha; q; \varphi). \tag{8.7}$$

Here, $p(q,\varphi)$ is the joint probability for measuring q and φ, depending on the measured data, while $f_\Omega(\alpha; q; \varphi)$ is the pattern function. The pattern function can be written as an integral over a finite interval,

$$f_\Omega(\alpha; q; \varphi) = \frac{16R^2}{\pi^3} h(X,R), \tag{8.8}$$

where $u = s/(2R)$, $X = 2R[q/A - 2|\alpha| \cos(\varphi + \arg\alpha)]$ and

$$h(X,R) = \int_0^1 du\, u \left[\arccos(u) - u\sqrt{1-u^2}\right] \cos(uX) e^{2R^2u^2}, \tag{8.9}$$

which can be evaluated numerically for a given R and any X. Note that thanks to the regularization, the pattern function is not divergent in contrast to other phase-space distributions.

In particular, a sufficiently dense grid of X parameters and corresponding pattern functions for a given R can be stored and used later. Hereby, the X parameter and thus the pattern function depend on q, φ, and α. The complex number $\alpha = q_{\text{new}} + ip_{\text{new}}$ is the new phase-space coordinate over which $P_\Omega(\alpha)$ is displayed. The variables q and φ can be defined as a grid of Ξ position intervals and Φ phase intervals against which the measured values (q_i,φ_i) are compared, as follows. For clarity, we will call these grid variables q_{grid} and φ_{grid} to discern them from the measured values.

In the next step, we replace the joint probability $p(q_{\text{grid}},\varphi_{\text{grid}})$ by statistical frequencies. Therefore, we suppose N quadratures q_i with phases φ_i were measured, i.e., the data set reads $\{(q_i,\varphi_i)\}_{i=1,\ldots,N}$. We define $N(q_{\text{grid}},\varphi_{\text{grid}})$ as the number of data points (q_i,φ_i) which are closest—according to the predefined grid of Ξ position intervals and Φ phase intervals—to $(q_{\text{grid}},\varphi_{\text{grid}})$. Then the above integral can be approximated through the weighted average

$$\boxed{P_\Omega(\alpha) \approx \frac{1}{\Phi} \sum_{q_{\text{grid}},\varphi_{\text{grid}}} \frac{N(q_{\text{grid}},\varphi_{\text{grid}})}{\sum_{q'_{\text{grid}}} N(q'_{\text{grid}},\varphi_{\text{grid}})} \pi f_\Omega(\alpha; q_{\text{grid}}; \varphi_{\text{grid}}) = \overline{P_\Omega(\alpha)}.} \tag{8.10}$$

Thus, the measured data only influence the weights $N(q_{\text{grid}},\varphi_{\text{grid}})$.

The second-order moment $\overline{P_\Omega(\alpha)^2}$ can be calculated similarly, using $[\pi f_\Omega(\alpha; q; \varphi)]^2$ in the above expression. This gives the uncertainty of the reconstructed phase-space distribution

$$\sigma[P_\Omega(\alpha)] = \sqrt{\frac{\overline{P_\Omega(\alpha)^2} - \overline{P_\Omega(\alpha)}^2}{N-1}}. \tag{8.11}$$

In this work, I chose the values shown in Table 8.1 for the predefined grid of Ξ quadrature intervals q_{grid}, Φ phase intervals φ_{grid}, and for the resulting new phase-space coordinates $\alpha = q_{\mathrm{new}} + ip_{\mathrm{new}}$ on which the $P_\Omega(\alpha)$ function is displayed. All grids are equally spaced. The step sizes are chosen as a compromise between the smoothness of the regularized P function and a reasonable computation time.

	Minimum	Maximum	Step size
q_{grid}	-20	20	1
φ_{grid}	0	2π	0.1
q_{new},p_{new}	-20	20	0.25

Table 8.1: Parameters of the predefined grids for the sampling of the regularized P function. The grid for comparison with the measured data is given by q_{grid} and φ_{grid}. The new phase-space coordinates for displaying $P_\Omega(\alpha)$ are given by q_{new},p_{new}.

8.5 Choice of filter width parameter

The regularized P function we introduced depends on a filter parameter R. For $R \to \infty$ (wide filter), we approach the original Glauber-Sudarshan distribution, but also the errors σ are large. Conversely, $R \to 0$ (narrow filter) does not result in a sufficient estimation of the phase-space distribution. Thus, we have to find the best intermediate R value empirically.

A comparison of P_Ω for different R values is shown in Fig. 8.4. In the top row, three exemplary P_Ω distributions are depicted. Obviously, the small filter parameter $R = 0.2$ leads to a very broad P_Ω function, where important features are smoothed away. On the other hand, for $R = 1$, the function is sharper but has numerical artifacts and an increased uncertainty. In between, $R = 0.7$ yields a smooth-looking function with well-preserved features without many artifacts. The lower plot compares properties of P_Ω like the width and the maximum error depending on R. Apparently, the range $0.5 \leq R \leq 1$ provides a low error and an unchanging width. Consequently, I chose $R = 0.7$ as the best trade-off value.

8.6 Results

8.6.1 Preliminary characterization of excitation power dependence

Before presenting the measured P_Ω functions, we first discuss results from Husimi function measurements for different excitation powers to characterize the system. Figure 8.5 shows the coherent and thermal photon numbers, $g^{(2)}(0)$ and quantum coherence derived from fitting Husimi functions for varying excitation powers. The upper row depicts results for 0° linear polarization and the lower row shows results for 90° polarization.

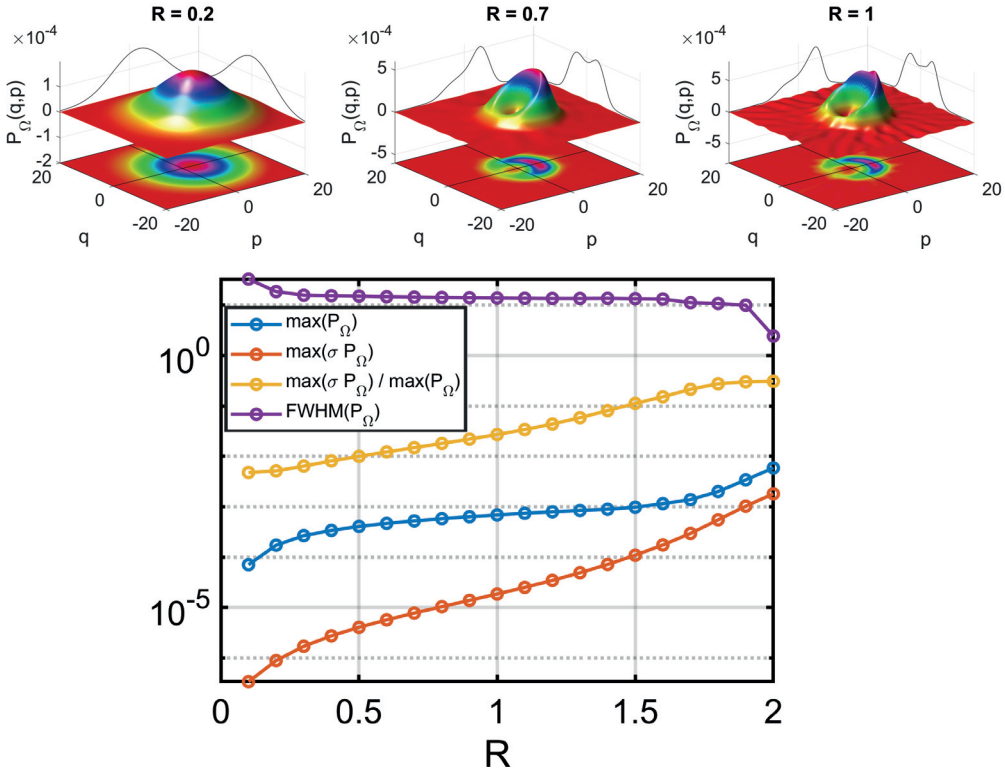

Figure 8.4: Comparison of P_Ω for different filter parameters R. The used dataset was acquired for $P_{\text{exc}} = 400$ mW ($P_{\text{exc}} = 1.7\ P_{\text{thr}}$) and a time delay $\tau = 1214$ ps. With increasing R, P_Ω becomes better defined but also more disturbed by artifacts. The value $R = 0.7$ yields a good compromise between well-defined features and reasonable errors.

For $P > 240\,\text{mW}$, the coherent photon number in the dominant 0° polarization increases rapidly, $g^{(2)}(0)$ drops and quantum coherence builds up. This power is higher than the one we identified in Section 7.5.2, probably due to slight changes of the sample position and environmental conditions. However, similar to our discussion in 7.5.2, we suppose that at this power, condensation occurs in the mode that is measured by the LO. Therefore, we define this power as the threshold power for our following discussions. Note that this is not the usual definition of threshold power based on a nonlinear increase of the total emitted intensity, but it is meaningful for the specific mode filtered by the LO. Also, this threshold power can be compared to the one in the numerical simulation.

Furthermore, for the 90° polarization, we observe an increase of coherent photon number and quantum coherence in a very small range of powers, 239 - 270 mW or 1 - 1.1 P_{thr}, implying mode competition between the two polarizations.

Keeping this power dependence in mind, we now proceed with the measured P_Ω functions.

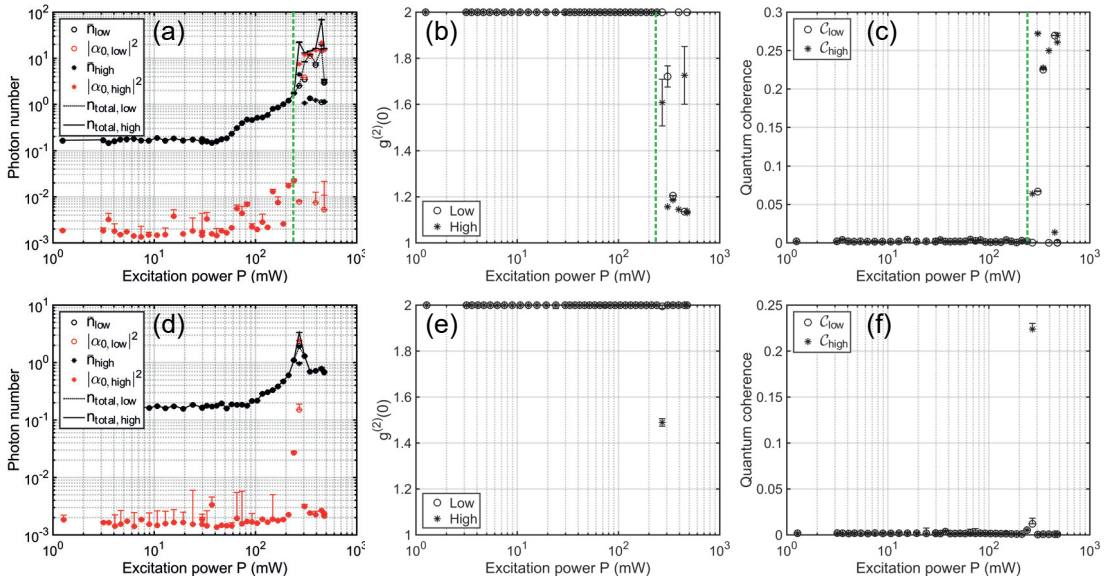

Figure 8.5: Results from fitting Husimi functions for varying excitation power. Upper row: 0° linear polarization of the emission. Lower row: 90° polarization. (a),(d): Coherent, thermal and total photon numbers. (b),(e): Photon correlation $g^{(2)}(0)$. (c),(f): Quantum coherence. Open and closed symbols correspond to the low and high state, respectively, when the emission is bistable. The green dashed lines in (a)–(c) indicate the threshold for a nonlinear increase of the coherent photon number and the build-up of quantum coherence in the 0° polarization.

8.6.2 Measured P_Ω functions for varying delay time

Let us now examine the P_Ω functions of the polariton emission that were measured for different delay times between target and postselection channels and for different excitation powers.

In Fig. 8.6, in the upper row, three examples of P_Ω for different delay times τ can be seen. These examples were measured at the highest excitation power $P_{\mathrm{exc}} = 400\,\mathrm{mW} = 1.7P_{\mathrm{thr}}$; the postselected phase-space region is given by a radius $s = 9.9$ and a width $w = 0.57$. For the time closest to zero, $\tau = -6$ ps, the distribution is narrow and symmetrical. With increasing time delay, P_Ω dephases, resulting in a broadening of the angular distribution. Besides, also the mean amplitude relaxes towards the steady-state value. To resolve both effects, we calculate the circular phase variance $\mathrm{Var}(\phi)$ via Eq. (8.6) and the mean amplitude via $\langle|\alpha|\rangle = \int d^2\alpha\, P_\Omega(\alpha)|\alpha| = \sum_{q,p} P_\Omega(q,p)\sqrt{q^2+p^2}$, where q,p denote the new phase-space coordinates q_{new},p_{new} for simplicity.
The temporal evolution of these mean values is plotted in Fig. 8.6(a) and (b) for $P_{\mathrm{exc}} = 1.7\ P_{\mathrm{thr}}$ for different postselected radii s while the width w is kept at 0.57. The inset in (a) shows the corresponding steady-state Husimi function for this excitation power, whereby the displacement of the ring indicates a significant amount of quantum coherence, $\mathcal{C} = 0.196 \pm 0.002$. The circular phase variance (a) has its minimum around $\tau = 0$, being 0.14 for the highest postselection radius. This minimum increases for

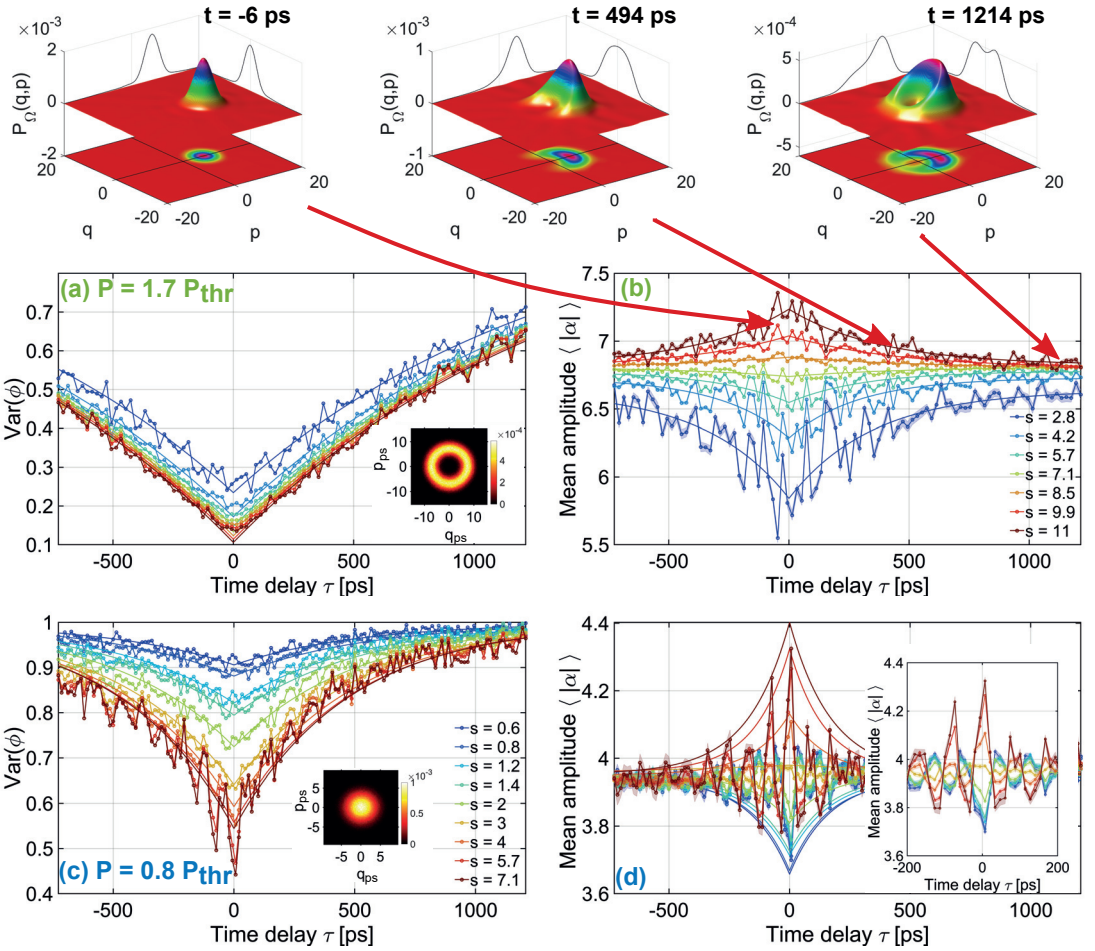

Figure 8.6: Results from measuring the P_Ω function for a series of delay times. Top row: Three exemplary P_Ω functions for $P_{\mathrm{exc}} = 400\,\mathrm{mW} = 1.7\ P_{\mathrm{thr}}$ for a postselected region with amplitude $s = 9.9$ and width $w = 0.57$, at time delays $\tau = -6$ ps (left), $\tau = 494$ ps (middle), and $\tau = 1214$ ps (right). The middle and lower rows show average values versus delay time for $P_{\mathrm{exc}} = 1.7\ P_{\mathrm{thr}}$ and $P_{\mathrm{exc}} = 0.8\ P_{\mathrm{thr}}$, respectively. (a,c) display the circular phase variance $\mathrm{Var}(\phi)$ and (b,d) the mean amplitude $\langle|\alpha|\rangle$ for different postselected amplitudes s. The width w is always 0.57 for the middle row and 0.1 for the lower row except for the two highest radii s, where it is also 0.57. The shaded area around the measured data corresponds to a one standard-deviation error margin, derived from the uncertainty σP. The lines with the same color as the data depict exponential fits. Insets in (a) and (c) present the corresponding Husimi functions. An inset in (d) displays a zoom around zero delay, revealing an oscillation of the mean amplitude.

smaller s due to the fundamental phase-photon number uncertainty relation, as elaborated in Subsection 8.6.3.

For growing time delay, $\mathrm{Var}(\phi)$ increases but does not reach the value 1 — which would indicate a uniform distribution of phases — even for the highest delay $\tau = 1214$ ps. On the other hand, the mean amplitude $\langle|\alpha|\rangle$ shown in (b) decays towards the steady-state value within the measured time interval. Around zero delay, $\langle|\alpha|\rangle$ is higher or smaller than the steady-state value when s is also higher or smaller than the mean amplitude in

the postselection channels, corresponding to a higher or smaller momentary intensity, respectively.
In contrast, Fig. 8.6 (c) and (d) show the results for the lowest excitation power $P_{\mathrm{exc}} = 200\,\mathrm{mW} = 0.8\ P_{\mathrm{thr}}$. The Husimi function does not show a displacement but is Gaussian shaped, corresponding to a small quantum coherence $\mathcal{C} = 0.0563 \pm 0.0004$. For this low excitation power, the phase variance increases faster and reaches almost 1 within the measured time interval, indicating an equal distribution of phases and a complete loss of quantum coherence.
Furthermore, the envelope of the mean amplitude $\langle|\alpha|\rangle$ rapidly decays towards the steady-state value; however, a zoom reveals an oscillation with a frequency of ca. 12.5 GHz. This oscillation appears as well for $P_{\mathrm{exc}} = 1\ P_{\mathrm{thr}}$ (not shown), but not for higher powers. In this range of powers, mode competition might occur between the two linear polarization components, as observed in Subsection 8.6.1. According to a simulation in Ref. [Sig20], a bistable regime of two cross-linear polarizations in a non-resonantly excited polariton condensate might indeed occur and cause an oscillatory behavior of the condensate pseudospin components. Furthermore, the observed frequency corresponds to an energy difference of 50 µeV, which has a similar magnitude as energy splittings between the polarizations found in the literature [KAD$^+$07, GST$^+$21]; thus, the oscillation might also be caused by quantum beats if the two polarizations are not completely separated by the Glan Thompson prism at this power. Another explanation might be modulations of the spatial density of the polariton condensate, e.g. breathing modes, that can lie in this frequency range as well [EPW$^+$21]. Finding the cause for these oscillations, however, goes beyond this work but might be pursued in further research.

8.6.3 Remarks on phase-photon number uncertainty

Before we further quantify the decay times, let us briefly consider how the minimum phase variance is connected to the selected intensity. As we have seen, $\mathrm{Var}(\phi)$ around $\tau = 0$ increases for decreasing selected radii s. With a smaller selected radius, we select a state with a lower photon number. Photon number and phase uncertainty are connected by the fundamental photon number-phase uncertainty relation [SBRF93]

$$\Delta\phi\Delta n \geq \frac{1}{2}|\langle[\hat{\phi},\hat{n}]\rangle|. \tag{8.12}$$

Note that for coherent states, $\Delta n = \sqrt{n}$. Thus, selecting a coherent state with a lower photon number leads to a higher phase uncertainty. Coherent states are the ideal limiting case for our postselected states since we do not expect squeezed states for our experiment. Hence, the phase variance of a coherent state sets a fundamental limit for how low the phase variance of the measured state can become. We test this assumption

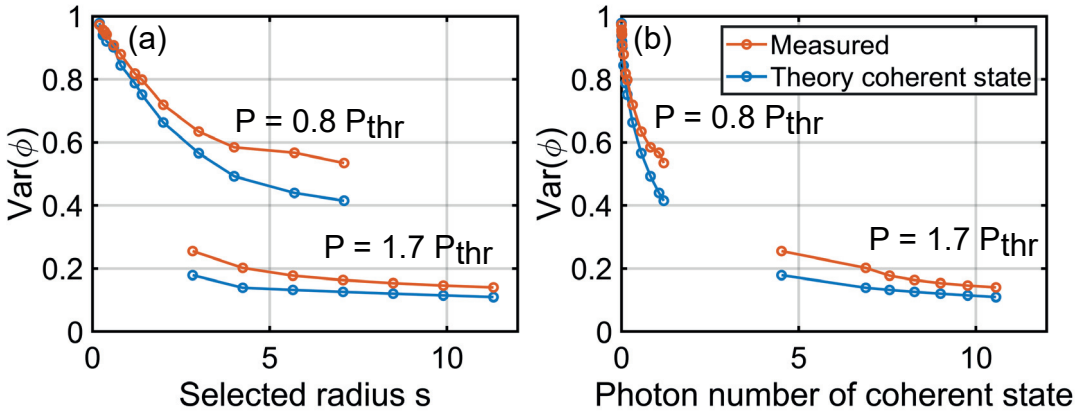

Figure 8.7: (a) Circular phase variance $\mathrm{Var}(\phi)$ versus the selected radius s for $P_{\mathrm{exc}} = 0.8\ P_{\mathrm{thr}}$ and $P_{\mathrm{exc}} = 1.7\ P_{\mathrm{thr}}$. Red: $\mathrm{Var}(\phi)$ of the measured P_Ω around $\tau = 0$. Blue: $\mathrm{Var}(\phi)$ of a theoretical coherent state with the same offset q_0. (b) Measured (red) and theoretical (blue) circular phase variance $\mathrm{Var}(\phi)$ for both powers versus the photon number of the corresponding coherent state.

by comparing the measured phase variance to the one of an ideal coherent state with the same amplitude as the postselected state. In particular, we identify the offset q_0 of the measured P_Ω function, calculate the theoretical P_Ω function of a coherent state having the same offset[4], and determine the coherent state's circular phase variance. The result is depicted in Fig. 8.7. Clearly, for both states, the phase variance decreases for increasing photon numbers, following the same trend. This phase-photon number uncertainty relation has also been observed for coherent states in Ref. [SBRF93].
Yet, our measured phase variance slightly exceeds the theoretical limit because of the finite width of the selected phase-space regions, a low amount of data in some of these regions, and experimental imperfections that increase phase noise. Furthermore, the variance of the postselected states is also theoretically expected to exceed the coherent limit and to depend on the photon numbers in the proxy and target channels [The18, p. 74, p. 82].

8.6.4 Decay times

Now let us analyze the temporal decay in detail. To this aim, we fit the temporal dependence of $\mathrm{Var}(\phi)$ and $\langle|\alpha|\rangle$ with a suitable function and extract a decay time. For finding the best matching function, we compare several functions that are likely to apply to our case, namely an exponential, a Gaussian, a power-law, and a power-law that starts at variable time. These functions are shown in Figure 8.8(a) for the

[4]The Glauber-Sudarshan P distribution of the coherent state is a delta distribution $\delta(\alpha - \alpha_0)$. Thus, the regularized P function of the coherent state according to Eq. (8.1) and (8.5) is given by $P_\Omega(\alpha) = \Omega(\alpha - \alpha_0) = \left[\frac{J_1(2R|\alpha-\alpha_0|)}{\sqrt{\pi}|\alpha-\alpha_0|}\right]^2$.

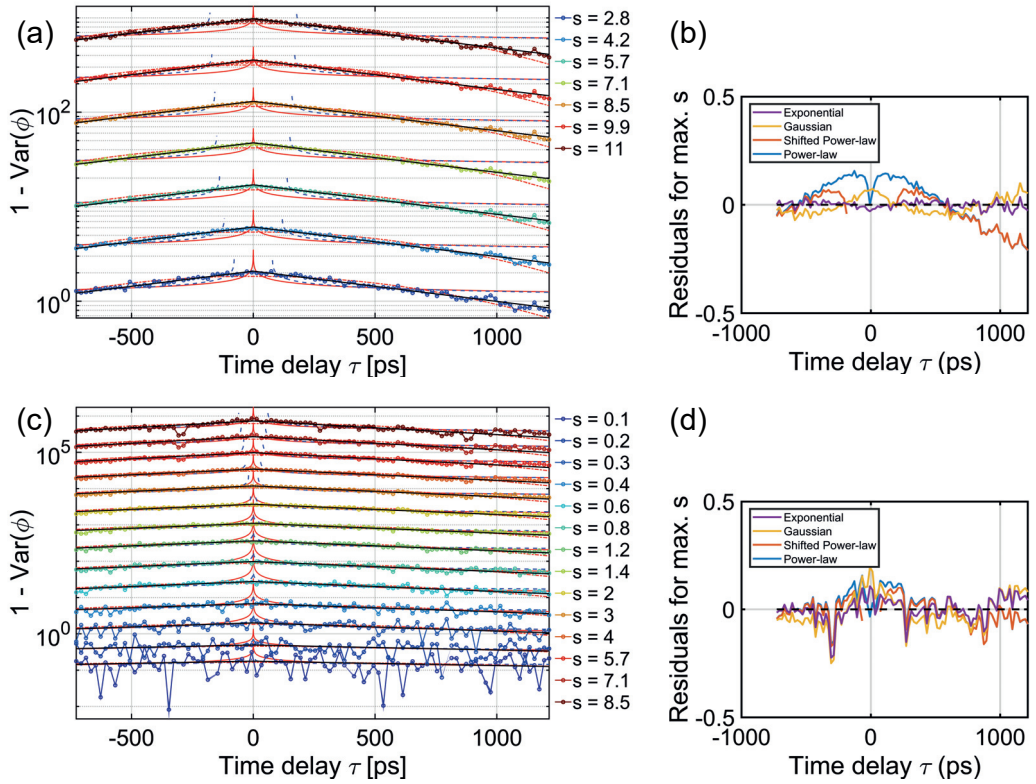

Figure 8.8: Comparison of different fit functions for the temporal dependence of $\mathrm{Var}(\phi)$. Plots (a) and (b): $P_{\mathrm{exc}} = 1.7\ P_{\mathrm{thr}}$. (a) Temporal decay of $1 - \mathrm{Var}(\phi)$ for different selected radii s, plotted semilogarithmically and scaled. The width w of the selected phase-space region is 0.57. Solid red line: power-law fit function; dashed blue line: temporally shifted power law; dotted red line: Gaussian fit; solid black line: exponential fit. (b) Residuals (i.e., data minus fit) for the highest postselection radius. Plots (c) and (d): $P_{\mathrm{exc}} = 1\ P_{\mathrm{thr}}$. The width w is 0.1, except for the three highest radii s, where $w = 0.57$.

temporal decay of $1 - \mathrm{Var}(\phi)$ at $P_{\mathrm{exc}} = 1.7\ P_{\mathrm{thr}}$. We chose a semilogarithmic scale so that different functions are easily distinguishable by their shape. Furthermore, we multiplied the results for increasing postselection radii s by an exponentially increasing factor in order to render all of them equally visible.

The residual difference between the data and these fit functions for the highest radius s is displayed in Fig. 8.8(b). Clearly, the exponential function matches best to the data. The same holds true for all other excitation powers (not shown), except $P_{\mathrm{exc}} = 1\ P_{\mathrm{thr}}$, which is depicted in Fig. 8.8(c) and (d).
At this threshold power for the build-up of quantum coherence, we observe a flatter decay of $1 - \mathrm{Var}(\phi)$, especially for larger time delays and higher postselected radii s. Thus, a power-law decay also might be an option. Such a power-law decay was suggested by theorists in Ref. [SKL07] for large systems and intermediate times. A power-law decay was also experimentally observed for a high-quality sample with a spatially extended condensate [CBD+18], where it was ascribed to a Berezinskii–Kosterlitz–

Thouless phase transition. This kind of topological order requires the formation of vortex-antivortex pairs, which might be less disturbed by interactions at threshold power than at higher powers.
Nevertheless, an exponential fit might still be valid as well since both fit functions yield comparable residuals. Also, for the high time delays and high postselected radii $s \geq 3$, the data points exhibit stronger noise, so they do not allow very reliable fits. Therefore, the decision between the different fit functions is not conclusive for $P_{\mathrm{exc}} = 1\ P_{\mathrm{thr}}$.
Thus, for comparability, we use an exponential fit to determine the decay times of $\mathrm{Var}(\phi)$ and of $\langle|\alpha|\rangle$ for all excitation powers according to

$$\langle|\alpha|\rangle,\mathrm{Var}(\phi) = a\ \exp\left(-\frac{\tau}{\tau_c}\right) + s, \tag{8.13}$$

yielding a decay time τ_c for each. For $\mathrm{Var}(\phi)$, the saturation value s was kept fixed at 1. These exponential fits are depicted in Fig. 8.6 as lines with the same color as the data points. The extracted decay time is plotted in Fig. 8.9(a) for $\mathrm{Var}(\phi)$ and in Fig. 8.9(b) for $\langle|\alpha|\rangle$ versus the postselected radius s for different excitation powers.

In Fig. 8.9(a), we observe a slight trend for the decay time of $\mathrm{Var}(\phi)$ to decrease with increasing s for lower excitation powers and vice versa for higher excitation powers. However, except for $1\ P_{\mathrm{thr}}$, this trend is not very significant, and for $1\ P_{\mathrm{thr}}$, the fits are not that reliable as discussed above. Therefore, we can not decide conclusively whether the selected radius s has an impact on the decay time of the phase variance.
Furthermore, for $\langle|\alpha|\rangle$, the decay time does not show a significant dependence on s.
In the following, we average the decay times over all postselected radii s for each excitation power and plot them in Fig. 8.9(c). Clearly, the amplitude decays significantly faster than the phase variance. For both quantities, in general, the decay times increase with excitation power.
However, for the amplitude, the decay time drops for the highest power while the decay time of $\mathrm{Var}(\phi)$ stays on a plateau. Here, heating might have an influence; but also an effect might take place that was described in Ref. [WE09]. This theoretical work found that for high excitation power, polariton number fluctuations should decay fast, leading to a slower decay of $g^{(1)}(\tau)$ since $g^{(1)}(\tau)$ is diminished by number fluctuations. If the polariton number fluctuations are connected to changes of the mean amplitude and $g^{(1)}(\tau)$ is in somewhat a measure of phase coherence — albeit these quantities are not equal —, then a faster relaxation of the amplitude might indeed cause a longer-lasting phase coherence.
Regarding the phase variance, the decay time is exceptionally long, between 520 and 1390 ps. This is particularly the case for $P_{\mathrm{exc}} = 1\ P_{\mathrm{thr}}$. At this threshold power, the quantum coherence is less affected than at higher powers by heating and interaction with the reservoir as well as polariton-polariton interactions.

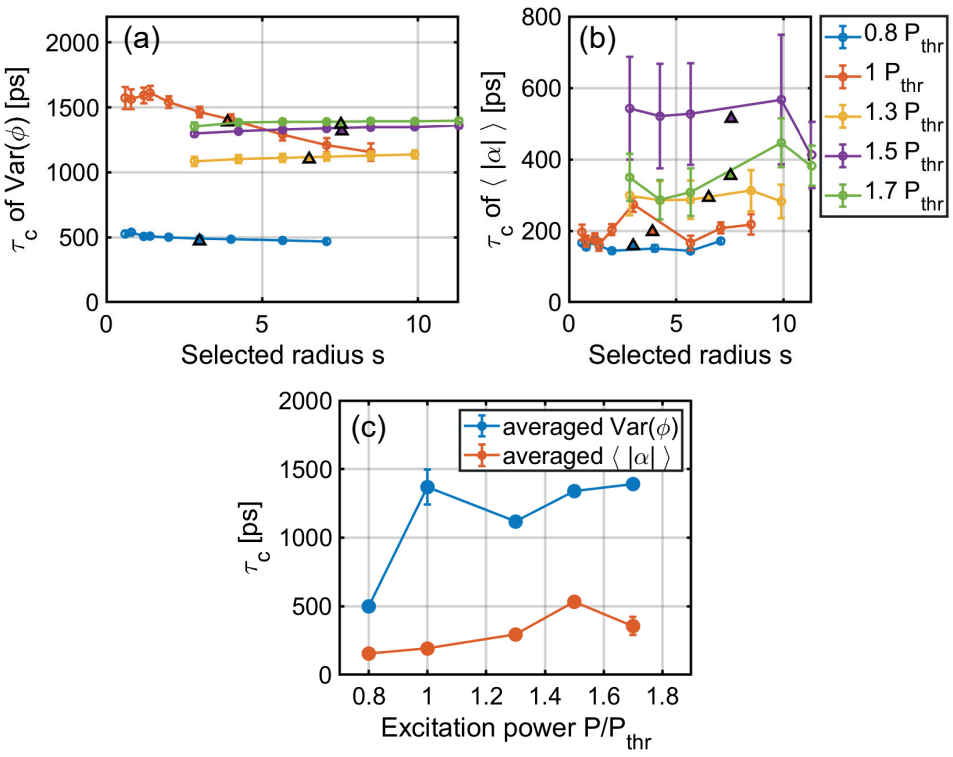

Figure 8.9: Fitted decay time τ_c of (a) the circular phase variance Var(ϕ) and (b) the mean amplitude $\langle|\alpha|\rangle$ versus the postselected radius s for different excitation powers. Black-rimmed triangles indicate the mean radius from the Husimi distribution, i.e. the stationary state. For $\langle|\alpha|\rangle$, those s were omitted that lie too close to the mean radius, since here the flat curve shape of $\langle|\alpha|\rangle(\tau)$ causes unreliable fits. (c) Decay time τ_c, averaged over the postselected radii s, versus excitation power. When calculating the average, the decay time for each s has been weighted with the corresponding amount of postselected data points.

Such long coherence times have been observed only in a few previous studies on polariton condensates. As discussed in Section 3.5, coherence times on the order of $100 - 1000$ ps were achieved by suitable experimental conditions: noisefree single-mode excitation [LKW$^+$08], samples designed for single-mode emission [KZW$^+$16], patterned pump shapes for diminishing interactions with the reservoir or large pump spots [OTP$^+$21, APA$^+$19, BZS$^+$22]. Nevertheless, most of these studies found a Gaussian shape of $g^{(1)}(\tau)$, indicating inhomogeneous broadening of the signal. Furthermore, these results are not directly comparable to ours since they measured different properties than the quantum coherence, i.e. $g^{(1)}(\tau)$ and $g^{(2)}(\tau)$.

The long-lasting quantum coherence we observe might be explained on the one hand by exciting with a single-mode laser with a relatively large beam diameter, and, on the other hand, by our homodyne detection method that only measures one mode filtered by the LO. This mode selectivity allows us to track the dynamics of the selected mode separately and only measure its intrinsic decay time instead of the faster decay due to inhomogeneous broadening when measuring several modes.

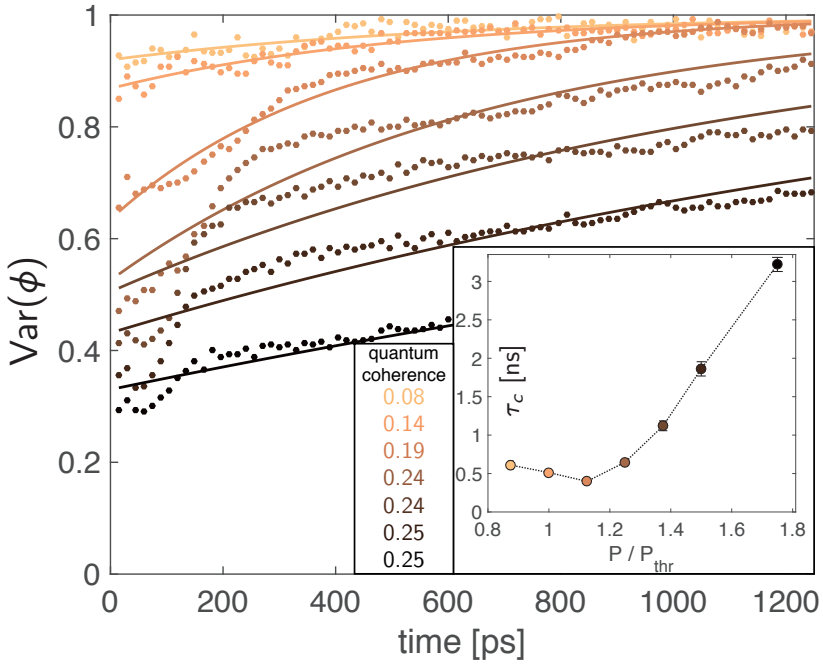

Figure 8.10: Results from a numerical simulation by the Paderborn group. Main plot: Circular variance Var(ϕ) of P_Ω versus time for several excitation powers. Inset: Decay time extracted from an exponential fit versus excitation power. The quantum coherence of the steady state is indicated for each excitation power.

8.7 Comparison to numerical simulations

In order to assess the decay times from the theoretical side, a numerical simulation was carried out by Matthias Pukrop and Franziska Barkhausen in the group of Stefan Schumacher at Paderborn University. They used the same stochastic Gross-Pitaevskii model, based on the truncated Wigner approximation, as in Section 7.6. The system is initialized as a displaced thermal state, where the mean displacement and standard deviation are taken from the steady-state values for the mean polariton number and the quantum coherence. Then, the system is evolved in time with a fourth-order stochastic Runge-Kutta algorithm on a finite two-dimensional grid in real space. To be comparable to the experimental results, the Wigner function is converted to the P_Ω function by a convolution-deconvolution approach [LPB$^+$] before evaluating the phase variance.

The results are shown in Fig. 8.10. The main plot displays Var(ϕ) versus time for several excitation powers while the inset shows the fitted decay time versus power. Compared to the experiment, the decay time has a similar order of magnitude, lying between 0.5 and 3 ns. Especially for intermediate powers, the times are similar to the ones observed in the experiment. Thus, there must be similar decoherence mechanisms present for intermediate powers. From the simulation, we can identify the source of decoherence as the nonlinear part of the effective potential, which is connected to interactions of the polaritons with each other and the reservoir, in combination with

density fluctuations that lead to frequency fluctuations.
In the simulation, these density fluctuations are especially prominent near the threshold power, leading to a rather short coherence time. This is different from the experiment, where the coherence time is particularly high at threshold power. From the decay of the mean amplitude in the experiment, we can assume that density fluctuations decay fast around threshold and also for the highest power, so they do not affect the phase coherence as much.
A second difference in the simulation is that the decay time unboundedly increases with power while in the experiment, it rather reaches a plateau. This shows that at higher powers, there are decoherence mechanisms in the experiment that are not taken into account in the simulation, namely heating of the sample and higher-order scattering processes.
All in all, the simulation is sufficiently similar to the experiment to yield decay times of the same order of magnitude, but the role of particular decoherence mechanisms might be investigated in the future.
Nevertheless, from the simulation we can learn the impact of intrinsic properties of the sample on decoherence. In particular, τ_c increases with decreasing polariton interaction strength g_c and with increasing condensate-reservoir interaction g_r. Especially the condensate-reservoir interaction g_r heavily influences the coherence time through the nonlinear part of the polariton's effective potential landscape while not having much influence on the steady-state amount of quantum coherence, which is why here it was chosen much smaller than in the previous chapter. This effect that a higher g_r leads to longer coherence times is rather unintuitive. The reason is the so-called hole-burning effect [EGB+18, WC07], where the condensate-reservoir interaction causes a depletion of the reservoir when the polariton density increases. This depletion of the reservoir, in turn, enables longer coherence times because the reservoir is a source of density fluctuations. Thus, a smaller reservoir density or a spatial separation of reservoir and condensate leads to longer-lasting coherence.

8.8 Conclusion

In this penultimate chapter, I investigated the temporal decay of quantum coherence in a polariton condensate. To this aim, I employed multi-channel homodyne detection in order to reconstruct the state of light of the polariton condensate, using a modern regularized P function approach. While the homodyne detection method allowed me to selectively filter on one mode for measurement, postselection after data acquisition enabled me to analyze the dynamics of the state depending on the initial intensity. I thereby observed long decay times of the circular variance — being a measure of quantum coherence — on the order of 1 ns, which was confirmed by a numerical simulation. This result is good news for the usability of polariton condensates in quantum tech-

nologies. Furthermore, it shows that other modes in the signal are not detrimental if they can be filtered out by homodyning, relieving constraints that were put on sample design to enable only single-mode operation.
All in all, this experiment delivered novel findings on polariton condensates that could hardly have been obtained in another way. The results showed that this system carries enough resources for quantum information processing while also providing insights into the physics of complex dynamics in semiconductor systems.
As an outlook, the coherence time might be improved by using different excitation geometries or vortex modes. Moreover, the multi-channel detection method might be employed to investigate the interplay between different modes of the condensate. To this aim, one might measure one mode, e.g. with a given polarization, in the postselection channels while detecting another mode, e.g. with orthogonal polarization, in the target channel, providing more insights into the dynamics of mode competition. Besides polariton condensates, also other optical systems with steady-state fluctuations might be investigated via multi-channel homodyne detection, e.g. lasers with multiple modes having gain competition [SSK$^+$19, LHA$^+$13] or quantum dots showing fluorescence intermittency ("blinking") [EN16].

Chapter 9

Conclusion and Outlook

In this work, I presented the advancement and application of homodyne detection (HD) to semiconductor exciton-polariton emission in order to measure quantum properties of the system. I demonstrated that HD is a useful tool not only for quantum optics but also for semiconductor spectroscopy, furthering the connection between these mostly separated fields on the road to quantum hybrid systems for future technologies. Specifically, I showed which information can be gained by HD without a fixed phase reference, depending on the number of detection channels. These findings are summed up in the following.

In Chapter 6, I presented time-resolved measurements of the photon number and the second-order correlation function $g^{(2)}(0,t)$ via one-channel HD. My studies showed that the slower external noise can be separated from the faster intrinsic photon-number fluctuations by using a sufficiently high averaging frequency for calculating the $g^{(2)}$ values.
Thus, time-resolved HD is a suitable tool for investigating the photon statistics of a light source in spite of external noise, which is especially an issue when noise itself is an important figure of merit, e.g. for the detection of squeezed light [BBA$^+$14, AAF$^+$17].

In Chapter 7, I employed two-channel HD in order to measure the phase-averaged Husimi function of the polariton emission. The Husimi function was found in good agreement with the model of a displaced thermal state, undergoing a transition from a mostly thermal to a mostly coherent state with increasing excitation power.
At a sweet spot of excitation power, the system showed a significant amount of quantum coherence, $\mathcal{C} \approx 0.2$, which was confirmed by a numerical simulation performed by Matthias Pukrop at Paderborn University. This non-zero amount of quantum coherence proves the presence of quantum superpositions of Fock states in the polariton system. Since these superpositions provide a resource for quantum protocols and might be transformed into entanglement, our result indicates the potential usefulness of po-

laritons for quantum information processing.
Moreover, I found evidence of mode competition between two cross-linearly polarizations, leading to bistable behavior in a certain power range.

In Chapter 8, I investigated the temporal decay of quantum coherence in a polariton condensate via three-channel HD. I employed the nonstationary optical homodyne tomography (OHT) technique developed by Johannes Thewes, Marc Aßmann and myself, and applied an algorithm proposed by Jan Sperling to the measured data in order to reconstruct the recently developed phase-space function P_Ω. Sampling P_Ω depending on postselected initial conditions and on delay time rendered it possible to track the dynamics of different phase-space regions and to extract a nanosecond decay time of quantum coherence, which is on the upper edge of the range of coherence times that were previously observed for polariton condensates. A similar decay time was reproduced by a numerical simulation from Matthias Pukrop and Franziska Barkhausen at Paderborn University.
Regarding quantum applications, this decay time is at the low end for different types of quantum-information platforms and too short to serve as a storage medium, for which spin ensembles are rather suited [KBK$^+$15]; but this time might be sufficient for a processing unit, being comparable to the coherence time provided by a semiconductor quantum dot hybrid qubit [KSS$^+$14] and semiconductor charge qubits [PPLG10, UKDD22]. Of course, the relevant figure of merit is not only the coherence time itself but the ratio between manipulation and coherence time depending on the used quantum protocol, which will be determined by future implementations.
Furthermore, at powers close to the threshold for the onset of quantum coherence, I observed a temporal modulation of the mean amplitude of P_Ω. This modulation might be connected to the aforementioned mode competition but also to density oscillations of the condensate and leaves room for further investigations. At this point, this observation demonstrates the ability of OHT to resolve the dynamics of the system.

All in all, I showed the capability of HD to characterize quantum properties and dynamics of a light-emitting semiconductor system. By postselecting specific parts of the phase space, spontaneous processes can be investigated that are hard to resolve with other detection schemes. This ability to carry out time- and intensity-resolved quantum state tomography opens new possibilities to explore quantum dynamics in extremely fine details. Here, it is worthwhile to note that HD allows one to selectively filter on one mode of the light field, removing the influence of other modes from the measurement. This selectivity might be expanded further in the future, tuning the LO in the different channels to different polarization modes or even OAM (orbital angular momentum) modes in order to investigate their interplay. For example, the observed mode competition might be investigated in more detail by measuring different polar-

ization modes in the proxy and target channels.

Regarding the future use of polariton condensates, the value of quantum coherence still leaves room for improvement since we only reached 20% of what is possible. To optimize this value, one might employ different pump profiles — in particular, narrow ring-shaped ones — or create polariton vortices [Puk22], which might also elongate the coherence time. Furthermore, the polariton optical parametric oscillator (OPO) [BSS$^+$00, WSF$^+$21] might be investigated with our method, where one tunes the excitation beam to the inflection point of the LP dispersion in order to stimulatedly scatter two polaritons to the ground state and to a higher state, which is expected to induce quadrature squeezing [RKL$^+$10].

However, multi-channel HD is not limited to polaritons but may be applied to other light-emitting systems in order to investigate quantum properties and spontaneous dynamical events that can not be measured by conventional methods. This might be fruitful among others for systems exhibiting bistability, e.g. lasers with mode competition [SSK$^+$19, LHA$^+$13], and quantum dots showing fluorescence intermittency ("blinking") [EN16]. Furthermore, one might expand the setup to more channels, giving access to more complex phase-space correlations.
Finally, a complete quantum process tomography [LKK$^+$08, KK06] might be performed, where one maps possible input parameters to the output of the system in order to realize a full quantum description of processes within the system.

In conclusion, my studies showed the applicability of optical homodyne tomography for semiconductor spectroscopy and the general potential for quantum coherent operation of polariton condensates for quantum information processing. I envisage this work to be a building block for fundamental research on semiconductor quantum optics and for the development of hybrid quantum systems.

Bibliography

[AAB+15] A. F. Adiyatullin, M. D. Anderson, P. V. Busi, H. Abbaspour, R. André, M. T. Portella-Oberli, and B. Deveaud. Temporally resolved second-order photon correlations of exciton-polariton Bose-Einstein condensate formation. *Applied Physics Letters* 107(22), 221107 (2015). 10.1063/1.4936889.

[AAF+17] A. F. Adiyatullin, M. D. Anderson, H. Flayac, M. T. Portella-Oberli, F. Jabeen, C. Ouellet-Plamondon, G. C. Sallen, and B. Deveaud. Periodic squeezing in a polariton Josephson junction. *Nature Communications* 8(1), 1329 (2017). 10.1038/s41467-017-01331-8.

[AB15] M. Aßmann and M. Bayer. Stochastic pumping of a polariton fluid. *Physical Review A* 91(5), 053835 (2015). 10.1103/PhysRevA.91.053835.

[ABB+21] D. Awschalom, K. K. Berggren, H. Bernien, S. Bhave, L. D. Carr, P. Davids, S. E. Economou, D. Englund, A. Faraon, M. Fejer, S. Guha, M. V. Gustafsson, E. Hu, L. Jiang, J. Kim, B. Korzh, P. Kumar, P. G. Kwiat, M. Lončar, M. D. Lukin, D. A. Miller, C. Monroe, S. W. Nam, P. Narang, J. S. Orcutt, M. G. Raymer, A. H. Safavi-Naeini, M. Spiropulu, K. Srinivasan, S. Sun, J. Vučković, E. Waks, R. Walsworth, A. M. Weiner, and Z. Zhang. Development of Quantum Interconnects (QuICs) for Next-Generation Information Technologies. *PRX Quantum* 2(1), 017002 (2021). 10.1103/PRXQuantum.2.017002.

[ACY83] G. L. Abbas, V. W. S. Chan, and T. K. Yee. Local-oscillator excess-noise suppression for homodyne and heterodyne detection. *Optics Letters* 8(8), 419 (1983). 10.1364/OL.8.000419.

[AFP09] G. Auletta, M. Fortunato, and G. Parisi. *Quantum Mechanics*. Cambridge University Press (2009). 10.1017/CBO9780511813955.

[AHLC+14] A. E. Almand-Hunter, H. Li, S. T. Cundiff, M. Mootz, M. Kira, and S. W. Koch. Quantum droplets of electrons and holes. *Nature* 506(7489), 471–475 (2014). 10.1038/nature12994.

[AOK+13] A. Askitopoulos, H. Ohadi, A. V. Kavokin, Z. Hatzopoulos, P. G. Savvidis, and P. G. Lagoudakis. Polariton condensation in an optically induced two-dimensional potential. *Physical Review B* 88(4), 041308 (2013). 10.1103/PhysRevB.88.041308.

[APA+19] A. Askitopoulos, L. Pickup, S. Alyatkin, A. Zasedatelev, K. G. Lagoudakis, W. Langbein, and P. G. Lagoudakis. Giant increase of temporal coherence in optically trapped polariton condensate. *arXiv* 1911.08981 (2019). 10.48550/arXiv.1911.08981.

[ASV+15] E. Agudelo, J. Sperling, W. Vogel, S. Köhnke, M. Mraz, and B. Hage. Continuous sampling of the squeezed-state nonclassicality. *Physical Review A* 92(3), 033837 (2015). 10.1103/PhysRevA.92.033837.

[ATV+11] M. Aßmann, J.-S. Tempel, F. Veit, M. Bayer, A. Rahimi-Iman, A. Löffler, S. Höfling, S. Reitzenstein, L. Worschech, and A. Forchel. From polariton condensates to highly photonic quantum degenerate states of bosonic matter. *Proceedings of the National Academy of Sciences* 108(5), 1804–1809 (2011). 10.1073/pnas.1009847108.

[AUM+07] S. Ates, S. M. Ulrich, P. Michler, S. Reitzenstein, A. Löffler, and A. Forchel. Coherence properties of high-β elliptical semiconductor micropillar lasers. *Applied Physics Letters* 90(16), 161111 (2007). 10.1063/1.2724908.

[AVT+10] M. Aßmann, F. Veit, J.-S. Tempel, T. Berstermann, H. Stolz, M. van der Poel, J. M. Hvam, and M. Bayer. Measuring the dynamics of second-order photon correlation functions inside a pulse with picosecond time resolution. *Optics Express* 18(19), 20229 (2010). 10.1364/OE.18.020229.

[AWH13] G. B. Arfken, H. J. Weber, and F. E. Harris. *Mathematical Methods for Physicists*. Elsevier 7th edition (2013).

[Bat22] Batop Optoelectronics. Refractive index n of GaAs. `https://www.batop.de/information/n_GaAs.html` (2022). Accessed on 05.05.2022.

[BBA+14] T. Boulier, M. Bamba, A. Amo, C. Adrados, A. Lemaitre, E. Galopin, I. Sagnes, J. Bloch, C. Ciuti, E. Giacobino, and A. Bramati. Polariton-generated intensity squeezing in semiconductor micropillars. *Nature Communications* 5(1), 3260 (2014). 10.1038/ncomms4260.

[BCP14] T. Baumgratz, M. Cramer, and M. B. Plenio. Quantifying Coherence. *Physical Review Letters* 113(14), 140401 (2014). 10.1103/PhysRevLett.113.140401.

[Ber21] B. Berger. *Control of Orbital Angular Momentum of Exciton Polariton Condensates*. Phd thesis TU Dortmund (2021).

[BGM+97] E. A. Burt, R. W. Ghrist, C. J. Myatt, M. J. Holland, E. A. Cornell, and C. E. Wieman. Coherence, Correlations, and Collisions: What One Learns about Bose-Einstein Condensates from Their Decay. *Physical Review Letters* 79(3), 337–340 (1997). 10.1103/PhysRevLett.79.337.

[BGRF09] F. Boitier, A. Godard, E. Rosencher, and C. Fabre. Measuring photon bunching at ultrashort timescale by two-photon absorption in semiconductors. *Nature Physics* 5(4), 267–270 (2009). 10.1038/nphys1218.

[BHM+14] C. Berger, U. Huttner, M. Mootz, M. Kira, S. W. Koch, J.-S. Tempel, M. Aßmann, M. Bayer, A. M. Mintairov, and J. L. Merz. Quantum-Memory Effects in the Emission of Quantum-Dot Microcavities. *Physical Review Letters* 113(9), 093902 (2014). 10.1103/PhysRevLett.113.093902.

[BKY14] T. Byrnes, N. Y. Kim, and Y. Yamamoto. Exciton–polariton condensates. *Nature Physics* 10(11), 803–813 (2014). 10.1038/nphys3143.

[BRS06] S. D. Bartlett, T. Rudolph, and R. W. Spekkens. Dialogue Concerning Two Views On Quantum Coherence: Factist And Fictionist. *International Journal of Quantum Information* 04(01), 17–43 (2006). 10.1142/S0219749906001591.

[BSM97] G. Breitenbach, S. Schiller, and J. Mlynek. Measurement of the quantum states of squeezed light. *Nature* 387(6632), 471–475 (1997). 10.1038/387471a0.

[BSS+00] J. J. Baumberg, P. G. Savvidis, R. M. Stevenson, A. I. Tartakovskii, M. S. Skolnick, D. M. Whittaker, and J. S. Roberts. Parametric oscillation in a vertical microcavity: A polariton condensate or micro-optical parametric oscillation. *Physical Review B* 62(24), R16247–R16250 (2000). 10.1103/PhysRevB.62.R16247.

[BZS+22] S. Baryshev, A. Zasedatelev, H. Sigurdsson, I. Gnusov, J. D. Töpfer, A. Askitopoulos, and P. G. Lagoudakis. Engineering Photon Statistics in a Spinor Polariton Condensate. *Physical Review Letters* 128(8), 087402 (2022). 10.1103/PhysRevLett.128.087402.

[CBD+18] D. Caputo, D. Ballarini, G. Dagvadorj, C. Sánchez Muñoz, M. De Giorgi, L. Dominici, K. West, L. N. Pfeiffer, G. Gigli, F. P. Laussy, M. H. Szymańska, and D. Sanvitto. Topological order and thermal equilibrium in polariton condensates. *Nature Materials* 17(2), 145–151 (2018). 10.1038/nmat5039.

[CC13] I. Carusotto and C. Ciuti. Quantum fluids of light. *Reviews of Modern Physics* 85(1), 299–366 (2013). 10.1103/RevModPhys.85.299.

[CG19] E. Chitambar and G. Gour. Quantum resource theories. *Reviews of Modern Physics* 91(2), 025001 (2019). 10.1103/RevModPhys.91.025001.

[CGZ+17] T. Cookson, K. Georgiou, A. Zasedatelev, R. T. Grant, T. Virgili, M. Cavazzini, F. Galeotti, C. Clark, N. G. Berloff, D. G. Lidzey, and P. G. Lagoudakis. A Yellow Polariton Condensate in a Dye Filled Microcavity. *Advanced Optical Materials* 5(18), 1700203 (2017). 10.1002/adom.201700203.

[CH16] E. Chitambar and M.-H. Hsieh. Relating the Resource Theories of Entanglement and Quantum Coherence. *Physical Review Letters* 117(2), 020402 (2016). 10.1103/PhysRevLett.117.020402.

[CKR09] A. Carmele, A. Knorr, and M. Richter. Photon statistics as a probe for exciton correlations in coupled nanostructures. *Physical Review B* 79(3), 035316 (2009). 10.1103/PhysRevB.79.035316.

[CLS+18] Á. Cuevas, J. C. López Carreño, B. Silva, M. De Giorgi, D. G. Suárez-Forero, C. Sánchez Muñoz, A. Fieramosca, F. Cardano, L. Marrucci, V. Tasco, G. Biasiol, E. del Valle, L. Dominici, D. Ballarini, G. Gigli, P. Mataloni, F. P. Laussy, F. Sciarrino, and D. Sanvitto. First observation of the quantized exciton-polariton field and effect of interactions on a single polariton. *Science Advances* 4(4), eaao6814 (2018). 10.1126/sciadv.aao6814.

[CQZ+11] Y. M. Chi, B. Qi, W. Zhu, L. Qian, H. K. Lo, S. H. Youn, A. I. Lvovsky, and L. Tian. A balanced homodyne detector for high-rate Gaussian-modulated coherent-state quantum key distribution. *New Journal of Physics* 13(1), 013003 (2011). 10.1088/1367-2630/13/1/013003.

[CRBS04] S. A. Crooker, D. G. Rickel, A. V. Balatsky, and D. L. Smith. Spectroscopy of spontaneous spin noise as a probe of spin dynamics and magnetic resonance. *Nature* 431(7004), 49–52 (2004). 10.1038/nature02804.

[DeL68] O. E. DeLange. Optical heterodyne detection. *IEEE Spectrum* 5(10), 77–85 (1968). 10.1109/MSPEC.1968.5215385.

[Deu20] I. H. Deutsch. Harnessing the Power of the Second Quantum Revolution. *PRX Quantum* 1(2), 020101 (2020). 10.1103/PRXQuantum.1.020101.

[DFS+19] A. Delteil, T. Fink, A. Schade, S. Höfling, C. Schneider, and A. İmamoğlu. Towards polariton blockade of confined exciton–polaritons. *Nature Materials* 18(3), 219–222 (2019). 10.1038/s41563-019-0282-y.

[DHY10] H. Deng, H. Haug, and Y. Yamamoto. Exciton-polariton Bose-Einstein condensation. *Reviews of Modern Physics* 82(2), 1489–1537 (2010). 10.1103/RevModPhys.82.1489.

[DM03] J. P. Dowling and G. J. Milburn. Quantum technology: the second quantum revolution. *Philosophical Transactions of the Royal Society of London. Series A: Mathematical, Physical and Engineering Sciences* 361(1809), 1655–1674 (2003). 10.1098/rsta.2003.1227.

[DMA+95] K. B. Davis, M. O. Mewes, M. R. Andrews, N. J. Van Druten, D. S. Durfee, D. M. Kurn, and W. Ketterle. Bose-Einstein condensation in a gas of sodium atoms. *Physical Review Letters* 75(22), 3969–3973 (1995). 10.1103/PhysRevLett.75.3969.

[DP12] B. Deveaud-Plédran. On the condensation of polaritons. *Journal of the Optical Society of America B* 29(2), A138 (2012). 10.1364/JOSAB.29.00A138.

[DSH+07] H. Deng, G. S. Solomon, R. Hey, K. H. Ploog, and Y. Yamamoto. Spatial coherence of a polariton condensate. *Physical Review Letters* 99(12), 126403 (2007). 10.1103/PhysRevLett.99.126403.

[DWS+02] H. Deng, G. Weihs, C. Santori, J. Bloch, and Y. Yamamoto. Condensation of semiconductor microcavity exciton polaritons. *Science* 298(5591), 199–202 (2002). 10.1126/science.1074464.

[EGB+18] E. Estrecho, T. Gao, N. Bobrovska, M. D. Fraser, M. Steger, L. Pfeiffer, K. West, T. C. H. Liew, M. Matuszewski, D. W. Snoke, A. G. Truscott, and E. A. Ostrovskaya. Single-shot condensation of exciton polaritons and the hole burning effect. *Nature Communications* 9(1), 2944 (2018). 10.1038/s41467-018-05349-4.

[EN16] A. L. Efros and D. J. Nesbitt. Origin and control of blinking in quantum dots. *Nature Nanotechnology* 11(8), 661–671 (2016). 10.1038/nnano.2016.140.

[EPW+21] E. Estrecho, M. Pieczarka, M. Wurdack, M. Steger, K. West, L. N. Pfeiffer, D. W. Snoke, A. G. Truscott, and E. A. Ostrovskaya. Low-Energy Collective Oscillations and Bogoliubov Sound in an Exciton-Polariton Condensate. *Physical Review Letters* 126(7), 075301 (2021). 10.1103/PhysRevLett.126.075301.

[Fis93] N. I. Fisher. *Statistical Analysis of Circular Data*. Cambridge University Press (1993). 10.1017/CBO9780511564345.

[Fli18] T. Fließbach. *Statistische Physik*. Springer Berlin Heidelberg Berlin, Heidelberg (2018).

[Fox06] M. Fox. *Quantum Optics - An Introduction*. Oxford University Press Oxford (2006).

[FSLQ+11] A. Farré, M. Shayegan, C. López-Quesada, G. A. Blab, M. Montes-Usategui, N. R. Forde, and E. Martín-Badosa. Positional stability of holographic optical traps. *Optics Express* 19(22), 21370 (2011). 10.1364/OE.19.021370.

[FXA+16] T. Ferreira da Silva, G. B. Xavier, G. C. Amaral, G. P. Temporão, and J. P. von der Weid. Quantum random number generation enhanced by weak-coherent states interference. *Optics Express* 24(17), 19574 (2016). 10.1364/OE.24.019574.

[Gla63] R. J. Glauber. Coherent and Incoherent States of the Radiation Field. *Physical Review* 131(6), 2766–2788 (1963). 10.1103/PhysRev.131.2766.

[GM14] R. Gross and A. Marx. *Festkörperphysik*. OLDENBOURG WISSENSCHAFTSVERLAG (2014). 10.1524/9783110358704.

[GST+21] I. Gnusov, H. Sigurdsson, J. Töpfer, S. Baryshev, S. Alyatkin, and P. Lagoudakis. All-Optical Linear-Polarization Engineering in Single and Coupled Exciton-Polariton Condensates. *Physical Review Applied* 16(3), 034014 (2021). 10.1103/PhysRevApplied.16.034014.

[HDCT12] H. Haug, T. D. Doan, H. T. Cao, and D. B. Thoai. Temporal first- and second-order correlations in a polariton condensate. *Physical Review B - Condensed Matter and Materials Physics* 85(20), 205310 (2012). 10.1103/PhysRevB.85.205310.

[HEOL19] R. Hanai, A. Edelman, Y. Ohashi, and P. B. Littlewood. Non-Hermitian Phase Transition from a Polariton Bose-Einstein Condensate to a Photon Laser. *Physical Review Letters* 122(18), 185301 (2019). 10.1103/PhysRevLett.122.185301.

[HFW+13] D. Huang, J. Fang, C. Wang, P. Huang, and G.-H. Zeng. A 300-MHz Bandwidth Balanced Homodyne Detector for Continuous Variable Quantum Key Distribution. *Chinese Physics Letters* 30(11), 114209 (2013). 10.1088/0256-307X/30/11/114209.

[HH77] E. Hanamura and H. Haug. Condensation effects of excitons. *Physics Reports* 33(4), 209–284 (1977). 10.1016/0370-1573(77)90012-6.

[HHHH09] R. Horodecki, P. Horodecki, M. Horodecki, and K. Horodecki. Quantum entanglement. *Reviews of Modern Physics* 81(2), 865–942 (2009). 10.1103/RevModPhys.81.865.

[HP06] J. A. Hansen and C. Penland. Efficient approximate techniques for integrating stochastic differential equations. *Monthly Weather Review* 134(10), 3006–3014 (2006). 10.1175/MWR3192.1.

[HSQ+10] T. Horikiri, P. Schwendimann, A. Quattropani, S. Höfling, A. Forchel, and Y. Yamamoto. Higher order coherence of exciton-polariton condensates. *Physical Review B - Condensed Matter and Materials Physics* 81(3), 033307 (2010). 10.1103/PhysRevB.81.033307.

[HT56] R. HANBURY BROWN and R. Q. TWISS. A Test of a New Type of Stellar Interferometer on Sirius. *Nature* 178(4541), 1046–1048 (1956). 10.1038/1781046a0.

[HWS+94] R. Houdré, C. Weisbuch, R. P. Stanley, U. Oesterle, P. Pellandini, and M. Ilegems. Measurement of cavity-polariton dispersion curve from angle-resolved photoluminescence experiments. *Physical Review Letters* 73(15), 2043–2046 (1994). 10.1103/PhysRevLett.73.2043.

[JBA+03] S. Jochim, M. Bartenstein, A. Altmeyer, G. Hendl, S. Riedl, C. Chin, J. Hecker Denschtag, and R. Grimm. Bose-Einstein Condensation of Molecules. *Science* 302(5653), 2101–2103 (2003). 10.1126/science.1093280.

[KAD+07] J. Kasprzak, R. André, L. S. Dang, I. A. Shelykh, A. V. Kavokin, Y. G. Rubo, K. V. Kavokin, and G. Malpuech. Build up and pinning of linear polarization in the Bose condensates of exciton polaritons. *Physical Review B* 75(4), 045326 (2007). 10.1103/PhysRevB.75.045326.

[KBK+15] G. Kurizki, P. Bertet, Y. Kubo, K. Mølmer, D. Petrosyan, P. Rabl, and J. Schmiedmayer. Quantum technologies with hybrid systems. *Proceedings of the National Academy of Sciences* 112(13), 3866–3873 (2015). 10.1073/pnas.1419326112.

[KBM+12] R. Kumar, E. Barrios, A. MacRae, E. Cairns, E. Huntington, and A. Lvovsky. Versatile wideband balanced detector for quantum optical homodyne tomography. *Optics Communications* 285(24), 5259–5267 (2012). 10.1016/j.optcom.2012.07.103.

[KBML17] A. V. Kavokin, J. J. Baumberg, G. Malpuech, and F. P. Laussy. *Microcavities*. Oxford University Press Oxford 2nd edition (2017). 10.1093/oso/9780198782995.001.0001.

[KFA+18] M. Klaas, H. Flayac, M. Amthor, I. G. Savenko, S. Brodbeck, T. Ala-Nissila, S. Klembt, C. Schneider, and S. Höfling. Evolution of Temporal Coherence in Confined Exciton-Polariton Condensates. *Physical Review Letters* 120(1), 017401 (2018). 10.1103/PhysRevLett.120.017401.

[KK06] M. Kira and S. W. Koch. Quantum-optical spectroscopy of semiconductors. *Physical Review A* 73(1), 013813 (2006). 10.1103/PhysRevA.73.013813.

[KKS+11] M. Kira, S. W. Koch, R. P. Smith, A. E. Hunter, and S. T. Cundiff. Quantum spectroscopy with Schrödinger-cat states. *Nature Physics* 7(10), 799–804 (2011). 10.1038/nphys2091.

[KLS+22] A. Kavokin, T. C. H. Liew, C. Schneider, P. G. Lagoudakis, S. Klembt, and S. Hoefling. Polariton condensates for classical and quantum computing. *Nature Reviews Physics* 4(7), 435–451 (2022). 10.1038/s42254-022-00447-1.

[KMA+06] Kłopotowski, M. D. Martín, A. Amo, L. Viña, I. A. Shelykh, M. M. Glazov, G. Malpuech, A. V. Kavokin, and R. André. Optical anisotropy and pinning of the linear polarization of light in semiconductor microcavities. *Solid State Communications* 139(10), 511–515 (2006). 10.1016/j.ssc.2006.07.016.

[KMSL07] J. Keeling, F. M. Marchetti, M. H. Szymańska, and P. B. Littlewood. Collective coherence in planar semiconductor microcavities. *Semiconductor Science and Technology* 22(5), R1–R26 (2007). 10.1088/0268-1242/22/5/R01.

[KRK+06] J. Kasprzak, M. Richard, S. Kundermann, A. Baas, P. Jeambrun, J. M. J. Keeling, F. M. Marchetti, M. H. Szymańska, R. André, J. L. Staehli, V. Savona, P. B. Littlewood, B. Deveaud, and L. S. Dang. Bose–Einstein condensation of exciton polaritons. *Nature* 443(7110), 409–414 (2006). 10.1038/nature05131.

[KSA+15] T. Kazimierczuk, J. Schmutzler, M. Aßmann, C. Schneider, M. Kamp, S. Höfling, and M. Bayer. Photon-Statistics Excitation Spectroscopy of a Quantum-Dot Micropillar Laser. *Physical Review Letters* 115(2), 027401 (2015). 10.1103/PhysRevLett.115.027401.

[KSF+18] M. Klaas, E. Schlottmann, H. Flayac, F. P. Laussy, F. Gericke, M. Schmidt, M. v. Helversen, J. Beyer, S. Brodbeck, H. Suchomel, S. Höfling, S. Reitzenstein, and C. Schneider. Photon-Number-Resolved

Measurement of an Exciton-Polariton Condensate. *Physical Review Letters* 121(4), 047401 (2018). 10.1103/PhysRevLett.121.047401.

[KSP16] N. Killoran, F. E. Steinhoff, and M. B. Plenio. Converting Nonclassicality into Entanglement. *Physical Review Letters* 116(8), 080402 (2016). 10.1103/PhysRevLett.116.080402.

[KSS+14] D. Kim, Z. Shi, C. B. Simmons, D. R. Ward, J. R. Prance, T. S. Koh, J. K. Gamble, D. E. Savage, M. G. Lagally, M. Friesen, S. N. Coppersmith, and M. A. Eriksson. Quantum control and process tomography of a semiconductor quantum dot hybrid qubit. *Nature* 511(7507), 70–74 (2014). 10.1038/nature13407.

[KV10] T. Kiesel and W. Vogel. Nonclassicality filters and quasiprobabilities. *Physical Review A* 82(3), 032107 (2010). 10.1103/PhysRevA.82.032107.

[KV12] T. Kiesel and W. Vogel. Universal nonclassicality witnesses for harmonic oscillators. *Physical Review A - Atomic, Molecular, and Optical Physics* 85(6), 062106 (2012). 10.1103/PhysRevA.85.062106.

[KV14] B. Kühn and W. Vogel. Visualizing nonclassical effects in phase space. *Physical Review A - Atomic, Molecular, and Optical Physics* 90(3), 033821 (2014). 10.1103/PhysRevA.90.033821.

[KVBZ11] T. Kiesel, W. Vogel, M. Bellini, and A. Zavatta. Nonclassicality quasiprobability of single-photon-added thermal states. *Physical Review A - Atomic, Molecular, and Optical Physics* 83(3), 032116 (2011). 10.1103/PhysRevA.83.032116.

[KvHR+20] T. Kupko, M. von Helversen, L. Rickert, J. H. Schulze, A. Strittmatter, M. Gschrey, S. Rodt, S. Reitzenstein, and T. Heindel. Tools for the performance optimization of single-photon quantum key distribution. *npj Quantum Information* 6(1), 29 (2020). 10.1038/s41534-020-0262-8.

[KVHS11] T. Kiesel, W. Vogel, B. Hage, and R. Schnabel. Direct Sampling of Negative Quasiprobabilities of a Squeezed State. *Physical Review Letters* 107(11), 113604 (2011). 10.1103/PhysRevLett.107.113604.

[KVT+21] B. Kühn, W. Vogel, V. Thiel, S. Merkouche, and B. J. Smith. Gaussian versus Non-Gaussian Filtering of Phase-Insensitive Nonclassicality. *Physical Review Letters* 126(17), 173603 (2021). 10.1103/PhysRevLett.126.173603.

[KZW+16] S. Kim, B. Zhang, Z. Wang, J. Fischer, S. Brodbeck, M. Kamp, C. Schneider, S. Höfling, and H. Deng. Coherent polariton laser. *Physical Review X* 6(1), 011026 (2016). 10.1103/PhysRevX.6.011026.

[LA20] C. Lüders and M. Aßmann. Distinguishing intrinsic photon correlations from external noise with frequency-resolved homodyne detection. *Scientific Reports* 10(1), 22411 (2020). 10.1038/s41598-020-79686-0.

[Lac65] G. Lachs. Theoretical Aspects of Mixtures of Thermal and Coherent Radiation. *Physical Review* 138(4B), B1012–B1016 (1965). 10.1103/PhysRev.138.B1012.

[LHA+13] H. A. M. Leymann, C. Hopfmann, F. Albert, A. Foerster, M. Khanbekyan, C. Schneider, S. Höfling, A. Forchel, M. Kamp, J. Wiersig, and S. Reitzenstein. Intensity fluctuations in bimodal micropillar lasers enhanced by quantum-dot gain competition. *Physical Review A* 87(5), 053819 (2013). 10.1103/PhysRevA.87.053819.

[LKK+08] M. Lobino, D. Korystov, C. Kupchak, E. Figueroa, B. C. Sanders, and A. I. Lvovsky. Complete characterization of quantum-optical processes. *Science* 322(5901), 563–566 (2008). 10.1126/science.1162086.

[LKW+08] A. P. Love, D. N. Krizhanovskii, D. M. Whittaker, R. Bouchekioua, D. Sanvitto, S. A. Al Rizeiqi, R. Bradley, M. S. Skolnick, P. R. Eastham, R. André, and L. S. Dang. Intrinsic decoherence mechanisms in the microcavity polariton condensate. *Physical Review Letters* 101(6), 067404 (2008). 10.1103/PhysRevLett.101.067404.

[LM14] F. Levi and F. Mintert. A quantitative theory of coherent delocalization. *New Journal of Physics* 16(3), 033007 (2014). 10.1088/1367-2630/16/3/033007.

[Lou83] R. Loudon. *The Quantum Theory of Light*. Oxford University Press Oxford 2nd edition (1983).

[LPB+] C. Lüders, M. Pukrop, F. Barkhausen, E. Rozas, C. Schneider, S. Höfling, J. Sperling, S. Schumacher, and M. Aßmann. Tracking quantum coherence in polariton condensates with time-resolved tomography. *In Preparation*.

[LPR+21] C. Lüders, M. Pukrop, E. Rozas, C. Schneider, S. Höfling, J. Sperling, S. Schumacher, and M. Aßmann. Quantifying Quantum Coherence in Polariton Condensates. *PRX Quantum* 2(3), 030320 (2021). 10.1103/PRXQuantum.2.030320.

[LR09] A. I. Lvovsky and M. G. Raymer. Continuous-variable optical quantum-state tomography. *Reviews of Modern Physics* 81(1), 299–332 (2009). 10.1103/RevModPhys.81.299.

[LSS+15] J. C. López Carreño, C. Sánchez Muñoz, D. Sanvitto, E. del Valle, and F. P. Laussy. Exciting Polaritons with Quantum Light. *Physical Review Letters* 115(19), 196402 (2015). 10.1103/PhysRevLett.115.196402.

[LTA18] C. Lüders, J. Thewes, and M. Assmann. Real time g (2) monitoring with 100 kHz sampling rate. *Optics Express* 26(19), 24854 (2018). 10.1364/OE.26.024854.

[Mac11] C. A. Mack. Fifty Years of Moore's Law. *IEEE Transactions on Semiconductor Manufacturing* 24(2), 202–207 (2011). 10.1109/TSM.2010.2096437.

[Man86] L. Mandel. Non-Classical States of the Electromagnetic Field. *Physica Scripta* T12(T12), 34–42 (1986). 10.1088/0031-8949/1986/T12/005.

[MBA+20] X. Ma, B. Berger, M. Aßmann, R. Driben, T. Meier, C. Schneider, S. Höfling, and S. Schumacher. Realization of all-optical vortex switching in exciton-polariton condensates. *Nature Communications* 11(1), 897 (2020). 10.1038/s41467-020-14702-5.

[MBAR95] M. Munroe, D. Boggavarapu, M. E. Anderson, and M. G. Raymer. Photon-number statistics from the phase-averaged quadrature-field distribution: Theory and ultrafast measurement. *Physical Review A* 52(2), R924–R927 (1995). 10.1103/PhysRevA.52.R924.

[MGF+10] A. Mohan, P. Gallo, M. Felici, B. Dwir, A. Rudra, J. Faist, and E. Kapon. Record-low inhomogeneous broadening of site-controlled quantum dots for nanophotonics. *Small* 6(12), 1268–1272 (2010). 10.1002/smll.201000341.

[MLC92] H. Mathieu, P. Lefebvre, and P. Christol. Simple analytical method for calculating exciton binding energies in semiconductor quantum wells. *Physical Review B* 46(7), 4092–4101 (1992). 10.1103/PhysRevB.46.4092.

[MMWJ+19] G. Muñoz-Matutano, A. Wood, M. Johnsson, X. Vidal, B. Q. Baragiola, A. Reinhard, A. Lemaître, J. Bloch, A. Amo, G. Nogues, B. Besga, M. Richard, and T. Volz. Emergence of quantum correlations from interacting fibre-cavity polaritons. *Nature Materials* 18(3), 213–218 (2019). 10.1038/s41563-019-0281-z.

[MR97] D. F. McAlister and M. G. Raymer. Ultrafast photon-number correlations from dual-pulse, phase-averaged homodyne detection. *Physical Review A* 55(3), R1609–R1612 (1997). 10.1103/PhysRevA.55.R1609.

[MW62] L. Mandel and E. Wolf. The measures of bandwidth and coherence time in optics. *Proceedings of the Physical Society* 80(4), 894–897 (1962). 10.1088/0370-1328/80/4/311.

[MW95] L. Mandel and E. Wolf. *Optical Coherence and Quantum Optics*. Cambridge University Press (1995). 10.1017/cbo9781139644105.

[MYG+16] J. Ma, B. Yadin, D. Girolami, V. Vedral, and M. Gu. Converting Coherence to Quantum Correlations. *Physical Review Letters* 116(16), 160407 (2016). 10.1103/PhysRevLett.116.160407.

[Nol14] W. Nolting. *Grundkurs Theoretische Physik 6*. Springer (2014).

[ORHH05] M. Oestreich, M. Römer, R. J. Haug, and D. Hägele. Spin Noise Spectroscopy in GaAs. *Physical Review Letters* 95(21), 216603 (2005). 10.1103/PhysRevLett.95.216603.

[OTP+21] K. Orfanakis, A. F. Tzortzakakis, D. Petrosyan, P. G. Savvidis, and H. Ohadi. Ultralong temporal coherence in optically trapped exciton-polariton condensates. *Physical Review B* 103(23), 235313 (2021). 10.1103/PhysRevB.103.235313.

[PAB+20] S. Pirandola, U. L. Andersen, L. Banchi, M. Berta, D. Bunandar, R. Colbeck, D. Englund, T. Gehring, C. Lupo, C. Ottaviani, J. L. Pereira, M. Razavi, J. Shamsul Shaari, M. Tomamichel, V. C. Usenko, G. Vallone, P. Villoresi, and P. Wallden. Advances in quantum cryptography. *Advances in Optics and Photonics* 12(4), 1012 (2020). 10.1364/aop.361502.

[Pol22] M. N. Polyanskiy. Refractive index database. `https://refractiveindex.info/?shelf=main&book=GaAs&page=Aspnes` (2022). Accessed on 05.05.2022.

[PPLG10] K. D. Petersson, J. R. Petta, H. Lu, and A. C. Gossard. Quantum coherence in a one-electron semiconductor charge qubit. *Physical Review Letters* 105(24), 246804 (2010). 10.1103/PhysRevLett.105.246804.

[PS03] L. Pitaevskii and S. Stringari. *Bose-Einstein Condensation*. Oxford Science Publications Oxford (2003).

[PT03] D. Porras and C. Tejedor. Linewidth of a polariton laser: Theoretical analysis of self-interaction effects. *Physical Review B - Condensed Matter and Materials Physics* 67(16), 161310 (2003). 10.1103/PhysRevB.67.161310.

[Puk22] M. Pukrop. *Exploring Roads to Functionality of Polaritons in Semiconductor Microcavities*. Phd thesis Universität Paderborn (2022).

[QSG+18] L.-F. Qiao, A. Streltsov, J. Gao, S. Rana, R.-J. Ren, Z.-Q. Jiao, C.-Q. Hu, X.-Y. Xu, C.-Y. Wang, H. Tang, A.-L. Yang, Z.-H. Ma, M. Lewenstein, and X.-M. Jin. Entanglement activation from quantum coherence and superposition. *Physical Review A* 98(5), 052351 (2018). 10.1103/PhysRevA.98.052351.

[RC13] G. Roumpos and S. T. Cundiff. Multichannel homodyne detection for quantum optical tomography. *Journal of the Optical Society of America B* 30(5), 1303 (2013). 10.1364/JOSAB.30.001303.

[RKL+10] M. Romanelli, J. P. Karr, C. Leyder, E. Giacobino, and A. Bramati. Two-mode squeezing in polariton four-wave mixing. *Physical Review B* 82(15), 155313 (2010). 10.1103/PhysRevB.82.155313.

[SAL11] T. Symul, S. M. Assad, and P. K. Lam. Real time demonstration of high bitrate quantum random number generation with coherent laser light. *Applied Physics Letters* 98(23), 231103 (2011). 10.1063/1.3597793.

[SAP17] A. Streltsov, G. Adesso, and M. B. Plenio. Colloquium: Quantum coherence as a resource. *Reviews of Modern Physics* 89(4), 041003 (2017). 10.1103/RevModPhys.89.041003.

[SBRF93] D. T. Smithey, M. Beck, M. G. Raymer, and A. Faridani. Measurement of the Wigner distribution and the density matrix of a light mode using optical homodyne tomography: Application to squeezed states and the vacuum. *Physical Review Letters* 70(9), 1244–1247 (1993). 10.1103/PhysRevLett.70.1244.

[Sch01] W. P. Schleich. *Quantum Optics in Phase Space*. Wiley (2001). 10.1002/3527602976.

[Sch19] D. Schmidt. *Exciton Polariton Interactions in Tailored Optical Potential Landscapes in Semiconductor Microcavities*. Phd thesis TU Dortmund (2019).

[SFW98] M. S. Skolnick, T. A. Fisher, and D. M. Whittaker. Strong coupling phenomena in quantum microcavity structures. *Semiconductor Science and Technology* 13(7), 645–669 (1998). 10.1088/0268-1242/13/7/003.

[SGD+16] N. Somaschi, V. Giesz, L. De Santis, J. C. Loredo, M. P. Almeida, G. Hornecker, S. L. Portalupi, T. Grange, C. Antón, J. Demory, C. Gómez, I. Sagnes, N. D. Lanzillotti-Kimura, A. Lemaítre, A. Auffeves, A. G. White, L. Lanco, and P. Senellart. Near-optimal single-photon sources in the solid state. *Nature Photonics* 10(5), 340–345 (2016). 10.1038/nphoton.2016.23.

[Sig20] H. Sigurdsson. Hysteresis in linearly polarized nonresonantly driven exciton-polariton condensates. *Physical Review Research* 2(2), 023323 (2020). 10.1103/PhysRevResearch.2.023323.

[SKL07] M. H. Szymańska, J. Keeling, and P. B. Littlewood. Mean-field theory and fluctuation spectrum of a pumped decaying Bose-Fermi system across the quantum condensation transition. *Physical Review B* 75(19), 195331 (2007). 10.1103/PhysRevB.75.195331.

[SLC02] A. Sinatra, C. Lobo, and Y. Castin. The truncated Wigner method for Bose-condensed gases: limits of validity and applications. *Journal of Physics B: Atomic, Molecular and Optical Physics* 35(17), 3599–3631 (2002). 10.1088/0953-4075/35/17/301.

[SQ08] P. Schwendimann and A. Quattropani. Statistics of the polariton condensate. *Physical Review B* 77(8), 085317 (2008). 10.1103/PhysRevB.77.085317.

[SSK+19] E. Schlottmann, D. Schicke, F. Krüger, B. Lingnau, C. Schneider, S. Höfling, K. Lüdge, X. Porte, and S. Reitzenstein. Stochastic polarization switching induced by optical injection in bimodal quantum-dot micropillar lasers. *Optics Express* 27(20), 28816 (2019). 10.1364/OE.27.028816.

[SSQ08] D. Sarchi, P. Schwendimann, and A. Quattropani. Effects of noise in different approaches for the statistics of polariton condensates. *Physical Review B* 78(7), 073404 (2008). 10.1103/physrevb.78.073404.

[STP+96] V. Savona, F. Tassone, C. Piermarocchi, A. Quattropani, and P. Schwendimann. Theory of polariton photoluminescence in arbitrary semiconductor microcavity structures. *Physical Review B - Condensed Matter and Materials Physics* 53(19), 13051–13062 (1996). 10.1103/PhysRevB.53.13051.

[Sud63] E. C. Sudarshan. Equivalence of semiclassical and quantum mechanical descriptions of statistical light beams. *Physical Review Letters* 10(7), 277–279 (1963). 10.1103/PhysRevLett.10.277.

[SV20] J. Sperling and W. Vogel. Quasiprobability distributions for quantum-optical coherence and beyond. *Physica Scripta* 95(3), 034007 (2020). 10.1088/1402-4896/ab5501.

[SW18] J. Sperling and I. A. Walmsley. Quasiprobability representation of quantum coherence. *Physical Review A* 97(6), 062327 (2018). 10.1103/PhysRevA.97.062327.

[The18] J. Thewes. *Non-Stationary Optical Homodyne Tomography*. Phd thesis TU Dortmund (2018).

[TLA20] J. Thewes, C. Lüders, and M. Aßmann. Conditional spectroscopy via nonstationary optical homodyne quantum state tomography. *Physical Review A* 101(2), 023824 (2020). 10.1103/PhysRevA.101.023824.

[TMJ+17] Y. S. Teo, C. R. Müller, H. Jeong, Z. Hradil, J. Řeháček, and L. L. Sánchez-Soto. Superiority of heterodyning over homodyning: An assessment with quadrature moments. *Physical Review A* 95(4), 042322 (2017). 10.1103/PhysRevA.95.042322.

[TVA+12] J. S. Tempel, F. Veit, M. Aßmann, L. E. Kreilkamp, A. Rahimi-Iman, A. Löffler, S. Höfling, S. Reitzenstein, L. Worschech, A. Forchel, and M. Bayer. Characterization of two-threshold behavior of the emission from a GaAs microcavity. *Physical Review B - Condensed Matter and Materials Physics* 85(7), 075318 (2012). 10.1103/PhysRevB.85.075318.

[UKDD22] W. Uddin, B. Khan, S. Dewan, and S. Das. Silicon-based qubit technology: progress and future prospects. *Bulletin of Materials Science* 45(1), 46 (2022). 10.1007/s12034-021-02621-0.

[VS14] W. Vogel and J. Sperling. Unified quantification of nonclassicality and entanglement. *Physical Review A - Atomic, Molecular, and Optical Physics* 89(5), 052302 (2014). 10.1103/PhysRevA.89.052302.

[VW06] W. Vogel and D.-G. Welsch. *Quantum Optics*. Wiley-VCH Verlag Weinheim 3rd edition (2006).

[Wal83] D. F. Walls. Squeezed states of light. *Nature* 306(5939), 141–146 (1983). 10.1038/306141a0.

[Wal16] M. M. Waldrop. More Than Moore. *Nature* 530(7589), 144–147 (2016). 10.1038/530144a.

[WC07] M. Wouters and I. Carusotto. Excitations in a nonequilibrium bose-einstein condensate of exciton polaritons. *Physical Review Letters* 99(14), 140402 (2007). 10.1103/PhysRevLett.99.140402.

[WCC08] M. Wouters, I. Carusotto, and C. Ciuti. Spatial and spectral shape of inhomogeneous nonequilibrium exciton-polariton condensates. *Physical Review B - Condensed Matter and Materials Physics* 77(11), 115340 (2008). 10.1103/PhysRevB.77.115340.

[WDE+17] C. E. Whittaker, B. Dzurnak, O. A. Egorov, G. Buonaiuto, P. M. Walker, E. Cancellieri, D. M. Whittaker, E. Clarke, S. S. Gavrilov, M. S. Skolnick, and D. N. Krizhanovskii. Polariton pattern formation photon statistics of the associated emission. *Physical Review X* 7(3), 031033 (2017). 10.1103/PhysRevX.7.031033.

[WE09] D. M. Whittaker and P. R. Eastham. Coherence properties of the microcavity polariton condensate. *EPL (Europhysics Letters)* 87(2), 27002 (2009). 10.1209/0295-5075/87/27002.

[WFS+10] E. Wertz, L. Ferrier, D. D. Solnyshkov, R. Johne, D. Sanvitto, A. Lemaâtre, I. Sagnes, R. Grousson, A. V. Kavokin, P. Senellart, G. Malpuech, and J. Bloch. Spontaneous formation and optical manipulation of extended polariton condensates. *Nature Physics* 6(11), 860–864 (2010). 10.1038/nphys1750.

[Wil17] R. S. Williams. What's Next? [The end of Moore's law]. *Computing in Science Engineering* 19(2), 7–13 (2017). 10.1109/MCSE.2017.31.

[WS09] M. Wouters and V. Savona. Stochastic classical field model for polariton condensates. *Physical Review B* 79(16), 165302 (2009). 10.1103/PhysRevB.79.165302.

[WSF+21] J. Wu, R. Su, A. Fieramosca, S. Ghosh, J. Zhao, T. C. H. Liew, and Q. Xiong. Perovskite polariton parametric oscillator. *Advanced Photonics* 3(05), 055003 (2021). 10.1117/1.AP.3.5.055003.

[YC83] H. P. Yuen and V. W. S. Chan. Noise in homodyne and heterodyne detection. *Optics Letters* 8(3), 177 (1983). 10.1364/OL.8.000177.

[ZSS+03] M. W. Zwierlein, C. A. Stan, C. H. Schunck, S. M. Raupach, S. Gupta, Z. Hadzibabic, and W. Ketterle. Observation of bose-einstein condensation of molecules. *Physical Review Letters* 91(25), 250401 (2003). 10.1103/PhysRevLett.91.250401.

Scientific Contributions

Publications

C. Lüders, J. Thewes, and M. Assmann, Real time $g^{(2)}$ monitoring with 100 kHz sampling rate, Opt. Express 26, 24854 (2018).

J. Thewes, **C. Lüders**, and M. Aßmann, Eavesdropping attack on a trusted continuous-variable quantum random-number generator, Physical Review A 100(5), 052318 (2019).

J. Thewes, J., **C. Lüders**, and M. Aßmann, Conditional spectroscopy via nonstationary optical homodyne quantum state tomography, Physical Review A 101(2), 23824 (2020).

C. Lüders and M. Aßmann, Distinguishing intrinsic photon correlations from external noise with frequency-resolved homodyne detection, Scientific Reports 10(1), 22411 (2020).

C. Lüders, M. Pukrop, E. Rozas, C. Schneider, S. Höfling, J. Sperling, S. Schumacher, and M. Aßmann, Quantifying Quantum Coherence in Polariton Condensates, PRX Quantum 2(3), 030320 (2021).

C. Lüders, J. Gil-Lopez, M. Allgaier, B. Brecht, M. Aßmann, C. Silberhorn and M. Bayer, Tailored frequency conversion makes infrared light visible for streak cameras, Submitted. ArXiv: 2206.05074

C. Lüders, M. Pukrop, F. Barkhausen, E. Rozas, C. Schneider, S. Höfling, J. Sperling, S. Schumacher, and M. Aßmann, Tracking quantum coherence in polariton condensates with time-resolved tomography, in preparation.

Talks and Conferences

7^{th} International Collaborative Research Centre TRR 142 workshop Tailored Nonlinear Photonics 2020 (online): 15 min oral presentation: "Frequency conversion for time-resolved spectroscopy"

17^{th} Optics of Excitons in Confined Systems Conference 2021 in Dortmund, Germany (online): Poster: "Quantifying Quantum Coherence in Polariton Condensates"

International Conference on Physics of Light-Matter Coupling in Nanostructures 2022 in Varadero, Cuba: 15 min oral presentation: "Quantifying Quantum Coherence in Polariton Condensates"

Photon 2022 in Nottingham, UK: 15 min oral presentation: "Tracking quantum coherence in polariton condensates with time-resolved tomography"

Supervised thesis

L. Büthe, Phasensensitive Messungen der Interferenz zweier unabhängiger Lichtquellen mittels homodyner Detektion, Master Thesis, TU Dortmund University, Experimentelle Physik 2 (2022)

Acknowledgments

At this point I would like to thank many people without whom this work would not have been possible. First of all, I thank Prof. Dr. Manfred Bayer for welcoming me to the chair EIIa with its excellently equipped laboratories. I'm grateful to Prof. Dr. Marc Aßmann for his friendly and competent supervision, for always listening to my questions and for numerous suggestions for research. I thank Dr. Johannes Thewes for teaching me everything he knew in a patient and humorous manner. I'm grateful to Dr. Daniel Schmidt and Dr. Bernd Berger for sharing their profound knowledge on the spectroscopy of exciton polaritons and more. Also, thanks to master student Lea Büthe for spending time with me in the lab, contributing with many ideas of her own. The other coworkers in this lab, Dr. Elena Rozas Jimenez and Yannik Brune, also deserve thanks for their contribution, their ideas and their eager spirit.
Regarding the Paderborn team, special thanks goes to Prof. Dr. Jan Sperling for sharing his extensive knowledge on quantum optics, his readiness to answer my questions and his friendly and encouraging spirit. I also thank Prof. Dr. Stefan Schumacher, Dr. Matthias Pukrop and Franziska Barkhausen for their diligent work. All in all, the collaboration was a joyful experience.
Concerning the frequency conversion project I also worked on, I thank Dr. Benjamin Brecht and Dr. Jano Gil López for their kind collaboration.
Likewise, I would like to thank Lars Wieschollek for his competent support in technical matters, as well as Michaela Wäscher and Katharina Sparka for their excellent administrative work that keeps this chair running.
All other members of EII also deserve praise for the warm atmosphere they create at this chair and for sharing the hardships of PhD studies, specifically Dr. Jan Mundry, Carl Arne Thomann, Patrick Lindner, Lars Klompmaker, Dr. Janina Rautert, Janina Schindler, Dr. Laura Krauß-Kodytek, and many others.
Last but not least, I would like to thank all friends who have accompanied me during these years, in particular Gary Schmiedinghoff and Alexandra Högl, and my parents Sieglinde and Lennart Lüders and my brother Christoph for their loving support.

Appendix A

Information on Matlab data processing

The Matlab scripts used in this work were developed by Johannes Thewes and me. They can be found in github:

`https://github.com/CarolinLueders/QST`
(Repository: QST, User: CarolinLueders)

A.1 Computation of quadratures from raw data

A homodyne measurement consists of a measurement without signal, in order to calibrate the number of photons of the LO, and a measurement with signal. These usually have file names of the form "01-xxmW-LOonly.raw" and "02-xxmW-LOwithDL.raw", respectively, and are stored in a folder called "raw-data". In the following, the file names will be referred to with the placeholders filenameLO and filenameSIG.
First, the quadratures are computed from the raw data. Therefore, in Matlab, one needs to be in the folder just above the folder "raw-data".
For a series of datasets, it is most convenient to run **seriesQuadratures**, which computes the quadratures for each dataset and saves them in a folder called "mat-data". This function uses the function **prepareData(filenameLO,filenameSIG)**, executing **computeQuadratures**, which integrates the data around the locations of the LO pulses to obtain the quadratures. Different options can be set:

- Detection channels to be calculated: e.g. **seriesQuadratures('Channels',1:3)**.

- Piezo modulation usage, in order to cut the data into pieces according to the back and forth sweeping of the piezo:
  seriesQuadratures('Channels',1:3,'Piezo','yes'); (or 'Piezo','no')

- Numerical removal of correlations between adjacent quadratures. It should be used for any signal with random phase, but it does not work if the signal has a fixed phase with respect to the LO. It should be set for each of the three channels, e.g. **'CorrRemove',[true,true,true] or [false,false,false]**.

- Subtraction of an offset: This should be done for each set of 1000 pulses individually when there is a random phase between LO and signal (**'Offset',["local" "local" "local"]**) or for the whole dataset when there is a fixed phase (**'Offset',** **["global" "global" "global"]**).

- An example for a signal with random phase:
  seriesQuadratures('Channels',1:3,'Offset',["local" "local" "local"], 'Piezo','yes','CorrRemove',[true,true,true]);

- An example for a signal with non-random phase:
  seriesQuadratures('Channels',1:3,'Offset',["global" "global" "global"], 'Piezo','yes','CorrRemove',[false,false,false]);

The computed quadratures X should be a matrix with size 999 x A x B, or 999 x A when no piezo was used, since B is the number of piezo path segments. The first dimension stems from the badges of 1000 pulses as which the data are stored. One pulse is removed after the numerical removal of correlations. If the length is significantly more or less than 999, this means the pulses are not recognized correctly, hinting at overexposure of the detectors.

A.2 Troubleshooting

If anything goes wrong, it might be helpful to look at the data itself.

- Load raw data using **data8bit = load8BitBinary(filename,'dontsave');** Plot this to see irregularities.

- Examine the variances of LOonly data with
  plotPointwiseVariance(data8bit(:,:,channel));
  This should show a peak for each LO pulse, but otherwise have a steady offset. If the offset is strangely varying, this might come from overexposure of the detectors.

- Plot the LOonly data of each channel and look if it is steady around zero. If it has a varying offset, this hints at mechanical instability.

- Plot the computed quadratures, e.g. **plot(X1(:),'.')** and **histogram(X1)**. For a signal with random phase, the quadratures should be distributed around zero. For a thermal signal, it should be a Gaussian distribution. For a coherent signal with random phase, the distribution should have two peaks symmetrical around zero.

A.3 Computation of $g^{(2)}(0)$

After the quadratures are computed as explained above and stored in the folder "mat-data", we can compute the second-order photon correlation and plot it versus time.

- Computation of photon number and $g^{(2)}(0)$ for a series of datasets, e.g.:
  g2SeriesFromQuadratures(nResolution,'Weight','yes','UseX','X1', 'Parameter','power');
  This function creates time-resolved plots of $g^{(2)}(0)$ and photon number for each dataset. It stores the time-resolved $g^{(2)}(0)$ values **g2vec**, the photon number values **ada** and the time vector **time** in a new folder, and it plots the average values of each dataset versus the parameter that was varied in the series. With **nResolution**, choose the number of quadratures that is used to compute one $g^{(2)}(0)$ value. Usually, 1000 is a good choice. 'UseX' sets which quadrature is used, e.g. 'X1' for channel 1. 'Parameter' describes which parameter is varied in the series. When setting 'Weight','yes', the $g^{(2)}(0)$ values are weighted with the corresponding photon numbers when the average is computed for each dataset.

- For a single quadrature dataset X, the time-resolved values can be computed via **[g2vec, ada, time] = g2(X, nResolution)**;

- Different averaging frequencies can be compared with **g2compareSamplingRate(X, filename)**, e.g. for the evaluation in Chapter 6.

A.4 Evaluation of 2 Channel Measurements of Husimi functions

As an example, let us assume that channels 1 and 2 were used for the measurement and in channel 1, the piezo was modulated.

- First, the quadratures are computed with
  seriesQuadratures('Channels',1:2,'Offset',["local" "local" "local"], 'Piezo','yes','CorrRemove',[true,true,true]);

- For a series of measurements, e.g. a power series, the Husimi functions can be evaluated with

HusimiSeriesFromQuadratures([3,1,2],'LoadExistent',false, 'PlotErrorbars',true,'FitMethod','NLSQ-LAR','Scale',true, 'PlotOption',true,'MonteCarloError',true,'Parameter','power');
This function plots the Husimi function for each dataset, fits the Husimi function to the theoretical model of the displaced thermal state, and plots the coherent and thermal photon number and the quantum coherence derived from the fit. If there is a big variation of the photon number during one measurement, the Husimi function is derived for the instances with high and with low photon number separately.
Thereby, [3,1,2] assigns which channel was used for what. In general, [a,b,c] assigns the target channel a, which is not used here, the channel with piezo modulation b and the remnant channel c. 'LoadExistent' can be set true to speed up the evaluation when the orthogonal quadratures O1,O2 and the photon numbers have already been computed and saved in the quadrature datasets. 'FitMethod','NLSQ-LAR' sets the best method for fitting the Husimi function to the theoretical model. With 'Scale',true, the quadratures of channel 1 and 2 are scaled to account for a difference in their photon numbers. With 'MonteCarloError',true, an error is computed for all quantities. Set it to false to save time. With 'Parameter', set which parameter was varied during the series and is indicated in the filenames so it can be read out by Matlab ('no', if no parameter was varied). E.g. for a power series, filenames have the structure "02-xxmW-yymW-LOwithDL.raw", where xx is the excitation power and yy the LO power.

- Within this function, **plotHusimiAndCut** is used to plot and fit the Husimi function.

A.5 Evaluation of 3 Channel Measurements of regularized P functions

Let us assume that channel 3 is the target channel, channel 1 is the postselection channel with piezo modulation, and channel 2 is the remnant postselection channel. A series with different time delays of channel 3 was measured.

- Again, we start by computing the quadratures with **seriesQuadratures('Channels',1:3,'Offset',["local" "local" "local"], 'Piezo','yes','CorrRemove',[true,true,true]);**

- Then, the series can be processed for different postselection parameters; i.e. we select different phase-space regions from the Husimi function in the two postselection channels and for each selection, we create a regularized P function from the target data, for each of the time delays.

In the first run, we use only one postselection region. In this run, the computed phases and orthogonal quadratures are stored in the quadrature datasets so they can be used in the next runs to save time. We start e.g. with (numbers are examples from a real measurement)
zeroDelay = 108.96; This is the delay line position that corresponds to zero time difference between the target channel and the other channels.
listOfParams = struct('Type',{'fullcircle'},'Position',{[7 0.4]});
This selects a ring in the Husimi function with a radius of 7 and a thickness of 0.4. Attention: When using the normalization for quadratures $\Delta X_{vacuum} = 1$, i.e. $A = 1$, these are later multiplied with $\sqrt{2}$.
makeSelectionPlots('table','ListOfParams',listOfParams,'Period',4, 'RecomputeTheta',true,'SaveTheta',true,'RecomputeOrth',true, 'saveOrth',true,'SavePostselection',true, 'ChannelAssignment',[3,1,2], 'ZeroDelay',zeroDelay,'Parameter','delay','RemoveModulation',true, 'Range',[0 20],'XUnit','ps','VaryAPS',false,'CorrRemove','yes', 'ZeroDelay',zeroDelay,'MeanNs',[13.8739,14.8419,9.3581]);

- In the next runs, the postselection is done for many more radii, whereby the phase and orthogonal quadratures are used that were computed and saved in the previous step. Therefore, we set some arguments as false, e.g.
  t = 0.4;
  listOfParams = struct('Type',{'fullcircle'},'Position',{[2 t],[3,t],[4,t],[5 t],[6 t],[7 t],[8 t]});
  makeSelectionPlots('table','ListOfParams',listOfParams,'Period', 4,'RecomputeTheta',false,'SaveTheta',false,'RecomputeOrth',false, 'saveOrth',false,'SavePostselection',true,'ChannelAssignment',[3,1,2], 'ZeroDelay',zeroDelay,'Parameter','delay','RemoveModulation',true, 'Range',[0 20],'XUnit','ps','VaryAPS',false,'CorrRemove','yes', 'ZeroDelay',zeroDelay,'MeanNs',[13.8739,14.8419,9.3581]);
  This function creates a table with postselected values, as well as storing the postselected data in the folder "post-data".
  'ChannelAssignment': This sets which channel is the target, which is the postselection channel where the piezo is modulated for the phase computation and which is the postselection channel without piezo modulation, according to [target,ps-piezo,ps-no-piezo].
  The 'removeModulation' option removes longterm drifts of the signal by scaling it to the mean photon number over all time delays set by 'MeanNs'. (The values have to be determined from the data). Also, random jumps of the signal outside a certain range of photon numbers set with 'Range' are removed.

- **makeSelectionPlots** uses **makeDelayPlots**, which in turn runs **series3Ch** for each set of postselection parameters. Also, **makeSelectionPlots** uses **plotSeriesPostselections**, which makes different types of plots if you set e.g. 'radiusPlots' instead of 'table' when running **makeSelectionPlots**.

A.5.1 Computation of pattern functions for the regularized P function

Before the regularized P function can be reconstructed from the data, the pattern functions for the P function have to be computed once. In our case, this is done for a normalization of quadratures such that the fluctuations of a vacuum field $\Delta X_{vacuum} = 1$, i.e. $A = 1$. The Matlab function **mainCalcGridsAndPatterns(varargin)** creates all necessary coordinate grids and pattern functions and saves them for given parameters in a given directory. Here we used the following parameters, whereby 'R' is the filter parameter for the regularized P function:
mainCalcGridsAndPatterns('MaxQuad',20,'MaxX',20,'PhiStep',0.1,'R',0.7, 'XStep',1,'Resolution',0.25);
This function executes the following procedure:

- **[xGrid,phiGrid] = makeGridxAndPhi(maxX,xStep,phiStep);**
  This creates a grid of position intervals and phase intervals (x, phi), which are defined by the parameters 'PhiStep', 'MaxX' and 'XStep'. This is the coordinate grid to which the measured data is compared, being called old grid.

- **makeXGridAndPattern(xGrid,phiGrid,R,maxQuad,Resolution, directory);**
  For each position in the old grid, so-called X parameters (XGrid) (cf. Eq. (C.14)) and the corresponding pattern function (Eq. (C.14) and Eq. (C.15)) are computed and stored. Both are saved in a file called e.g. 'x-0.5-phi-0.1.mat', as for each position (x, phi) in the old grid, one file is created. For computing the X parameters, we define a new grid of quadratures, specified by 'maxQuad' and 'Resolution'. These new quadratures provide the phase-space coordinates on which the regularized P function is displayed.

A.5.2 Computing the P functions and plotting the results

Then, the regularized P functions are calculated from the postselected data, e.g. with these parameters:

- **zeroDelay=108.96; t = 0.4;**
  listOfParams = struct('Type',{'fullcircle'},'Position',{[2 t],[3,t],[4,t],[5 t],[6 t],[7 t],[8 t]});
  for iParams = 1:length(listOfParams)
  PFunctionDelaySeries('LoadExistent',true,'Plot',false,'ZeroDelay',

zeroDelay,'SelectionParameters',listOfParams(iParams),
'RemoveModulation',true,'Range',[0 20],'MaxQuad',20,'MaxX',20,
'PhiStep',0.1,'Rvalue',0.7,'XStep',1,'Resolution',0.25);
end
Set 'Plot',true, for plotting each P function. Also it is necessary to set the path where the pattern functions have been stored; see inside the Matlab script.

- Then, the expectation values from the P functions can be plotted versus delay via
plotPFunctionResults(listOfParams,'Quantity',{'R'},'fitType','exp2sat1',
'RemoveModulation', true,'Range',[0 20],'MaxQuad',20,'MaxX',20,
'PhiStep',0.1,'Rvalue',0.7,'XStep',1,'Resolution',0.25,'Norm',1);
With 'Quantity', set for which quantity the expectation value is plotted, e.g. {'R'} for the amplitude and {'circVa1'} for the circular variance. 'FitType' can be set to various fit functions. Set it to 'exp2' when plotting the mean amplitude, so the offset can be fitted, or to 'envelopeExp2' in order to fit the envelope of an oscillating curve. The results from the fits are stored into new files.

A.6 Evaluation of Dispersions

For the evaluation of spectroscopic dispersions, a few Matlab functions can be used.

- For a series of different positions on the sample e.g.:
plotDispersionsPositionSeries('ZeroPosition',3.67,'ZoomE',[1.59 1.64]);
'ZeroPosition' gives the position of the sample edge. 'ZoomE' gives the plotted energy range in eV.

- For a series of polarizations, polar plots are created via e.g.:
plotDispersionsPolarisationSeries('minY',213,'xAperture',142,
'GetTime','no','Fit','useOld','E0Old',E0,'aOld',a,'y0',y0,'ModeK', [-0.5
0.5],'ModeE',[1.6103 1.6109],'AdjustEnergy',true);
Here, 'minY', and 'xAperture' give the calibration of the k space. 'GetTime' toggles whether the intensity is divided by the acquisition time. 'Fit', 'useOld', 'E0Old', E0, 'aOld', a, 'y0', y0 draws a parabola into the dispersion for which the parameters have to be determined from a dispersion below threshold. 'ModeK' and 'ModeE' define the rectangle in which the intensity is integrated. 'AdjustEnergy' sets whether the energy of the rectangle is adapted to account for a red- or blue shift during the series.

- For a power series, an I-O curve is created via e.g.:
plotDispersionsPowerSeries('minY',214,'xAperture',142,'GetTime',
true,'Fit','useOld','E0Old',E0,'aOld',a,'y0',y0,'ModeK',
[-0.5 0.5],'ModeE',[1.6101 1.6111],'adjustEnergy',true);

Appendix B

Details on error estimation from Husimi functions

As described in Chapter 7, the measured quadrature values of two homodyne detection channels are binned to obtain a histogram, which (when normalized) corresponds to the Husimi Q function. For any given point in phase space, the mean value $\bar{Q}(q,p)$ is the empirical probability of the corresponding (q,p) bin and the margin of error is given by the standard error, $\sigma(Q) = [\bar{Q}(1-\bar{Q})/\nu]^{1/2}$ for ν data points.

We fit the measured Q function to the model of a displaced thermal state for extracting parameters, such as $\bar{n}$ and $|\alpha_0|^2$, which are then used to compute other properties like e.g. the quantum coherence, here denoted by z. In order to propagate errors to these final properties, we use a Monte Carlo error estimation. For this purpose, we simulate a sufficiently large sample of random Q functions, $\{Q_i\}_i$, according to a Gaussian distribution with a mean $\bar{Q}$ and a standard deviation $\sigma(Q)$ for each point in phase space. For each sample element i, we determine the parameters z_i separately via fitting. Then, the standard deviation of the resulting parameter set $\{z_i\}_i$ yields the uncertainty of z.

Appendix C

Derivation of the pattern function for the regularized P function

This appendix derives how the regularized P function can be expressed with help of a pattern function [LPB$^+$]. For simplicity, first we derive this decomposition for the unfiltered P distribution, then we explain how it is altered by the filter Ω, and finally we show how the measured data is inserted.
We begin with the unfiltered Glauber-Sudarshan distribution, $P(\alpha)$. Its Fourier transform defines the characteristic function

$$\widetilde{P}(\beta) = \int_{\mathbb{C}} d^2\alpha \, P(\alpha) e^{\beta\alpha^* - \beta^*\alpha} = \langle e^{\beta\hat{a}^\dagger} e^{-\beta^*\hat{a}} \rangle, \tag{C.1}$$

where the second relation connects to the normally ordered displacement operator. Applying the Baker-Campbell-Hausdorff formula, we can rewrite the quantum expectation value in terms of quadratures,

$$e^{\beta\hat{a}^\dagger} e^{-\beta^*\hat{a}} = e^{|\beta|^2/2} e^{i|\beta|\hat{q}(\pi/2 - \arg\beta)/A}, \tag{C.2}$$

with $\hat{q}(\varphi) = A(e^{i\varphi}\hat{a} + e^{-i\varphi}\hat{a}^\dagger)$. A is a normalization constant relating to the uncertainty product $\Delta q \Delta p \geq A^2$ cf. Eq. (2.29).

Now, the P distribution is the inverse Fourier transform of the characteristic function:

$$P(\alpha) = \int_{\mathbb{C}} \frac{d^2\beta}{\pi^2} \, e^{\beta^*\alpha - \beta\alpha^*} e^{|\beta|^2/2} \langle e^{i|\beta|\hat{q}(\pi/2 - \arg\beta)/A} \rangle. \tag{C.3}$$

The goal is now to seperate the term in angular brackets $\langle ... \rangle$ from the rest because this term corresponds to the measured data. When transforming $\gamma = i\beta^*$, we get

$$P(\alpha) = \int_{\mathbb{C}} \frac{d^2\gamma}{\pi^2} \, e^{-i(\gamma\alpha + \gamma^*\alpha^*)} e^{|\gamma|^2/2} \langle e^{i|\gamma|\hat{q}(\arg\gamma)/A} \rangle. \tag{C.4}$$

Substituting $\gamma = se^{i\varphi}$ with $s \in \mathbb{R}$ and $0 \leq \varphi < \pi$ allows us to write

$$P(\alpha) = \int_{-\infty}^{\infty} ds \int_0^{\pi} d\varphi \, \frac{|s|}{\pi^2} e^{-2is\mathrm{Re}(e^{i\varphi}\alpha)} e^{s^2/2} \langle e^{is\hat{q}(\varphi)/A} \rangle. \tag{C.5}$$

The quadrature operator can be given in its spectral decomposition, using the eigenvalue equation $\hat{q}(\varphi)|q;\varphi\rangle = q|q;\varphi\rangle$, resulting in

$$P(\alpha) = \int_{-\infty}^{\infty} ds \int_0^{\pi} d\varphi \, \frac{|s|}{\pi^2} e^{-2is\mathrm{Re}(e^{i\varphi}\alpha)} e^{s^2/2} \int_{-\infty}^{\infty} dq \, e^{isq/A} \langle q;\varphi|\hat{\rho}|q;\varphi\rangle \tag{C.6}$$

for a density operator $\hat{\rho}$. This expression can be separated into a measured part,

$$P(\alpha) = \int_{-\infty}^{\infty} dq \int_0^{\pi} d\varphi \, p(q;\varphi) f(\alpha;q;\varphi), \tag{C.7}$$

where $p(q;\varphi) = \langle q;\varphi|\hat{\rho}|q;\varphi\rangle$, and the measurement-independent part

$$f(\alpha;q;\varphi) = \int_{-\infty}^{\infty} ds \frac{|s|}{\pi^2} e^{-2is\mathrm{Re}(e^{i\varphi}\alpha)} e^{s^2/2} e^{isq/A}, \tag{C.8}$$

defining the divergent pattern function (i.e., distribution) for the Glauber-Sudarshan distribution. Note that $p(q;\varphi)$ is the probability density for measuring q for a fixed angle φ, i.e., the conditional probability $p(q;\varphi) = p(q,\varphi)/p(\varphi)$, with the joint and marginal (w.r.t. the angle) densities $p(q,\varphi)$ and $p(\varphi)$.

After decomposing the unregularized Glauber-Sudarshan P distribution, now we replace P by its regularized counterpart, see Eq. (8.1):

$$P_\Omega(\alpha) = \int_{\mathbb{C}} d^2\gamma \, \Omega(\gamma) P(\alpha - \gamma), \tag{C.9}$$

using the regularizing function as in Eq. (8.5)

$$\Omega(\gamma) = \left[\frac{J_1(2R|\gamma|)}{\sqrt{\pi}|\gamma|} \right]^2, \tag{C.10}$$

with J_n denoting the nth Bessel function of the first kind.

Inserting this into the considerations above, this yields the pattern function

$$f_\Omega(\alpha;q;\varphi) = \int_{\mathbb{C}} d^2\gamma \, \Omega(\gamma) \int_{-\infty}^{\infty} ds \, \frac{|s|}{\pi^2} e^{-2is\mathrm{Re}(e^{i\varphi}[\alpha-\gamma])} e^{s^2/2} e^{isq/A}. \tag{C.11}$$

In polar coordinates, $\gamma = re^{i\vartheta}$, this yields

$$\begin{aligned} f_\Omega(\alpha;q;\varphi) &= \int_0^\infty dr \int_0^{2\pi} d\vartheta \int_{\mathbb{R}} ds\, \frac{|s|}{\pi^3 r} J_1(2Rr)^2 e^{2isr\cos(\varphi+\vartheta)} e^{is[q/A-2\mathrm{Re}(e^{i\varphi}\alpha)]} e^{s^2/2} \\ &= \int_0^\infty dr \int_{\mathbb{R}} ds\, \frac{2|s|}{\pi^2 r} J_1(2Rr)^2 J_0(2sr) e^{is[q/A-2\mathrm{Re}(e^{i\varphi}\alpha)]} e^{s^2/2} \\ &= \int_{\mathbb{R}} ds\, \frac{2|s|}{\pi^2} \int_0^\infty dy\, \frac{J_1(y)^2 J_0\left(\frac{|s|}{R}y\right)}{y} e^{is[q/A-2\mathrm{Re}(e^{i\varphi}\alpha)]} e^{s^2/2}, \end{aligned} \tag{C.12}$$

applying a transformation $y = 2Rr$ in the last step.

It is now convenient to evaluate the transformed integral,

$$\begin{aligned} g(t) &= \int_0^\infty dy\, \frac{J_1(y)^2 J_0\left(2ty\right)}{y} \\ &= \frac{1}{\pi} \begin{cases} 0 & \text{for} \quad t > 1, \\ \arccos(t) - t\sqrt{1-t^2} & \text{for} \quad 0 \le t \le 1, \end{cases} \end{aligned} \tag{C.13}$$

where $2t = |s|/R$.

This allows us to express the pattern function via an integral over a finite interval,

$$\begin{aligned} f_\Omega(\alpha;q;\varphi) &= \int_{-2R}^{2R} ds\, \frac{2|s|}{\pi^2} g\left(\frac{|s|}{2R}\right) e^{is[q/A-2\mathrm{Re}(e^{i\varphi}\alpha)]} e^{s^2/2} \\ &= \frac{8R^2}{\pi^3} \int_{-1}^1 du\, |u| \left[\arccos(|u|) - |u|\sqrt{1-u^2}\right] e^{iuX} e^{2R^2u^2} \\ &= \frac{16R^2}{\pi^3} h(X,R), \end{aligned} \tag{C.14}$$

where $u = s/(2R)$, $X = 2R[q/A - 2|\alpha|\cos(\varphi + \arg\alpha)]$ and

$$h(X,R) = \int_0^1 du\, u \left[\arccos(u) - u\sqrt{1-u^2}\right] \cos(uX) e^{2R^2u^2}, \tag{C.15}$$

which can be evaluated numerically for a given R and any X. In particular, a sufficiently dense (typically not equidistant) grid of X parameters for a given R can be stored and used later for any $X' \approx X$. Note that thanks to the regularization, the pattern function is not divergent anymore.

All above considerations enable us to analytically write

$$P_\Omega(\alpha) = \int_{-\infty}^\infty dq \int_0^\pi d\varphi\, p(q;\varphi) f_\Omega(\alpha;q;\varphi) = \int_{-\infty}^\infty dq \int_0^\pi \frac{d\varphi}{\pi} \frac{p(q,\varphi)}{\int_{\mathbb{R}} dq'\, p(q',\varphi)} \pi f_\Omega(\alpha;q;\varphi). \tag{C.16}$$